

June 2021

Metal Oxide Sensor Array Test Bed Prototype for Diagnostic Breath Analysis

Tiffany C. Miller
University of South Florida

Follow this and additional works at: <https://digitalcommons.usf.edu/etd>



Part of the [Electrical and Computer Engineering Commons](#)

Scholar Commons Citation

Miller, Tiffany C., "Metal Oxide Sensor Array Test Bed Prototype for Diagnostic Breath Analysis" (2021).
USF Tampa Graduate Theses and Dissertations.
<https://digitalcommons.usf.edu/etd/9188>

This Dissertation is brought to you for free and open access by the USF Graduate Theses and Dissertations at Digital Commons @ University of South Florida. It has been accepted for inclusion in USF Tampa Graduate Theses and Dissertations by an authorized administrator of Digital Commons @ University of South Florida. For more information, please contact digitalcommons@usf.edu.

Metal Oxide Sensor Array Test Bed Prototype for Diagnostic Breath Analysis

by

Tiffany C. Miller

A dissertation submitted in partial fulfillment
of the requirements for the degree of
Doctor of Philosophy
Department of Electrical Engineering
College of Engineering
University of South Florida

Major Professor: Salvatore D. Morgera, Ph.D.
Stephen E. Sadow, Ph.D.
Ashwin Parthasarathy, Ph.D.
Mile Krajcevski, Ph.D.
Mark Jaroszeski, Ph.D.

Date of Approval:
June 30, 2021

Keywords: Gas Sensor, Volatile Organic Compounds, COVID-19,
SARS-CoV-2, Viral and Bacterial Pathogens

Copyright © 2021, Tiffany C. Miller

Dedication

This Dissertation is dedicated to my those affected by the COVID-19 pandemic and my Grandma, Sally Spangenberg, who recently passed from contracting COVID-19.

Acknowledgments

I thank The University of South Florida COVID-19 Rapid Response Research Grants program and the efforts made by the University of South Florida researchers, canine detection specialists, and breath specialists based in Edinburgh, UK, in Dortmund, Germany, and in Jacksonville, Florida U.S., for their contributions to high impact research and public service during this global pandemic. I am grateful for the guidance set forth by my Major Professor and Committee Members to help me navigate through the Dissertation process to completion. In particular, I would like to thank Dr. Salvatore Morgera for Founding and Leading the Bull Nose Research Group in which a weekly meeting always addressed this important research. I also would also like to thank Dr. Stephen E. Sadow for teaching me basic electrical engineering concepts with hours of discussion and Dr. Arash Takshi for the laboratory support in which he taught me the necessary gas sensor circuitry setups and calibration techniques for this important research. I thank Dr. Ashwin Parthasarathy, Dr. Mile Krajcevski, Dr. Mark Jaroszeski, and Dr. Matthew Mullarkey for their valuable contributions and time serving on my Dissertation committee.

Table of Contents

List of Tables	iii
List of Figures	iv
Abstract	vi
Chapter 1: Introduction	1
Chapter 2: A Review of VOC's and the Means for Their Detection.....	7
2.1 COVID-19 and Diagnostic Testing	8
2.1.1 Observed Symptoms of COVID-19	8
2.1.2 Ferritin Levels and COVID-19	10
2.1.3 Diagnostic Testing of COVID-19	11
2.1.4 Endogenous Compounds of Disease.....	13
2.2 Brain Breath Biochemistry in Neurological Complications of COVID-19.....	15
2.2.1 Infection Mechanism of SARS-CoV-2.....	15
2.2.2 Olfactory Nerve	17
2.2.3 Olfactory Bulb Signal Recording.....	20
2.2.4 Volatile Organic Compound Profiles of Lung Disease	21
2.2.5 Neurological Manifestations of Inflammation.....	22
2.2.5.1 Nitric Oxide Expression.....	23
2.2.5.2 Carbon Monoxide Expression.....	25
2.3 Electronic Nose Technology.....	26
2.3.1 Space Shuttle Air Quality Monitoring	27
2.3.2 Detectable Breath Ammonia and Liver Health.....	29
2.3.3 Air Collection Devices for Breath Emissions in Bats.....	29
2.3.4 Metal Oxide Semiconductor Gas Sensors in Fruit Industry	30
2.3.5 Electronic Nose Detection of Chronic Rhinosinusitis	31
2.3.6 Field-Effect Transistor Biosensor Detection of SARS-Cov-2.....	33
2.3.7 Nanocrystalline Metal Oxide Film Sensor for Influenza Detection	33
2.3.8 Gas Chromatography for Inflammatory Lung Disease Detection	34
Chapter 3: Materials and Methods	37
3.1 Electronic Nose Gas Detection Experiments	38
3.1.1 COVID-19 Breath Simulation Mixture	41
3.1.2 Design and Assembly of the Gas Sensor Array Test Bed Prototype.....	44
3.1.2.1 System Architecture.....	47

3.1.2.2 Gas Sensor Signal Conditioning and Interfacing	48
3.2 Gas Measurement Protocol and Results for Preliminary Gas Data Acquisition	55
3.2.1 Flow Rate Impact	58
3.2.2 Gas Concentration Gradient.....	64
3.3 Gas Measurement Protocol and Results for OSC in a Stability Regression Model.....	67
3.3.1 Measurement Instability.....	70
3.4 Reporting Diagnostic Accuracy	73
Chapter 4: Drift Correction and Calibration	74
4.1 Drift Correction.....	74
4.1.1 Baseline Manipulation	75
4.1.2 Orthogonal Signal Correction (OSC).....	76
4.1.3 Calibration.....	81
4.1.4 Selected Characteristic Features	83
4.1.5 Stability Test	83
Chapter 5: Conclusions	85
Chapter 6: Recommended Applications	89
References	93
Appendix A: Copyright Permissions	107
Appendix B: MQ and LED Arduino Uno Source Code	112
Appendix C: BMW280 Arduino Uno Source Code	118
Appendix D: HRP-310 – Worksheet for Human Subjects Research Determination.....	121
Appendix E: Glossary of Terms	124
Appendix F: Publications.....	128
About the Author	End Page

List of Tables

Table 2.1 COVID-19 symptoms and associated biomechanisms	9
Table 2.2 Electronic nose devices with target gas discrimination and gas sensor type.....	14
Table 2.3 Odor analysis of endogenous compounds of disease compared to healthy controls.....	28
Table 3.1 VOC concentration trends in exhaled breath of healthy samples compared to viral infiltrated samples.....	43
Table 6.1 Volatile organic compounds (VOCs) of indoor pathogens including, bacteria, viruses, and different genera of molds capable of impacting a healthy indoor space.....	90

List of Figures

Figure 3.1	Electronic nose comprising a breath collection vessel, a mask, and a computer	38
Figure 3.2	Electronic nose having gas sensing components retained within an internal bladder being in communication with a sample vessel, compressed oxygen carrier gas, and a flowmeter.....	40
Figure 3.3	Schematic diagram of the experiment comprising a testbed prototype.....	41
Figure 3.4	The electronic nose testbed prototype housing has LEDs illuminating in response to predetermined threshold levels of target gas concentration in ppm.	46
Figure 3.5	The MQ sensor side comprising 6 legs, wherein, two of the legs are labeled H and are configured to heat the sensing element connected by a nickel-chromium coil and platinum wires of the 4 remaining legs, labeled A and B, are connected to the sensing element and are configured to convey output responses of current changes occurring through the sensing element	48
Figure 3.6	The MQ module component side has four pins being Common Collector Voltage (VCC), Ground (GND), Digital (D0), and Analog (A0).....	49
Figure 3.7	A systematic design of the sensor unit having a breadboard in electrical communication with a first and a second Arduino Uno microcontroller, a MQ-2 gas sensor, a MQ-135 gas sensor, a BME280, and 5 LEDs	50
Figure 3.8	Each LED is individually electrically connected to a 220-ohm resistor on a breadboard.....	51
Figure 3.9	A schematic wiring diagram of the sensor unit having a first and a second Arduino Uno microcontroller in electrical communication with a MQ-2 gas sensor, a MQ-135 gas sensor, a BME280, and 5 LEDs.....	52
Figure 3.10	Signal condition circuit of the MQ gas sensor having resistor (RL), 5V supply voltage (VC), and the measured analog/digital value being the output voltage(Vout)	54

Figure 3.11 (a) Temperature and flow control of baseline drift over the MQ-2 and MQ-135 MOS based sensors, (b) Output responses of the MQ-2 sensor at different flow rates of 300 ppm sample solution, (c) Output responses of the MQ-135 sensor at different flow rates of 300 ppm sample solution	59
Figure 3.12 Gas concentration gradient of simulated breath sample having a flow rate of 25.00 mL/min (a) for the MQ-2 sensor, (b) for the MQ-135 sensor	61
Figure 3.13 Output response voltages from of the MQ-2 sensor and the MQ-135 sensor with associated individual gas concentrations in ppm of acetone, alcohol, and CO from the 300 ppm sample solution at a flow rate of 25.00 mL/min for 30 s	62
Figure 3.14 Correlation analysis of the concentration gradient between output response (V) versus the concentration (ppm) of COVID-19 simulation solution, (a) for the MQ-2 sensor, (b) for the MQ-135 sensor.....	65
Figure 3.15 (a) Output responses of the MQ-2 sensor at different flow rates of 300 ppm sample solution, (b) Output responses of the MQ-135 sensor at different flow rates of 300 ppm sample solution.....	68
Figure 3.16 Temporal responses at 10 ppm, 50 ppm, 100 ppm, 200 ppm, and 300 ppm of COVID-19 breath simulation solution concentration at 25.00 mL/min (a) for the MQ-135 sensor, (b) for the MQ-2 sensor	71
Figure 3.17 Instability of the MQ-2 gas sensor depicted as output responses of initial resistance were collected during a plurality of consecutive measurements of the 5 concentrations of 10 ppm, 50 ppm, 100 ppm, 200 ppm, and 300 ppm of COVID-19 breath simulation solution	72
Figure 4.1 Temporal responses of concentrations of 10 ppm, 50 ppm, 100 ppm, 200 ppm, and 300 ppm of COVID-19 breath simulation solution concentration at 25.00 mL/min following OSC for (a) for the MQ-135 sensor, (b) for the MQ-2 sensor.....	79
Figure 4.2 PCA plot after OSC correction for concentrations of 10 ppm, 50 ppm, 100 ppm, 200 ppm, and 300 ppm of COVID-19 breath simulation.....	80
Figure 4.3 Plot illustrating RMSE values on the y-axis and number of PLS and PLS with OSC components on the x-axis	82

Abstract

Detection of specific target biomarkers is a critical step for electronic nose technologies in breath analysis. Electronic nose technologies have been successfully demonstrated in the air quality, meat processing, and the citrus industries, as well as cancer clinical trials. The novel design, assembly, and implementation of a test bed prototype of an electronic nose system is introduced in this Dissertation. To verify the feasibility of a test bed prototype design, a Corona Virus Disease 2019 (COVID-19) breath simulation mixture of alcohol, acetone, and carbon monoxide was presented to the test bed prototype in the laboratory. The COVID-19 breath simulation mixture was developed from a literature review and from preliminary gas chromatography ion mobility spectrometry data obtained from parallel COVID-19 breath studies based in Edinburgh and Dortmund. As a result, the test bed prototype was fit with metal oxide semiconductor (MOS) MQ-2 and MQ-135 gas sensors due to their availability, affordability, high sensitivity, high selectivity, and low recovery time properties related to their respective target gasses. The sensors were configured to show a detection range for alcohol, acetone, and carbon monoxide in part per million (ppm) level.

The problem with the use of MOS based sensors in electronic nose technologies is system instability, due to a result of gradual drifts in the output responses of the MQ-2 and MQ-135 sensors. This instability directly pertains to the baseline output response of the MQ-2 and MQ-135 sensors not being accurately obtained. A main focus of this Dissertation analyzes a signal processing approach involving the manipulation of the gas sensor output response baseline using

Orthogonal Signal Correction (OSC) in an attempt to decrease the negative influence of gradual drifts associated with the output response of the MQ-2 and MQ-135 sensors. The proposed signal processing approach of applying baseline manipulation with OSC was performed to eliminate and/or minimize the drift effects of the MQ-2 and MQ-135 gas sensors responding to varying concentrations of the COVID-19 breath simulated mixture of methyl alcohol, acetone, and carbon monoxide (CO). A Partial Least Squares (PLS) regression model is then employed to determine the approximate concentration of gas detected in ppm after the corrected datasheet undergoes baseline manipulation. This Dissertation will detail how the proposed signal processing approaches increase the reproducibility of the sensor output responses by enhancing the regression model stability while maintaining an accuracy suitable for breath analysis applications.

Chapter 1: Introduction

A portion of this chapter was accepted for publication in [154]. Permission to reproduce the works in this Dissertation is included in Appendix A.

The Corona Virus Disease 2019 (COVID-19) pandemic, caused by severe acute respiratory syndrome coronavirus 2 (SARS-CoV-2), was identified in December 2019 and has since spread rapidly across the globe, resulting in at least 26 million cases and approximately 440,000 deaths by January 2021 [102]. The transmission of SARS-CoV-2 includes viral shedding through the potential fecal-oral route as well as bioaerosols emitted orally and nasally [105]. For example, respiratory droplets retaining SARS-CoV-2, have an approximate size between 65 nm-125 nm, which are emitted by the force of a breath, a cough, or a sneeze of an infected individual [103], [104]. These infectious airborne particles then contaminate surfaces of the surrounding environment, such as a tabletop, doors, or even the mouth, nose and eyes of other individuals.

Many countries have been implementing reverse transcription-polymerase chain reaction (PCR) COVID-19 testing of its population to reduce the spread of COVID-19. Studies have revealed that lockdowns and mobility reductions decreased the transmission rate of COVID-19 in Europe and North America [106]. However, manufacturers of the current PCR COVID-19 diagnostic test kits struggle to keep up with demand and experience testing kit shortages and long processing times [107]. As a result, test results may be delayed which then delays the intervention of quarantining the potentially infected individual who may be transmitting viral particles within the wait period for their test results, which is typically 3 or more days. Thus, there is a need for a

rapid COVID-19 screening test that can provide results in real-time so that a confirmed COVID-19 infected individual can be alerted of their infection status within seconds of taking the test. A confirmed COVID-19 positive individual would be immediately advised by a healthcare professional, at point of care, to quarantine and isolate to slow the spread of infection, so that businesses and schools can continue providing services in a COVID-19 free environment.

This Dissertation details research conducted from April 2020 to May, 2021 which culminated in a response to the University of South Florida (USF, Tampa, FL) COVID-19 Rapid Response Research Task Force, led by Dr. Salvatore D. Morgera. The Task Force challenged researchers to develop novel approaches to address the respiratory illness pandemic in the form of COVID-19, to help prevent the spread of the virus by rapid diagnostic detection. The work presented here represents the design, assembly, and implementation of a test bed prototype configured for detecting volatile organic compounds (VOCs) associated with inflammatory biomarkers of viral infection and COVID-19 from exhaled breath samples of infected individuals. The test bed prototype consists of a gas collection system having an array of metal oxide semiconductor (MOS) MQ-2 and MQ-135 gas sensors in communication with a microcontroller and an electronic device such as a computer, a tablet, or a smart phone.

As a result of MOS based gas sensor commercial availability, low cost, and sensor properties, including a high sensitivity to target gases and a short recovery time, the MQ-2 and MQ-135 gas sensors are commonly used gas sensor components for electronic nose technologies for biomedical applications; however, their suitability has yet been determined for use in electronic nose systems directed at real-time monitoring for breath analysis applications [109], [110]. The problem with the use of MOS-based sensors in electronic nose technology is system instability due to the output response of the sensor not being under stable control because of gradual drifts in

the output response of the MQ-2 and MQ-135 sensors. This results in an inability to successfully reproduce output responses using these sensors. It would be more desirable to have a gas sensor having an increased reproducibility of more controlled output responses so that acquired gas sensor data obtained from a laboratory setting may be more efficiently applied toward breath analysis applications [114]. This baseline instability directly pertains to the baseline output response of the MQ-2 and MQ-135 sensors not being accurately obtained due to factors such as drifts, environmental influences, and sampling means [108]. In particular, as it relates to drifts, as a slight variation is observed in MOS-based gas sensor output responses of electronic nose devices having the sensors exposed to an unchanged target gas sample with an unchanged concentration value having the surrounding environment at an ambient status.

Drift in a sensor is a natural phenomenon in which a low frequency change occurs. Drift changes occurring between sample intervals has been investigated to be attributed to many factors including, the degradation of the heating element comprising a nickel-chromium coil surrounded by a layer of aluminum oxide-based ceramic of the sensor over time or damage to the sensing element, comprising a layer of tin dioxide overlaying the heating element, from chemicals that can compromise the integrity of the sensor components [111], [112]. Further, unstable drift changes of MOS-based gas sensors may result from changes in the environment of the sample chamber such as, temperature, humidity, flow rate of the sample, and concentration of target gas [113]. Drift variation is magnified in breath analysis applications when the sensors of an electronic nose device are exposed to a diversity of target gasses within an exhaled breath sample, at varying concentrations, and a changing flow rate corresponding to the inconsistent force of the exhaled breath emitted from an individual's lungs. [154]

In addition, undesirable drift variation exists in MOS-based gas sensors due in part to the sampling mechanism in which the heated tin dioxide layer of the gas sensor is configured for oxygen adsorption on its surface. This oxygen adsorption decreases the flow of electric current flowing through the coil of the MOS gas sensor until the surface density of adsorbed oxygen lowers during sensor exposure with a target gas. As a result of target gas exposure to a MOS gas sensor, a resistance change having a value measured using a voltage divider network occurs and is associated with the detection of a specific gas. Thus, in the presence of reducing gases, more electrons can flow across the coil. The sampling mechanism comprising the electron flow across a coil of a MOS gas sensors requires lengthy cycling time when a saturated sensor refreshes back to baseline drift. This response and recovery time may hinder the accuracy of results and not be suitable for breath analysis applications unless corrected using signal processing [108]. Although an efficient cleaning process is a solution to minimizing drifts after each gas exposure phase, the cleaning process requires a length of time that is not suitable for an electronic nose in clinical applications for breath analysis. This Dissertation will present a signal processing method to minimize the effects of drift on MOS-based gas sensor output responses so that the sensor response drifts are reduced, thus providing quicker and continuous measurements. As a result, fast measurements as well as maintaining the accuracy of the results are expected from applying the signal processing cleaning step [128]. [154]

Current signal correction methods such as univariate and multivariate are configured for increasing the quality of the sensor output response. Univariate methods are capable of applying the correction to one variable, such as the gas sensor during baseline manipulation [115]. This alteration is commonly referred to as a transformation and is configured for the correction, such as differential, relative, or fractional, of the sensor's signal baseline. Some studies have indicated the

use of baseline manipulation as a means for preliminary processing of the output response of the gas sensor [116]. Other studies have utilized various filtering techniques such as Moving Median Filter (MMF), Fourier Bandpass Filter (FBF), and Discrete Wavelet Transform (DWT) to eliminate adverse drift effects from acquired gas data [117], [118]. [154]

Studies have indicated a correlation between output responses of gas sensors and drift effects that have influenced the direction of electronic nose technologies towards utilizing multivariate signal correction methods to apply the correction to many variables, such as a plurality of gas sensors, resulting in an increased amount of data being detected for modeling of nonlinear drift effects [119]. Self-Organizing Maps (SOMs) are a type of adaptive neural network that have been incorporated within the signal processing of some electronic nose sensors [143]. Although the use of this adaptive neural network can accomplish accurate results for the application of gas analysis, the quantification of acquired gas sensor output responses have been identified as a major limitation [120], [123]. Taking the literature review into consideration, it can be discerned that drift is associated with the output response of a gas sensor even during exposure to a target gas having consistent variables such as, temperature, humidity, and time. It would be more desirable to minimize the variance of drift. In another example of multivariate linear correction being applied in other studies, the use of Partial Least Square (PLS) and Principal Component Analysis (PCA) have contributed to the decrease in variance of the gas sensor drift as it flows in a single pathway [113], [121], [122]. Further, some studies have investigated and favored the use of orthogonal signal correction (OSC) algorithms to eliminate the variance that is absent any correlation to the variable for approximate calculation [122], [124], [125]. In a particular study, OSC was used for the correction of near-infrared spectra (NIR) and many publications described machine learning

algorithms to improve the processing of the OSC method to eliminate the variance not correlated to the estimated variable [127], [128]. [154]

The goal of this Dissertation was to determine candidate VOC biomarkers associated with the body's inflammatory response to SARS-CoV-2 and then design, assemble, and implement a test bed prototype capable of detecting these specific VOCs with MQ-2 and a MQ-135 gas sensors. After careful review of the literature and consultation with breath experts involved with breath analysis for COVID-19, the candidate VOC biomarkers included in the COVID-19 breath simulated mixture were alcohol, acetone, and carbon monoxide (CO) for detection analysis with the test bed prototype to acquire preliminary gas sensor output response data. The first step of the proposed signal processing approach includes applying baseline manipulation with OSC to eliminate and/or minimize the drift effects of the MQ-2 and MQ-135 gas sensors responding to varying concentrations of the COVID-19 breath simulated mixture.

Next, a regression model to determine the approximate concentration of gas detected in ppm is realized after the corrected datasheet undergoes Partial Least Square (PLS) regression. As the MQ-2 and MQ-135 gas sensors are exposed to differing concentrations of the COVID-19 breath simulation mixture, PLS regression will be applied to model the output responses of the MQ-2 and MQ-135 sensors. This Dissertation will describe the proposed signal processing correction approach for quantification of COVID-19 breath simulation mixture using a portion of PLS steps in the modeling process for increasing the reproducibility of the sensor output responses by enhancing the regression model stability while maintaining an accuracy suitable for breath analysis applications. It is envisioned that this drift compensation method presented in this Dissertation will enhance electronic nose design capabilities for a wide variety of applications. [154]

Chapter 2: A Review of VOC's and the Means for Their Detection

A portion of this chapter was published in [125] and accepted for publication in [154] . Permission to reproduce the works in this Dissertation is included in Appendix A.

Considering this review and in response to the COVID-19 pandemic, breath specialists based in Edinburgh, UK, in Dortmund, Germany, and in Jacksonville, Florida U.S., have initiated clinical trials of electronic nose technologies directed to VOCs of COVID-19 in exhaled breath. Further, a weekly virtual multidisciplinary meeting was established at the University of South Florida in April 2020 in collaboration with canine detection specialists to discuss and begin understanding neurological manifestations of COVID-19 disease and potential diagnostic breath sensor devices to address a long felt, yet unfulfilled need to standardize electronic nose (eNose) methodologies into a reproducible method for detection of low noise data signature profiles of disease [36]. This section will review several electronic nose devices including their structural components, materials, and their breath sample collection procedures.

This section describes symptoms and standard diagnostic testing methods of COVID-19. Endogenous compounds of disease and the clinical detection of chronic rhinosinusitis (CRS), COVID-19, Influenza Flu Virus, and inflammatory lung disease such as Respiratory Tract Infection (RTI) in a patient's breath by various eNose devices will be discussed. Brain breath biochemistry in neurological complications of COVID-19 will be detailed including the infection mechanism of SARS-CoV-2 with a specific focus on its angiotensin-converting enzyme 2 (ACE2) interaction, viral infection routes from the olfactory epithelium at the nasal cavity to the central

nervous system (CNS), and VOCs in lung disease will be described. Neurological manifestations of COVID-19 will be described including, Guillain-Barre Syndrome (GBS), acute demyelinating encephalomyelitis (ADEM), and Induced Multisystem Inflammatory Syndrome. Electronic nose devices will be reviewed including, the Jet Propulsion Laboratory (JPL) eNose configured for air quality monitoring, the Wize Sniffer configured to determine liver health from breath samples, an air collection device for breath VOCs and body odor emissions in a variety of species of bats, and an eNose sensor configured for monitoring fruit growth and maturation.

2.1 COVID-19 and Diagnostic Testing

Electronic nose technology incorporated with breath analysis protocols have been observed as a successful approach to noninvasive diagnosis demonstrated in clinical trials for breast cancer, colorectal cancer, lung cancer, liver disease, infectious disease such as tuberculosis, and diabetes [101]. Further, electronic nose technologies are currently used in monitoring air quality, spoiled meats, and ripened fruit; however, its impact on emerging pandemics, such as the respiratory illness pandemic in the form of COVID-19, is still under investigation. A significant problem with electronic nose technology is accurate detection of a target gas within a diverse environment of gasses, such as in a breath sample. The use of MOS based gas sensors within an electronic nose system has a great potential as a means of rapid detection of a target gas without having to modify the target gas sample. [154]

2.1.1 Observed Symptoms of COVID-19

On March 11, 2020 SARS-CoV-2 has caused a respiratory illness pandemic in the form of COVID-19 [154]. As illustrated in Table 2.1, a plurality of key symptoms associated with COVID-19 infections include, but are not limited to: fever and dry cough which accompany approximately

Table 2.1 COVID-19 symptoms and associated biomechanisms.

COVID-19 Symptom	Biomechanism	Reference
Fever	Upper Respiratory/ Inflammatory Immune Response	[28], [31]
Dry Cough	Upper Respiratory/ Inflammatory Immune Response	[28]
Hypoxia	Metabolic/ Upper Respiratory/ Inflammatory/ Immune Response	[28]
Headache	Upper Respiratory/ Inflammatory Immune Response	[29]
Nasal Congestion	Mucus Obstruction/Upper Respiratory/ Inflammatory Immune Response	[29]
Sore throat	Upper Respiratory/ Inflammatory Immune Response	[29]
Increased Ferritin levels	Inflammatory/ Immune Response	[31], [91], [92]
Nausea	Gastrointestinal	[29], [30]
Vomiting	Gastrointestinal	[30]
Diarrhea	Gastrointestinal	[30]
Dyspnea	Respiratory	[29], [31]
Fatigue	Musculoskeletal	[29]
Myalgia	Musculoskeletal	[29]
Arthralgia	Musculoskeletal	[29]
Anosmia	Olfactory/Neurodegenerative diseases, mucus obstruction	[32], [33]
Ageusia	Olfactory	[32], [33]

80% of COVID-19 infections [28], [69]. Further, headache, nasal congestion, sore throat, nausea, labored breath or dyspnea, and musculoskeletal symptoms are responses to inflammation while immune response symptoms include fatigue, myalgia or muscle pain, and arthralgia or joint pain [29], [89]. Recently observed symptoms of COVID-19 include anosmia and ageusia. Anosmia is a neurological impairment of olfactory functioning in that the olfactory system is not able to accurately detect and/or correctly identify odors and is characterized by a loss of smell. Ageusia is characterized by a loss of taste [32], [33]. [154]

2.1.2 Ferritin Levels and COVID-19

Clinical laboratory results involving COVID-19 patients have indicated a substantial increase in ferritin levels compared to healthy individuals and diabetics possibly due to the inflammatory response corresponding to disease severity [31]. For example, healthy individuals and diabetics have a combined reference ferritin level range between approximately 30 ng/ml and 400 ng/ml [31]. Studies have evaluated ferritin levels in exhaled breath condensate of lung cancer patients and have identified non-small cell lung cancer (NSCLC) patients having ferritin levels above 60 ng/ml and have identified chronic obstructive pulmonary disease (COPD) patients having ferritin levels ranging between 35 ng/ml and 40 ng/ml [94]. Laboratory findings of mild COVID-19 patients showed a substantially high ferritin blood level of approximately $888.2 \text{ ng/ml} \pm 2181.7 \text{ ng/ml}$ and severe COVID-19 patients having a substantially increased ferritin blood level of approximately $1869.1 \text{ ng/ml} \pm 2229.4 \text{ ng/ml}$ [91]. A study showed that ferritin concentrations were measured noninvasively in exhaled breath condensate (EBD) with an EBC collection device [93], [94], [95].

2.1.3 Diagnostic Testing of COVID-19

Due to the highly contagious and life-threatening characteristics of COVID-19, the Emergency Use Authorization (EUA) authority has allowed the use of real-time reverse transcription polymerase chain reaction (rRT-PCR) testing to detect RNA from SARS-CoV-2 in nasal, nasopharyngeal, and oropharyngeal swabs from patients exhibiting symptoms of the virus [154]. This rRT-PCR method requires target-specific fluorescent labeled oligonucleotide probes which create a signal when they are bound to the amplified RNA [24]. This lengthy procedure requires many steps during preparation of the sample including, but not limited to, collecting samples from nasal swabs, providing quinidine isothiocyanate to disrupt the SARS-CoV-2 virions, providing a magnetic nanoparticle to capture the nucleic acids, washing the sample to remove inhibitors and unbound sample components, providing a nucleic acid detection kit for separating the nucleic acids from the magnetic nanoparticle with a buffer solution, and amplifying the nucleic acids in a deep well plate. An Internal Control Reagent (ICR) is then introduced to the wells and the specimen is plated, amplified, and detected on a reaction plate [24]. This diagnostic process requires many materials associated with an increase in cost and is subject to human error along the process which may adversely affect the accuracy of the testing result. Further, between April-June 2020, there have been shortages of genetic extraction kits, swabs, reagents, masks, and gowns which have halted COVID-19 testing. It would be more desirable to have a method of COVID-19 testing that eliminates the need for excessive equipment, supplies, and multiple steps.

Although rRT-PCR is the current standard and diagnostic testing method due to its high sensitivity having an approximate range between 66-83% for detecting the RNA of SARS-CoV-2, studies indicate false-negative (FN) results from respiratory samples for SARS-CoV-2 and show FN rates (FNRs) having a range between 1% to 30%. The FN's may be due to, for example, swab

contamination from poor sample collection, low viral load, different rates of viral shedding over time in the disease process, and decreased analytic sensitivity [144], [145]. Studies have suggested repeating the rRT-PCR test if a chest computerized tomography (CT) scan suggests COVID-19 specific features despite an initial false-negative test result. Unfortunately, rRT-PCR testing materials not be available during a pandemic scenario when testing supplies and lab technician resources are in short supply and in high demand. [145]. Thus, the substantially increased range of FNRs with rRT-PCR test results serves as a motivation for a diagnostic electronic nose breath analysis testing method. In particular, depending on the type of electronic chemical gas sensors used and the amount of these sensors that comprise a rapid electronic nose device, the high selectivity of these sensors to the breath pattern signature of coronavirus disease would greatly reduce the number of false positives and false negatives associated with existing rRT-PCR diagnostic testing methods.

Since there have been shortages of testing materials such as swabs and associated reagents to perform rRT-PCR, some non-electronic nose investigations have sought out COVID-19 patient breath samples for processing and COVID-19 VOC signature detection with a gas chromatograph ion mobility spectrometer (GC-IMS) device. Evidence suggests a signature of inflammatory and oxidative stress metabolites detected from COVID-19 positive patients using Gas Chromatography (GC) and Ion Mobility Spectrometry (IMS) include, acetone, alcohol, butanone, methanol, isoprene, heptanal, propanol, propanal and octanal [98]. Other studies have indicated VOC concentrations of approximately 10 to 250 parts-per-billion (ppb) of methylpent-2-enal, 2,4-octadiene, 1-chloroheptane, and nonanal in breath samples obtained from exhaled breath samples of COVID-19 infected patients [145], [146]. [154]

2.1.4 Endogenous Compounds of Disease

Although it is currently known that VOCs are emitted from exhaled breath, it was not until the 1970s that one of the first breath studies was carried out. The investigation was directed to approximately 200 VOCs emitted from human breath samples using GC methods [153]. From that point onward, other studies have investigated identifying specific biomarkers of disease for the application of breath analysis. Breath analysis would eventually replace many invasive blood testing procedures with this noninvasive testing method for disease diagnosis [153]. As illustrated in Table 2.2, inorganic gases such as CO, NO, and VOCs such as isoprene, ethane pentane, and acetone are emitted from internal tissue because of the inflammatory response or from oxidative stress because of injury or disease [4], [5]. Studies have detected VOCs associated with infectious diseases such as COVID-19 and Influenza. Acetaldehyde has been detected in the human breath of upper respiratory tract infection (UTRIs) patients; pentane, acetone and isoprene has been detected in the human breath of acute respiratory distress syndrome (ARDS) patients; and nitric oxide (NO) has been detected in human breath of chronic obstructive pulmonary disease (COPD) [4], [5]. Further, pulmonary tuberculosis (TB) patients were found to have elevated levels of heptane detected in their breath sample [26]. Electronic nose devices have been implemented in clinical settings to diagnose diseases based on biomarker signature detection of patient breath samples.

Although other pathogens of disease may share a similar infection mechanism of SARS-CoV-2, it is an important aspect of this research for the combination of more broadly known neurological inflammatory biomarkers, such as NO and CO, from a plurality of pathogens of disease to be incorporated with the known breath pattern signature of COVID-19. The VOCs of COVID-19 currently consist of specific increases in acetone, isoprene, heptanal, propanol,

Table 2.2 Odor analysis of endogenous compounds of disease compared to healthy controls.

<i>Biomarkers</i>	<i>Endogenous Compounds (EC)</i>	<i>EC Type</i>	<i>Expression</i>	<i>References</i>
Lung Disease /Inflammation/ARDS	Pentane	VOC	+	[4], [19]
COPD, Lung Disease/Inflammation	Ethane	VOC	+	[4], [19]
(ARDS), Inflammation	Isoprene	VOC	-	[4], [12], [19]
Inflammation COVID-19 Neurological	CO NO	Inorganic gas	+ +	[38] [19], [43]
Inflammation	Cytokines IL-6 and TNF- α	Nonvolatile	+	[20]
URTI	Acetaldehyde	VOC	+	[4]
COPD, lung inflammation, pulmonary tuberculosis (TB)	Heptane	Hydrocarbon VOC	+	[21] [26]
COPD	2-propanol, 2-butylolctanol	Alcohol	+	[21]
COPD	8-Isoprostane	VOC	+	[4]
COVID-19 Gastrointestinal	Methanol	VOC	-	[98]
COVID-19	Acetone, isoprene, heptanal, propanol, propanal, butanone, octanal, methylpent-2-enal, 2,4-octadiene, 1-chloroheptane, and nonanal	VOC	+ + + +	[28] [98] [145] [146]
Gastrointestinal Motility Disorders	Hydrogen	VOC	+	[99] [98] [100]

propanal, butanone, methylpent-2-enal, 2,4-octadiene, 1-chloroheptane, nonanal, octanal, and a decrease in methanol as shown in Table 2.2 [98], [145], and [146]. In regard to diagnostic electronic nose detection of SARS-CoV-2 infection and COVID-19 disease biomarkers, a breath pattern signature having a wider scope including neurological inflammatory biomarkers is a strategy described here to enhance the accuracy of differentiating COVID-19 infection from other pathogens of disease.

2.2 Brain Breath Biochemistry in Neurological Complications of COVID-19

To date, the direct link between SARS-CoV-2 gaining access to the nervous system through the olfactory nerve to invoke reversible anosmia and COVID-19 induced inflammatory multisystem syndrome remains unexplored and represents a major gap in knowledge about SARS-CoV-2 cellular entry and associated detectable biomarkers of COVID-19. Thus, we propose to elucidate the olfactory nerve's role in viral entry of SARS-CoV-2 to the nervous system and determine quantitative biomarkers associated with its immune response in an effort to gain insights on detecting COVID-19. A highly specified sensor array detection system may be capable of identifying SARS-CoV-2 and/or viral components such as the amino acid receptor binding domains (RBDs) of Spike 1 (S1) glycoprotein of SARS-CoV-2, and/or a plurality of inflammatory biomarkers from the breath of an individual and/or from the odor emitted from an individual. Accordingly, we will probe the role of electrochemical and semiconductor-based detection sensors as well as canine detection of these viral components and/or inflammatory biomarkers under healthy and pathological conditions. [154]

2.2.1 Infection Mechanism of SARS-CoV-2

Studies have indicated that SARS-CoV-2 has four main structural proteins including, spike (S) glycoproteins, a membrane (M), an envelope (E), and a nucleocapsid (N) [58], [39], [37], [72].

These S glycoproteins are embedded on the surface of the outer E portion of SARS-CoV-2 and have a 1273 amino-acid-long structure configured to connect with the human cell membrane protein angiotensin-converting enzyme 2 (ACE2) during infection [51], [52], [39], [73]. Studies have shown ACE2 to be located at various host sites such as at the nasal epithelial cells, the heart, the esophagus, the kidneys, the bladder, and the ileum [62]. The S glycoprotein is divided into subunit 1 (S1) and subunit 2 (S2) [50]. S1 is primarily in communication with ACE2 during infection and has beta strands and comprises an N-terminal domain (NTD), a first C-terminal domain (CTD1), a second C-terminal domain (CTD2), and a third C-terminal domain (CTD3) [54]. The CTD1 functions as a receptor binding domain (RBD) facilitating the connection between S1 and the peptidase domain (PD) of ACE2 [51], [54]. The CTD1 specifically binds to the cellular receptor ACE2. Amino acid residues have unique positioning along the S1 and S2 proteins of a variety of coronaviruses [58]. A variation of 70 interactions found in SARS-CoV-2 S protein and wild-type ACE2 complex exists having ACE2 alleles forming hydrophobic, electrostatic, and hydrogen bonds with SARS-CoV-2 [73]. A strong polar communication exists between SARS-CoV-2 CTD1 of S1 protein residue A475 with ACE2 residue S19, N487 with Q24, E484 with K31, and Y453 with H34 [39], [73].

SARS-CoV-2 binds to the host during infection, and studies have shown evidence that some viral proteins contribute to the suppression of cytokines, interferon (IFN) – α and β of macrophages during immune response [69]. This immune response delay corresponds to the peak of viral load detected in the upper respiratory tract of SARS-CoV-2 patients at day 10 of infection [62], [69]. This suppression of IFN – α and β may contribute to this infection load peak. When the immune system's IFN– α and β finally become active after approximately day 10 of infection, the upper respiratory tract viruses [69]. Studies have revealed SARS-CoV-2 residues including, but

not limited to, V445, Y449, Y473, Q474, A475, E484, G485, F486, and N487 facilitate an increase in has already sustained significant injury, thus, contributing to the increased fatality rate of COVID-19 compared to other electrostatic interactions between S1 protein of SARS-CoV-2 and ACE2 receptor. As a result, a high binding occurs between the ligand S1 protein and the ACE2 receptor [51]. Cryo-EM structure analysis of previous studies have indicated the binding affinity of SARS-CoV-2 S protein to ACE2 is approximately 10–20 times higher than the binding affinity of SARS-CoV S protein to ACE2 [46]. Zinc metalloprotease functions as a receptor molecule for SARS-CoV-2 and is encoded by the ACE2 gene [73].

After the SARS-CoV-2 S1 protein infects an individual by connecting with the ACE2 receiver of an individual, studies have shown indication of a down-regulation of ACE2 prevalence on some cell surfaces [57]. Considering these studies, it is believed that the continued infection and replication of SARS-CoV-2 results in a reduced membrane ACE2 expression. Consequently, the reduced membrane expression of ACE2 expression in the lungs activates neutrophil infiltration of white blood cells in response to bacterial endotoxin, resulting in an influx of angiotensin II accumulation which may increase blood pressure and cause tissue damage [57]. In fact, many CNS infections can result in inflammatory responses including, but not limited to, an increase of neutrophils, mononuclear cells, and neuronal necrosis [34]. Further, biomarkers of cell death include karyorrhexis, condensed chromatin, karyolytic cells, and/or pyknosis which are potential quantitative biomarkers for the detection of COVID-19 [64].

2.2.2 Olfactory Nerve

The cribriform plate separates the nasal cavity from the brain [66]. The goblet cells, secretory cells, and ciliated cells of the nasal epithelium lines the nasal cavity and paranasal sinuses [35]. Olfactory receptor neurons of the olfactory neural cells have a dendritic end portion extending

through the olfactory epithelium of the nasal cavity located opposite an end traversing through approximately 15-20 foramina or openings of the cribriform plate and are connected to the olfactory bulb [53], [34], [66]. The olfactory bulb is positioned within the frontal lobe of the brain and the olfactory tract traverses through the medial temporal lobe of the brain [88]. Next, the olfactory tracts divide at the olfactory trigone into three channels. One of the channels is referred to as the lateral olfactory stria which continues laterally, traversing the horizontal Sylvian cistern and ending at the medial temporal lobe approximately at the uncus [87]. It has been shown that an infection route of SARS-CoV-2 is through the nasal cavity in communication with the medial temporal lobe of the brain by the olfactory bulb [83]. [154]

Some studies have revealed evidence from magnetic resonance imaging (MRI) of the brain of COVID-19 patients revealing signal abnormalities associated with COVID-19 infection at the medial temporal lobe of the brain, which has been shown to retain the olfactory lateral stria [81], [87]. Cerebral white matter fluid-attenuated inversion recovery (FLAIR) hyperintensity lesions show high intensity bright areas on an MRI where a lesion is being reflected. Although these hyperintensity lesions increase with age and with environmental factors such as smoking, they are considered to be a signal abnormality of severe COVID-19 patients [81]. Studies have confirmed that viral particles up to approximately 100 nm can enter the CNS through the olfactory epithelium [34]. Interestingly, clinical investigations of coronavirus-specific viral particles were observed to range in size from 60-140 nm in size [68]. Thus, it has been shown that SARS-CoV-2 is more than capable of infiltrating the CNS through olfactory receptor neurons and traversing the cribriform plate. Studies have indicated infection of the olfactory bulb epithelium as being a contributor in neurological symptoms in that SARS-CoV-2 damages ACE2 and then infiltrates into the blood-brain barrier (BBB) [82]. Interestingly, studies have detected similar viral RNA concentrations

within collection swabs from the nasal epithelium of both symptomatic and asymptomatic patients, thereby, placing viral RNA at the olfactory epithelium during active infection and/or during dormancy [13], [30]. The unique communication of SARS-CoV-2 with the olfactory receptor neurons of the olfactory epithelium may serve the basis of diagnostic sensing devices and/or canine sensing methods configured for pathogen detection and/or pathogen classification of the nervous system.

Some studies have demonstrated the cribriform plate of younger individuals having foramina with a larger sized diameter compared to the cribriform plate of older individuals [66]. In younger children, the cribriform plate is undergoing development and the substantially larger foramina could result in an increased susceptibility to viral infiltration, especially since SARS-CoV-2 is attracted to the ACE2 receptors within the nasal cavity. Studies have indicated that viral transmission along the olfactory nerve is associated with histological lesions [23]. These histological lesions in CNS disease have been known to induce an inflammatory response including, but not limited to, NO mediated demyelination and could trigger COVID-19 induced inflammatory multisystem syndrome [23]. Therefore, NO and CO are potential biomarker candidates for detecting COVID-19.

Although the olfactory nerve is comprised of nonmyelinated axons, the axonal projections of the olfactory bulb that extend to the lateral olfactory tract (LOT) are myelinated [77]. Viral mediated nervous system injury may include demyelination of some portions of the olfactory system. Odorants are captured by olfactory sensory epithelium in nasal respiratory epithelium [38]. Glomeruli located in the olfactory bulb receive electronic impulses associated with an odorant. The first synapse is made with mitral and tufted cells, known as projection neurons [40]. These projection neurons extend into a LOT to an information processing area in the CNS called the

olfactory cortex [77], [38]. The LOT is comprised of axons having promyelinating oligodendrocytes [76], [77], [78]. The myelinated axons of the LOT contribute to an increased membrane resistance, a decreased membrane capacitance, and an increased nerve impulse conduction velocity [77]. Scientific evidence supports regeneration of axons from peripheral nerve injuries by suppressing oxidative stress in oligodendrocytes with acetyl-L-carnitine (ALC) [79]. Olfactory receptor neurons have nucleotide gated ion channels activated by odorant binding, whereby, some volatile odoriferous compounds bind to the mucus layer-odorant binding protein (OBP) in the layer of mucus at the olfactory epithelium surface [38]. Some animal models have suggested mitral and tufted cells have an increased responsiveness to odors when an animal has fasted during detection of the olfactory bulb signals within the gamma band with an electrobulbogram (EBG) [49].

2.2.3 Olfactory Bulb Signal Recording

The olfactory bulb has mitral and tufted cells that generate odor response signals within the gamma band of an electrobulbogram (EBG) scalp recording [49]. A study has investigated the detection and recording of these signals emitted from the olfactory bulb with an electrobulbogram having electroencephalogram (EEG) electrodes positioned on either side of the patient's nasal bridge [49]. Although this method is noninvasive and may serve as an ideal method for diagnosis and monitoring of the olfactory bulb as it relates to brain health in disease and infection, it would be more desirable for an electrobulbogram to have a collection system having electrodes placed within the nasal cavity of a patient for collection of olfactory bulb signals and an analysis chamber for collection and processing of nasally exhaled breath of a patient. Thus, a unique signature may be formed from both the olfactory bulb signals and from the pattern of a plurality of detected endogenous compounds within multiple nasally exhaled breath samples over time. This unique

signature may serve as a method for the diagnosis and monitoring of progression of a plurality of respiratory diseases including, but not limited to, COVID-19.

2.2.4 Volatile Organic Compound Profiles of Lung Disease

Volatile organic compound (VOC) profiles include stable chemicals being volatile at ambient temperature. In some instances, VOCs are produced by an individual because of an infection. Studies suggest that VOCs are transported through the blood from different organs to the lungs, excreted by diffusing across the pulmonary alveolar membrane, and then exhaled through the individual's breath [55]. Many VOCs are detectable in exhaled air and their concentrations in a breath sample may be measured to determine presence of disease [63]. Some VOCs have been identified in studies that have tested the breath of individuals having lung disease compared to healthy individuals. Study results have indicated an increase in VOCs such as, alpha-pyrene, acetaldehyde, 2-butyloctanol, octane, methyl isobutyrate, butanal, 2-propanol, 3-hexanone, cyclopentanone and 3-methyl-propanal, and a decrease of delta-dodecalactone, 2-methyl butanoic acid, 2-acetylpyridine, tetradecane, [E]-cinnamaldehyde, and vinylpyrazine [59].

Some studies showed that the exhaled breath of an individual having disease conditions corresponds to a specific VOC profile [56]. Testing for VOC biomarkers in clinical samples may serve as a noninvasive, point-of-care, and low-cost diagnostic screening method for respiratory diseases. Further, the breath of a SARS-CoV-2 infected individual may have biomarkers which may be detected by a portable gas analysis system configured for rapid and accurate SARS-CoV detection. These biomarkers include, but are not limited to: SARS-CoV-2 spike (S) glycoproteins; endogenous compounds such as NO and CO; VOCs such as ethane, pentane, acetone, isoprene; and nonvolatile substances such as isoprostanes, peroxynitrite or cytokines [8]. Further, studies have revealed measurements of increased levels of Pro-Inflammatory Cytokines (PICs) in the lung

and bronchial tissues of the SARS-CoV-infected ACE2-expressing cells of the epithelial cells, pneumocytes, and macrophages [22]. Some of these PICs include, but are not limited to, monocyte chemoattractant protein-1 (MCP-1) and transforming growth factor beta 1 (TGF- β 1), and intermediate levels of tumor necrosis factor alpha (TNF- α), interleukin-1 β (IL-1 β), and interleukin-6 (IL-6) [22].

2.2.5 Neurological Manifestations of Inflammation

Investigations in the beginning stages have shown that an infection of SARS-CoV-2 does manifest both neurological and neuropsychiatric illness as described in previously mentioned Table 2.2 [80]. The infection mechanism of Guillain-Barre Syndrome (GBS) results in acute inflammatory demyelinating polyradiculoneuropathy lesions from an immune response targeting myelin and/or the axon of the peripheral nerve [86]. Studies have investigated acute demyelinating encephalomyelitis (ADEM) in COVID-19 patients. ADEM is an immune-mediated demyelinating disorder in which pathological evidence suggests that although the brain tissue samples had a negative PCR test for SARS-CoV-2 and that there was no evidence of axonal damage on a neurofilament stain, myelin debris associated with the breakdown of myelin sheaths was detected around vessels in the white matter in the myelin basic protein stain from a brain biopsy [80]. The olfactory bulb and track of the medial temporal lobe, as it pertains to adjacent demyelination, is a likely candidate for facilitating ADEM and/or GBD in COVID-19 patients. Further, it is known that medial temporal lobe atrophy may contribute to retinal thinning, whereby, the retinal nerve fiber layer may be noninvasively scanned with a spectral-domain optical coherence tomography (OCT) [96]. The OCT system may be used in combination with VOC breath signature analysis to more accurately diagnose COVID-19 in infected patients.

2.2.5.1 Nitric Oxide Expression

A recently observed symptom of COVID-19 is anosmia or loss of smell. Studies have shown an increased ACE2 expression in SARS-CoV-2 infection at the location of nasal epithelial cells [33], [35]. Because the S1 proteins of SARS-CoV-2 bind to ACE2 for infection to occur, a strong correlation exists between peripheral nerve injury including virus induced olfactory loss and/or injury stemming from viral communication at the olfactory epithelium, resulting in the anosmia symptom of COVID-19. Studies have identified both an olfactory bulb and olfactory tract volume reduction in size resulting from some respiratory infections and/or diseases such as multiple sclerosis (MS) which display the anosmia symptom [61], [41]. Studies have shown that demyelinating diseases have an increased inflammatory response compared to non-neurological diseases. Further, the atrophy of both the olfactory bulb and the olfactory tract was shown to be more pronounced in MS in relation to both demyelination and parenchymal inflammation [41]. Hence, this atrophy of the olfactory bulb and olfactory tract might be correlated with demyelination, which could trigger an inflammatory response with potentially fatal outcomes in patients. This inflammatory response induced from both COVID-19 and MS can be detected through volatile organic compound (VOC) brain breath analysis with an electronic nose device.

Although, the majority of anosmia observations reported in COVID-19 diagnosed cases appear to be caused from mucosal congestion, peripheral nerve injury could explain anosmia in asymptomatic COVID-19 patients not having mucosal congestion [61]. In particular, because of the inflammatory response of SARS-Cov-2 connecting with ACE-2 at the olfactory epithelium, macrophages and microglia may be activated to generate cellular debris such as, inflammatory cytokines and nitric oxide (NO) which contribute to demyelination and axonal loss [65]. NO has been shown to damage mitochondria of axons [74], resulting in lower levels of the enzyme Na⁺/K⁺

ATPase, an ATP supply deficiency, and an increase in the amount of Na⁺ within a cell. The olfactory sensory neurons have unbranched dendrites that connect with the olfactory epithelium. The cytoplasm of the dendrites is configured to retain mitochondria and the ends of these dendrites form olfactory knobs [40]. The ATP production is crucial for nervous tissue to have stable resting potentials to propagate electrical signals to transverse the length of nerve fibers. Therefore, nervous tissue requires ATP to generate resting potentials.

When the ATP is broken down into adenosine diphosphate (ADP) and phosphate, the Na⁺/K⁺ pumps become activated again to reverse the influx of Na⁺ within the cell. There may be a correlation between anosmia as a symptom of COVID-19 with the NO mediated injury to the olfactory receptor neurons. Additionally, COVID-19 induced inflammatory multisystem syndrome may result from an inflammatory response from this aforementioned peripheral nerve injury. Thus, understanding the biomechanism of anosmia may provide anosmia specific biomarkers capable of being added to the known breath pattern signature of COVID-19 currently consisting of increases in acetone, isoprene, heptanal, propanol, propanal, butanone, octanal with a decrease on methanol, thereby, differentiating COVID-19 infection from other pathogens of disease [98]. The incorporation of additional biomarkers from the anosmia symptom of COVID-19 contributes to the unique exhaled breath profile of COVID-19 to increase the accuracy of a diagnostic electronic nose for exhaled breath applications.

Although the epithelium of the paranasal sinuses produces NO even without viral infection, macrophages generate excessive NO because of proinflammatory cytokine activation during viral infection defense [43], [47]. When NO and oxygen free radicals (OH) and (O₂⁻) are in communication with each other from some viral lung infections, toxic byproducts such as peroxynitrite (ONOO⁻) and NO_x (NO₂ and N₂O₃) are seen to contribute to the mechanism of viral

pneumonia resulting in tissue injuries to the lungs [42], [47]. Further, scientific evidence has indicated measurable amounts of NO in nasally exhaled air [44]. Thus, excessive levels of NO may be a biomarker of inflammation especially when a biosensor collects breath samples from nasally exhaled air as opposed to orally exhaled air. [154]

2.2.5.2 Carbon Monoxide Expression

Multisystem inflammatory syndrome is a disease that has recently been observed in children and teens that had previously tested positive for COVID-19. Some of the symptoms include, but are not limited to, body inflammation, rash, high fever, upset stomach, and cardiac dysfunction. Studies have indicated proinflammatory cytokines such as tumor necrosis factor-alpha (TNF- α), interleukin-6 (IL-6), and IL-8 having increased levels detected after being stimulated for inflammatory response and having increased levels as age increases [70], [45]. Thus, younger individuals will have less of a protective inflammatory response compared to adults, which may contribute to COVID-19 related multisystem inflammatory syndrome.

It is currently known that NO is a biomarker of airway inflammation [19]. It is a possibility that COVID-19 induces NO mediated demyelination of the axons of olfactory receptor neurons. An example of energy failure of a neuron in CNS diseases can be caused by deficient Sodium Potassium (Na⁺/K⁺) ATPase. The enzyme Na⁺/K⁺ ATPase is responsible for the pumping of Na⁺ and K⁺ in opposite directions across the cell membrane [74]. When ATP supply is deficient, the enzyme Na⁺/K⁺ ATPase loses its function. Without the breakdown of ATP to energize the Na⁺/K⁺ pumps, these Na⁺/K⁺ pumps can fail. When these Na⁺/K⁺ pumps are impaired, it results in an increase in the amount of Na⁺ within the inside of the cell from the Na⁺/K⁺ pumps losing their ability to export Na⁺ from the cell. Thus, energy failure of the neuron and degeneration of

demyelinated axons may occur in response to viral mediated CNS when ATP supply is deficient and may result in COVID-19 induced inflammatory multisystem syndrome [74], [125].

Similarly, energy failure of the neuron results from Ca^{2+} mediated injury to myelinated axons when an increase in the amount of Na^{+} is retained within the inside of the cell [74]. When there is an influx of Na^{+} inside of a cell, the reverse operation of the Na^{+} - Ca^{2+} exchanger is activated, thereby, importing excessive levels of Ca^{2+} into the axon. Ca^{2+} mediated injury includes, but is not limited to, fragmented neurofilaments, depolymerized microtubules, or a lowering of organelles of residual demyelinated axons [61]. An influx of Ca^{2+} occurs as a result from both ATP depletion and from odorant binding. For example, in odorant binding, cyclic adenosine monophosphate (cAMP) causes a depolarizing flow of current into olfactory receptor neurons, which slows odorant stimulation by closing cyclic nucleotide-gated (CNG) channels [38]. Studies have evidence supporting CO as the diffusible intracellular and intercellular biomarker of CNG channel activity in olfactory receptor neurons. Thus, CO is a byproduct of olfactory transduction associated with CNG channel activity reduction, whereby, a loss of olfactory receptor neurons occurs for minutes [38]. These excessive concentrations of CO byproduct may be detected by a gas sensor and compared to CO concentrations of healthy individuals.

2.3 Electronic Nose Technology

Currently, diagnostic testing of many diseases often requires invasive means such as tissue biopsy, post-mortem microscopic testing, blood collection, and/or implantable electrodes. It is more desirable for the breath profile of a human to be non-invasively analyzed for the presence of disease specific biomarkers including a plurality of endogenous compounds for clinical disease screenings, diagnosing disease, and monitoring disease progression in humans. In particular, some eNose devices utilize gas chromatography and mass spectrometry and are capable of detecting

various odors and toxic substances. The use of biosensors eliminates many ethical considerations that may arise with either human or canine detection of infectious disease or biohazardous material. Although studies have shown biosensors being capable of detecting odor associated with immune responses, biosensors lacked specificity and have signal suppression due to poor data processing and a noisy signal. Table 2.3 shows a broad scope of eNose devices and their respective materials and methods including the locations monitored, target gas discrimination, and sensor type.

2.3.1 Space Shuttle Air Quality Monitoring

Early eNose devices such as those that have been developed for air quality monitoring at the NASA Jet Propulsion Laboratory (JPL) have 32 conductometric sensors made from carbon loaded insulting polymer films in communication with a computer [23]. The computer obtains sampled data from a database of air samples, independent component vectors are generated to represent each subset of the sampled data, and each subset of sampled data undergoes independent component analysis whereby, each subset of sampled data is linearized using a plurality of specific operating points by subtracting the averaged value from each element to determine the data distribution. This method of air quality monitoring involves complex mathematical modeling and lengthy algorithms for the response pattern extraction and for the pattern recognition of gasses such as, methanol, ethanol, 2-propanol, ammonia, benzene, indole, methane, formaldehyde, Freon 113, and toluene [23]. The JPL eNose is configured for use in a space shuttle setting and is not conducive to the widespread, rapid diagnostic testing of the public for COVID-19. Thus, there remains a long felt, yet unfulfilled need for an improved eNose capable of measuring the air quality from the breath of an individual at point-of-care for a rapid diagnosis for COVID-19.

Table 2.3 Electronic nose devices with target gas discrimination and gas sensor type.

Electronic Nose Devices	Location Monitored	Target Gas Discrimination	Sensor Type	References
Jet Propulsion Laboratory (JPL)	Air Quality	Gasses such as, methanol, ethanol, 2-propanol, ammonia, benzene, indole, methane, formaldehyde, Freon 113, and toluene	32 conductometric sensors made from carbon loaded insulting polymer films	[23]
Wize Sniffer with Mouthpiece	Liver Dysfunction	Carbon monoxide, carbon dioxide, hydrogen, ethanol, hydrogen sulfide, hydrogen, and ammonia	6 metal oxide semiconductors (MOS)	[1]
Cyranose 320 eNose	Diagnosing White-Nose Syndrome in bats	6 alcohols including methanol, ethanol, 1-propanol, 2-propanol, 1-butanol, t-butanol; six aldehydes; 2 amines; four ketones; and four carboxylic acids	32-sensor array with carbon black polymer composite sensors/conducting polymers	[2]
Gas Chromatography and Mass Spectrometer (GC-MS)	Fruit Quality Monitoring	Aldehydes, alcohols, esters, ketones, and terpenoids	12 chemical tin oxide sensors/8 MOS sensors	[3]
Gas Chromatography and Mass Spectrometer (GC-MS)	Fruit Quality Monitoring	Acetone, n-hexane, benzene, ethanol, isobutane, carbon monoxide, and methane	13 MOS gas sensors	[3]

2.3.2 Detectable Breath Ammonia and Liver Health

Liver dysfunction is detectable by measuring quantities of ammonia in the breath of a patient with an eNose device referred to as the Wize Sniffer. The gas sensor array is retained within the gas collection chamber and has six MOS based sensors. The MQ7 sensor detects carbon monoxide and hydrogen, the TGS2620 sensor detects carbon monoxide, hydrogen, and ethanol, the TGS2602 sensor detects ethanol, hydrogen sulfide, hydrogen, and ammonia, the TGS821 sensor detects hydrogen, the TGS2444 sensor detects ammonia, and the TGS4161 sensor detects carbon dioxide [1]. A mouthpiece is connected to the gas collection chamber and is configured for a user to exhale a single breath as per the mixed expiratory breath sampling technique from the user's mouth into the mouthpiece. The cited study indicated the need to establish a clearly defined boundary of the best detection range in parts-per million to differentiate patients having liver disease from healthy controls.

2.3.3 Air Collection Devices for Breath Emissions in Bats

A study investigating the presence of a fungal pathogen, *Pseudogymnoascus destructans*, in bats utilized the portable Cyranose 320 eNose for diagnosing White-Nose Syndrome in bats [2]. Each species of bat was placed inside of the air collection chamber for a time of 10 minutes and the sample was processed with the VOC pure chemical standards for a sixty second run time [2]. The Cyranose 320 has a 32-sensor array with carbon black polymer composite sensors with conducting polymers. The sensor sensitivity to VOC analytes of the air collection chamber retaining the bat is configured to detect the following: six alcohols including methanol, ethanol, 1-propanol, 2-propanol, 1-butanol, t-butanol; six aldehydes; 2 amines; four ketones; and four carboxylic acids. The VOC signatures were detected from nine different bat species and stored into a database. 3-Dimensional Principal Component Analysis (PCA) includes the spatial

distribution of the unique VOC profiles detected from differences in the intensity and polarity of the sensor array of the eNose in six different bat species [2]. The composition of the VOC metabolic eNose data were statistically analyzed and plotted to show both VOC types and measurable quantities detected by the eNose.

2.3.4 Metal Oxide Semiconductor Gas Sensors in Fruit Industry

There have been a number of studies that describe a variety of VOCs using a gas chromatography and mass spectrometry (GC-MS) in the farming industry to monitor the freshness and quality of peaches. VOC detection of aldehydes, alcohols, esters, ketones, and terpenoids emitted from Eragil peaches at different concentrations depending on the date range of peach growth after full bloom are known [3]. One eNose sensing device has 12 chemical tin oxide sensors and 8 MOS sensors configured to measure the degree of peach ripeness and freshness. Another eNose device has 13 MOS gas sensors such as TGS822 configured to detect acetone, n-hexane, benzene, ethanol, isobutane, and methane; TGS2600; TGS2602; TGS2603; MQ-2; MQ-3, MQ-4, MQ-5, MQ-6, MQ-7 is configured to detect carbon monoxide having a detection range of 20-200 ppm, MQ-9, and MQ-135 [1],[3]. This eNose has a fan configured to move the flow of air carrying VOCs emitted from a peach into a chamber. The air flow is then heated for 10 minutes prior to the air coming into contact with the sensor array, whereby, electrical signals are read through a 10-bit analog-digital converter (ADC) into the microcontroller [3]. The digital signals from the sensor array may be wirelessly transferred and/or stored as data into a computer database. In addition to the MOS-based MQ-7 sensor for carbon monoxide (CO) detection of the Wize Sniffer device, another known CO gas sensor comprises reduced graphene oxide (rGO)/Fe₃O₄ nanocomposites having an interdigitated chromium electrode capable of high selectivity for detection of CO gas

[6]. This sensor detected 5 ppm of CO gas in 3.59 seconds and detected 50 ppm of CO gas in 8.78 seconds [6].

2.3.5 Electronic Nose Detection of Chronic Rhinosinusitis

Some common gas sensor technology in eNose devices includes amperometric electrochemical (AEC), field effect transistor (FET), quartz crystal microbalance (QCM), and surface acoustic wave (SAW) sensors [9], [11]. An eNose device using acoustic wave technology with gas-chromatography (GC) and SAW capability is referred to as a ZNose. The ZNose has a heated inlet and a vapor pre-concentrator configured to output a pictogram of a quantity of 6 peaks associated with detected VOCs of nasal infections such as, chronic rhinosinusitis (CRS) within 10 seconds from invitro cultured cells [5], [25], [26]. The breath collection technique implemented with this ZNose required the use of a cotton swab positioned for 5 minutes within the middle meatus of a nasal fossae for collection of nasal secretions of 14 healthy controls and from 14 CRS affected individuals [25]. The intensity and quality of the detectable endogenous compounds of this study are biomarkers of bacterial and/or fungus induced sinus infections.

Investigations suggest odors emitted from the nasal exhalation of a patient having CRS are a result of the load quantity of bacteria and/or fungus within the nasal cavity and from the metabolic process of pathogenic infiltration of the bacteria and/or fungus into the nasal cavity. One eNose device has an array of 5 SAW resonators having 3 odorant binding proteins connected thereto. The SAW resonators are configured for detection of vapor-phase odorant molecules of octenol and carvone [7], [10]. In another study, biological agents such as sarin, ricin, and anthrax were detected with a biosensing system comprising a mist-generator integrated within an air collection chamber, as the biosensors require the sample reagent to be dissolved in water [8]. A glycol chip in communication with the air collection chamber is configured for localized surface

plasmon resonance (SPR) processing, whereby, gold nanoparticles are configured to connect the biological agent or analyte to the ligand mounted on the chip. SPR monitors binding events between a receptor of a biological agent and a ligand. This eNose technology provides binding, kinetics, specificity, and concentration, without the need for labels and is ideal for detecting viruses such as SARS-CoV-2. A glass slide is provided. A layer of gold film or nanoparticles overlays the glass slide. A dexamethasone (dex)-strand matrix functions as a substrate to which molecules can be attached. A ligand is connected to the dex-strand on the chip. The analyte then binds to the ligand. SPR causes a reduction in the intensity of light reflected at a specific angle from the glass side of the sensor surface. As binding occurs the refractive index close to the surface changes, which alters the angle of minimum reflective intensity.

In another CRS study, 5 nasally exhaled breath samples were obtained from healthy controls and were compared to 5 nasally exhaled breath samples from CRS affected individuals. A plastic collection sack comprising a rubber tube connected to a bifurcated nasal tube has a valve, whereby, the bifurcated nasal tube is positioned within the nostrils of the study participant and the plastic collection sack is filled with nasally exhaled air [27]. Processing of the collected breath samples was accomplished with 8 quartz microbalance sensors configured to produce a molecular composition-based pattern qualitatively classified using principal component analysis (PCA) having an 80% successful classification rate and artificial neural network (ANN) analysis having a 60% successful classification rate [5], [26],[27]. Because some biomarkers of disease result from an immune mediated response, studies indicate metabolic byproducts specific to the infiltrated pathogen, thus, a unique signature of metabolic biomarkers may be detectable with an eNose device [4], [25].

2.3.6 Field-Effect Transistor Biosensor Detection of SARS-Cov-2

The detection of SARS-CoV-2 may be accomplished with a glycan-based or graphene-based field-effect transistor (FET) biosensor [37], [97]. A study has indicated the biosensor comprises graphene sensing material having a SARS-CoV-2 S antibody in communication with the graphene having a 1-pyrenebutyric acid N-hydroxy succinimide ester probe linker. FET based biosensors have a high sensitivity and immediate results [37]. Graphene is utilized for its high electronic conductivity, increased carrier mobility, and increased specific area [37]. The SARS-CoV-2 S antibody was used as a receptor to detect SARS-CoV-2. In a study, an undisclosed SARS-CoV-2 antibody is evaluated for its limit of detection on the graphene surface of the FET biosensor which detected 1 femtogram per milliliter (fg/mL) which measures concentrations of SARS-CoV-2 S protein in phosphate-buffered saline in parts per quadrillion [37]. In another experiment, the FET biosensor was evaluated for its limit of detection on the graphene surface with cultured SARS-CoV-2 which detected concentrations 1.6×10^1 pfu/mL and in clinical nasopharyngeal samples, the FET sensor detected concentrations $1:1 \times 10^5$ (242 copies/mL) [37]. The study concluded that further research was required to determine materials having a more reduced associated noise.

2.3.7 Nanocrystalline Metal Oxide Film Sensor for Influenza Detection

The metabolic processes involved with inflammatory responses and oxidative stress of diseases produce byproduct biomarkers such as, NO and CO, whereby, some of which are expelled in the exhaled breath of an infected individual at an altered composition and concentration compared to healthy controls [16], [17], [18], [26]. It is this difference in concentration of a plurality of biomarkers in disease that creates a signature pattern, whereby, a detected biomarker may have markedly increased levels of concentration or decreased levels of concentration compared to a healthy control, that may be used to differentiate healthy controls with infected

individuals. For example, some studies have investigated the detection of influenza induced infection by monitoring levels of isoprene, NO, acetone, and/or ammonia in exhaled breath of an individual with an eNose device [12]. In particular, an isoprene sensor device configured for an individual to orally exhale a single breath into a mouthpiece is connected to a chamber in communication with a sensor having a Bluetooth interface integrated within a printed circuit board (PCB) [12]. This isoprene sensor comprises a nanocrystalline metal oxide film configured to monitor viral infections by detecting a plurality of exhaled biomarkers simultaneously over time. In another study, a NO sensitive single exhale breath sensor is configured to communicate with a PCB having a breath sample chamber and sensor circuitry [15].

2.3.8 Gas Chromatography for Inflammatory Lung Disease Detection

Central nervous system (CNS) infections result in immune-mediated responses such as inflammation. Scientific data from several studies indicate that hospitalized patients having COVID-19 also develop acute respiratory distress syndrome (ARDS) [35]. As a result of infected individuals having these aforementioned highly pathogenic coronaviruses, the lung and bronchial tissues may be susceptible to acute lung injury (ALI) and ARDS, which are associated with chronic and acute inflammation [22]. Some studies suggest that exhaled concentrations of ethane and lipid peroxidation biomarker, pentane were measured at increased levels in inflammatory diseases [19]. Other studies have revealed that isoprene is another biomarker having a presence in inflammatory lung disease [19]. In particular, the exhaled breath of individuals infected with bacterial RTI was analyzed for VOC concentrations with the GC-IMS sample collection, whereby, patients orally exhaled the last 3 seconds of the exhaled breath into a mouthpiece directly connected to the device after 30 minutes of fasting [13]. The IMS is configured to detect separation of chemicals within the GC with a sensitivity in the parts-per trillion (ppt). Further, the 10-minute analysis time for

each sample was implemented. Some data associated with the GC-IMS was processed for machine learning applications to reduce noise and to correct the baseline of 30 recorded VOCs including, but not limited to, ethanol, benzene, octane, and hexanal [14]. Although GC-IMS is considered to be a leading standard test for exhaled breath analysis due to its high specificity of identifying VOCs of varying metabolic processes, GC-IMS technology requires lengthy processing times in addition to technical requirements, involving skilled technicians to process the sample, which is not an ideal approach for diagnostic VOC profiling [148], [149]. Electronic noses have been shown to successfully recognize complex VOC mixtures from a sample breath indicative of a metabolic process in respiratory diseases.

Many electronic nose devices comprise an electronic chemical sensor array configured for detection of a target gas, such as VOCs, and implements pattern recognition to differentiate the target gas from a diversity of gasses [149]. Current existing electronic nose technologies have been developed and investigated for their diagnostic performance in respiratory diseases including, but not limited to, inflammatory lung disease such as asthma [147], [148]. For example, the Cyranose 320 is an electronic nose having a carbon black-polymer sensor array [147]. Studies have investigated the performance of the Cyranose 320, configured for 96% accuracy in distinguishing patients with asthma from patients with COPD [148]. Another study indicated the Cyranose 320 could differentiate patients having mild asthma from patients having severe asthma at a cross-validation value (CVV) of 65% [147], [150]. In yet another study, the Cyranose 320 was shown to discriminate between healthy controls, controlled asthma, and partially controlled and uncontrolled asthma with an AUC (Area Under the Curve) ROC (Receiver Operating Characteristics) curve of 85%, a sensitivity of 79%, and a specificity of 84% [147], [151]. The Aeonose is an electronic nose device having micro hotplate metal-oxide sensors and demonstrated

a lower accuracy and sensitivity compared to the Cyranose 320 when discriminating asthma from healthy controls, whereby, the Aeonose performance results indicate an AUROC curve of 79%, a sensitivity of 74% , and a specificity of 91% [147]. [154]

This section presented a review of VOCs and their means for detection. First, symptoms and diagnostic testing methods of COVID-19 were described. Then endogenous compounds of diseases, such as COVID-19, were presented to provide an indication that detectable VOCs are emitted from infected individuals. Next, brain breath biochemistry in neurological complications of COVID-19 were discussed. The SARS-CoV-2 infection mechanism, olfactory nerve route, and inflammatory biomarkers of inflammation provided a biological perspective of COVID-19 infection and potential VOC targets for an eNose device to detect. Finally, structural components of differing electronic nose devices were reviewed in varying applications such as, in space shuttle air quality monitoring, for measuring breath ammonia, for monitoring liver health, for monitoring fruit ripeness in the citrus industry, and for monitoring breath emissions in bats. Further, performance results configured for use in diagnostic breath analysis applications that have shown moderate to good accuracy in providing a rapid detection of the breath pattern of biomarkers of respiratory disease. Electronic noses may also be usefully extended to diagnostic applications of other inflammatory and infectious diseases such as in chronic rhinosinusitis, influenza, and inflammatory lung disease [149]. Due to their portability, ability to rapidly provide point-of-care diagnostic test results without a laboratory technician and their relatively low cost elevate the electronic nose to an attractive diagnostic tool in breath analysis.

Chapter 3: Materials and Methods

A portion of this chapter was published in [124] and was accepted for publication in [154]. Permission to reproduce the works in this Dissertation is included in Appendix A.

A major limitation in this study was the inaccessibility to certain gas sensors and electronic nose systems because of state and locally mandated business closures in response to the 2019 novel COVID-19 pandemic during the timeframe of April 2020-May 2021. This study was limited to MQ sensors due to their commercial availability when potentially more suitable gas sensors were currently unavailable. A testbed prototype of an electronic nose device having a sampling chamber in communication with an MQ-2 gas sensor and an MQ-135 gas sensor was designed and built. In addition, all proposed laboratory-based research involving SARS-CoV-2 virus at USF requires the use of either a Biosafety Level (BSL) 2 or a BSL-3 facility. At the time of this study, the USF BSL-2 and BSL-3 facilities were not accessible due to either closures and/or long wait lists. Thus, this study was not able to work with viral cultures to determine VOCs firsthand and was limited to information obtained through the literature review in regard to VOCs of COVID-19.

COVID-19 breath samples were not obtained by researchers of USF for this Dissertation research because of the deadly risk of researchers being contaminated by and/or transmitting COVID-19 via exhaled breath. The exhaled breath collection process would have generated SARS-CoV-2 contaminated aerosols and/or droplets. Research collaborators provided this Dissertation research with data from clinical breath studies located in Loughborough, UK, and Dortmund, Germany. The results of the literature review and these breath studies done by research

collaborators revealed that some of the major components of COVID-19 positive breath samples contained acetone, alcohol, and CO as previously described in Table 2.2. This study formulated and tested a COVID-19 breath simulation solution of acetone, alcohol, and CO. Although these formulation ingredients are based on literature review and COVID-19 breath analysis results, the formulation ingredients are subject to change as more study results are obtained [98].

3.1 Electronic Nose Gas Detection Experiments

Acquired gas data presented in this Dissertation was obtained from an experimental test bed prototype illustrated in Figure 3.1 comprising an electronic nose having a breath collection vessel with a first check valve and a second check valve. The first check valve located at the top

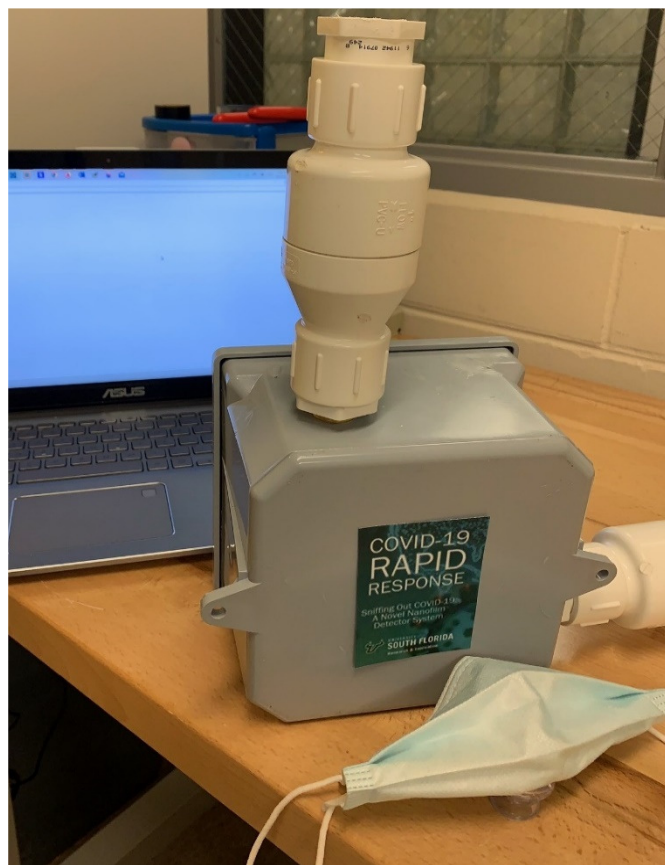


Figure 3.1 Electronic nose prototype comprising a breath collection vessel, a mask, and a computer.

of the housing allows exhaled breath to enter the collection chamber. The first check valve is configured for a patient to breath into through a one-way valve of a mask. A specialized mouthpiece was built to comprise a mask and a one-way valve having a filter so that an individual could provide a breath sample into the collection vessel without having to remove a mask barrier member from their face due to COVID-19 precautions. The second check valve located on the side of the housing allows exhaled breath to escape the collection chamber, therefore, purging the collection chamber of encased exhaled breath. Thus, the exhaled breath is trapped within the collection chamber and is positioned between the first check valve and the second check valve. The gas sensors are retained within the collection chamber of the housing and a microcontroller is in electrical communication with a computer.

It is envisioned that sterilization elements such as ultraviolet-C (UVC) light emitting diodes (LEDs) can be incorporated into the conceptual design of the breath sample chamber and the exhaust or output valve can be connected to a filtration system to purify the air being purged from the breath collection chamber. However, the design limitation did not include these limitations due to lack of adequate funding and time restraints directed to the completion of this study. Further, as previously mentioned, although a limitation of this study focused on obtaining data from a simulated breath sample solution rather than from a clinical breath sample, future opportunities with additional funding and IRB approval will allow this experimental test bed prototype for clinical use in obtaining exhaled breath samples of COVID-19 infected individuals.

Figure 3.2 illustrates a side cut-away view of the electronic nose housing retaining electrical components and gas sensing components retained within an internal bladder being in communication with a sample vessel, compressed oxygen carrier gas, and a flowmeter. In particular, two MOS gas sensors are retained in the chamber of the housing. These sensors are

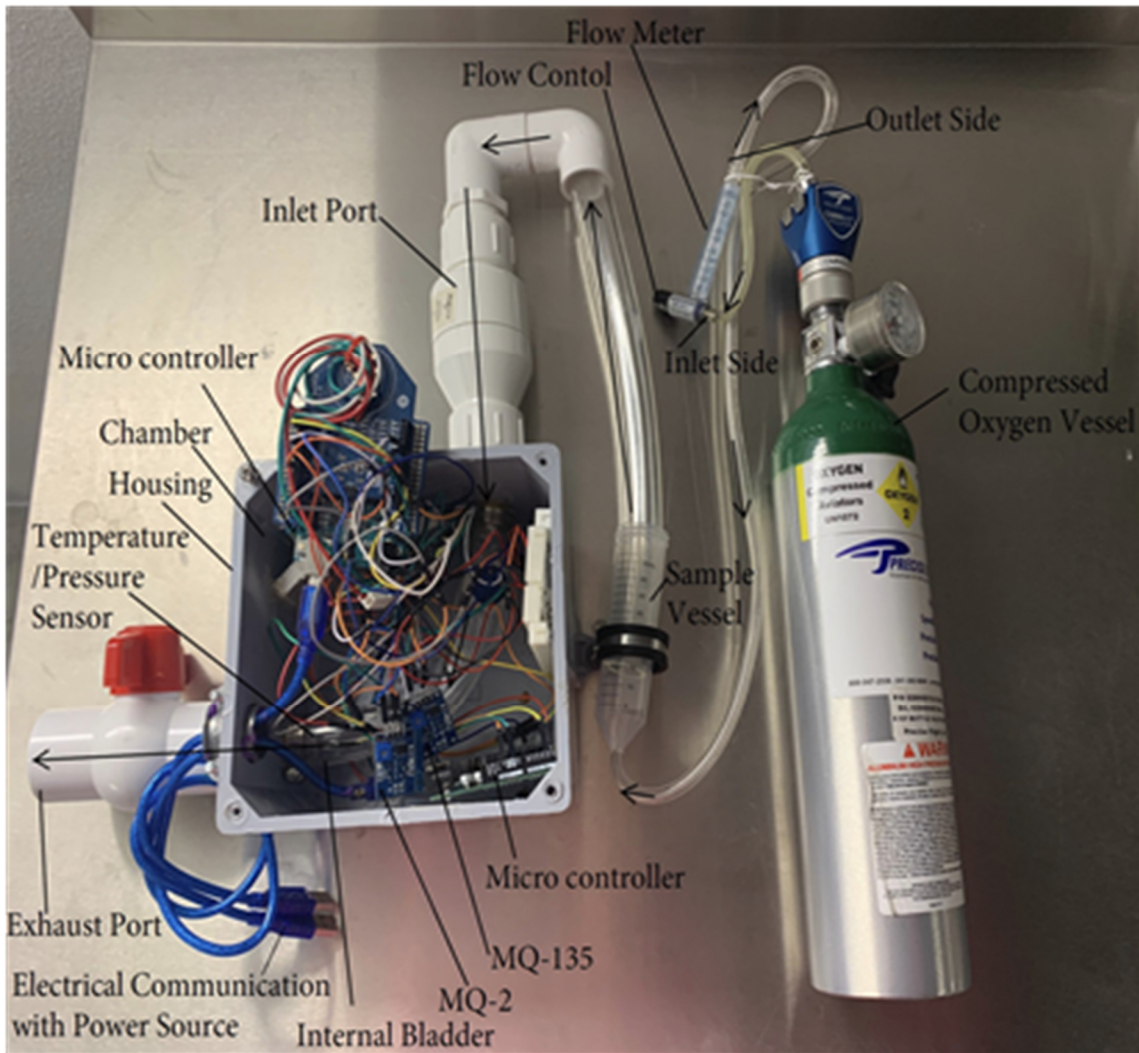


Figure 3.2 Electronic nose having gas sensing components retained within an internal bladder being in communication with a sample vessel, compressed oxygen carrier gas, and a flowmeter [124] © 2021 IEEE.

capable of being saturated by a target gas to then produce a resistance change across the sensors resulting in an output response in volts (V). The MOS-based sensors are capable of detecting gas concentrations in parts-per-million (ppm) of CO, acetone, and alcohol. Referring now to Figure 3.3, the COVID-19 breath simulation solution has equal parts of liquid methyl alcohol and liquid acetone mixed together. The solution is within an airtight sample vessel. Compressed CO gas is emitted from a controlled high pressure aluminum cylinder in communication with the gasses emitted from the sample vessel retaining the liquid alcohol and the liquid acetone solution. The

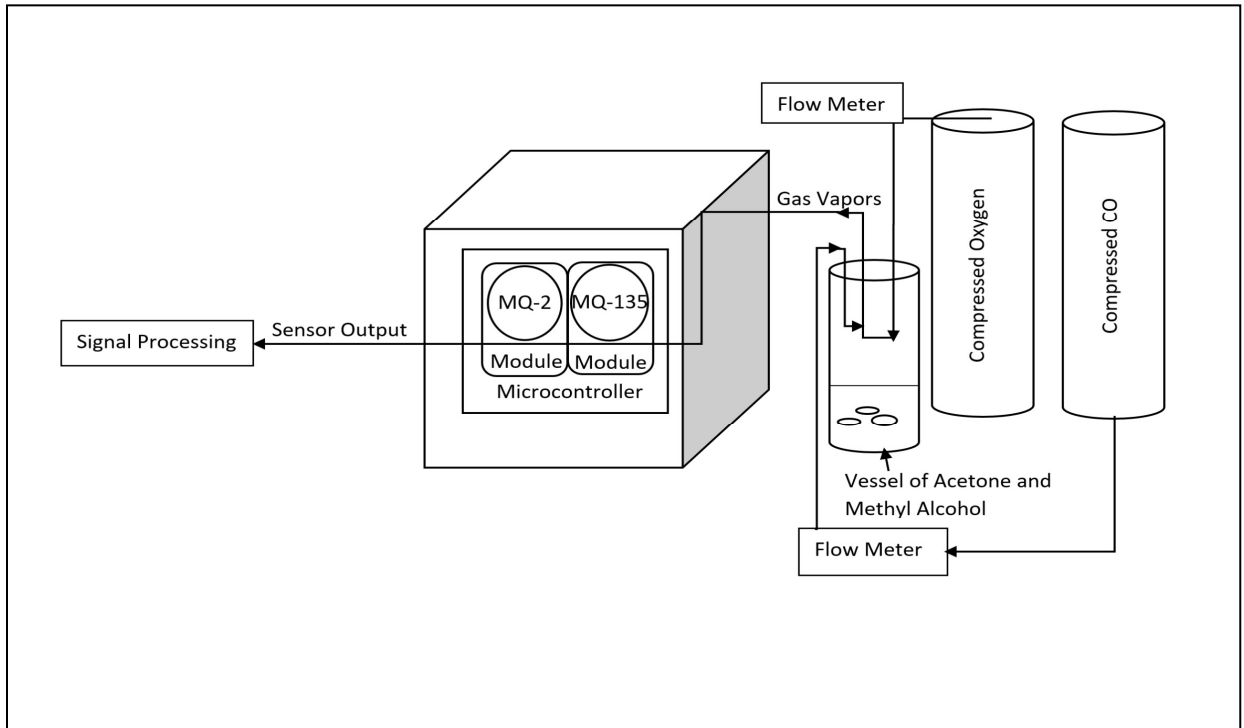


Figure 3.3 Schematic diagram of the experiment comprising a testbed prototype having MQ-2 and MQ-3 gas sensors.

concentration of the COVID-19 breath simulation solution in oxygen carrier gas is controlled by a model A-5 In-Line Dual Scale Flowmeter. The flowmeter is in communication with a compressed oxygen carrier gas so that the flow rate of COVID-19 breath simulation solution having equal parts of acetone, CO, and methyl alcohol remains continuous across the gas sensors. Varying concentrations of methyl alcohol and acetone of the COVID-19 breath simulation solution were subsequently introduced and retained by a sample vessel. Different concentrations of CO were generated by modifying the percentage of the CO flow rate over the total flow of COVID-19 breath simulation solution. The gas sensors were retained within an internal bladder of a housing to maintain a continuous climatic environment [124].

3.1.1 COVID-19 Breath Simulation Mixture

Studies have indicated measured concentrations of CO emitted from the breath of non-COVID-19 individuals as having approximately 2 ppm-100 ppm of CO present in their exhaled

breath [19], and [126]. Although SARS-CoV-2 is considered a respiratory illness, scientific evidence demonstrates that viruses may utilize the olfactory nerve to infiltrate and damage the nervous system including the central nervous system (CNS) and/or the peripheral nervous system (PNS) by activating T-lymphocytes which then activate microglia and inflammatory mediators [84], [90], [69], [80], [81], [82], [86]. Nervous system damage is associated with disease specific metabolites and abnormal chemical biomarkers that are emitted into the air from soft tissue samples and body cavities such as, the lungs and/or the nasal cavity, which may be detected in the breath of an individual with an eNose sensor configured for diagnostic screening for COVID-19 [4], [34], [57], [45].

Referring to Table 3.1, in addition to carbon monoxide being an inflammatory biomarker, preliminary data obtained from parallel COVID-19 breath studies, based in Edinburgh and Dortmund, have indicated statistically significant concentrations of methanol gas which is an alcohol and a ketone gas being acetone, using gas chromatography-ion mobility spectrometry (GC-IMS), as being capable of discriminating between patients with COVID-19 and healthy individuals [98]. For example, at the Royal Infirmary of Edinburgh (RIE), a participant's COVID-19 positive breath sample was collected within the GC-column to separate the plurality of compounds of the breath. Next, the plurality of compounds was ionized, whereby, the ions exhibited a characteristic drift time determined by the detector based on properties such as mass and charge [98]. Referring again to Table 3.1, detected exhaled methanol monomer and methanol dimer concentrations have a relative drift time of 0.99 ms and 1.036 ms, respectively, whereby, signal processing of GC-IMS data with MATLAB and statistical analysis indicated a lower methanol signal volume emitted from exhaled breath of RIE COVID-19 positive participants compared to non-COVID-19 exhaled

Table 3.1 VOC concentration trends in exhaled breath of healthy samples compared to viral infiltrated samples [124] © 2021 IEEE.

VOC type	Sensor type		VOC measured values emitted from non-COVID-19 breath	Relative drift time in GC-IMS of RIE samples of COVID-19 breath	References
Acetone	MQ-135		0.24 ppm-1.69 ppm	1.159 ms	[15], [16], [17]
Methanol Monomer-Alcohol	MQ-2		0.4 ppm-2.0 ppm	0.99 ms	[15], [17]
Methanol Dimer-Alcohol	MQ-2		0.4 ppm – 2.0 ppm	1.036 ms	[15], [17]

breath samples [98]. Although this aforementioned RIE study resulted in an identification of a decreased concentration of methanol in the exhaled breath of COVID-19 positive participants using GC-IMS and did not use a gas sensor capable of detecting methanol concentrations in ppm, the results contribute to our understanding of the COVID-19 exhaled breath pattern signature.

Table 3.1 further shows detected exhaled acetone concentrations having a relative drift time of 1.159 ms, whereby, signal processing of this GC-IMS data with MATLAB, preliminary modeling, and statistical analysis indicated an increased acetone signal volume emitted from exhaled breath of RIE COVID-19 positive participants compared to non-COVID-19 exhaled breath samples, corresponding to an increased concentration of acetone in COVID-19 positive participants [98]. It is currently known that environmental contaminants exist in both the ambient

air and/or an exhaled breath sample. For example, Table 3.1 shows concentrations of acetone in non-COVID-19 exhaled breath samples having a detected concentration range between 0.24 ppm-1.69 ppm [98]. Hence, a gas sensor, such as the MQ-135, capable of detecting acetone at levels exceeding 1.69 ppm is desirable for the application of detection of breath acetone levels. In addition, the reduction of environmental contaminants within ambient air can be reduced and/or eliminated with an air tight sample collection and processing system. Thus, the simulated breath sample solution of this current Dissertation was based on breath studies and comprises equal parts of CO, alcohol and acetone within an air tight sample collection and processing system [98]. Appendix D shows IRB approval was not required for this Non-Human Subject Research.

3.1.2 Design and Assembly of the Gas Sensor Array Test Bed Prototype

Circuitry of the first Arduino Uno microcontroller electrically connects to the MOS-based MQ-2 and MQ-135 gas sensors produced by Hanwei Electronics CO., LTD with sensor modules produced by Flying-Fish company and the second Arduino Uno microcontroller is electrically connected to a Bosch BME280 sensor configured to measure pressure and temperature within the chamber of the housing. The housing chamber retains an internal bladder which connects the input port of the electronic nose to the exhaust port of the electronic nose to separate the microcontrollers and electronic circuitry from the gas obtained from the sample solution, whereby, at least a portion of the BME280, MQ-2 sensor is configured to detect both CO and alcohol, and an MQ-135 sensor is configured to detect acetone and are retained within the internal bladder. The microcontrollers are electrically wired to a 5V power source being an electronic device such as a computer. The electronic device has a graphic user interface configured for a programmer to calibrate the gas sensors, to define threshold values, and to collect data pertaining to the detected gas signature.

It would be desirable for a gas analysis system to indicate to a user when concentrations within an exhaled breath fall within a suitable range considered to be a breath pattern signature of COVID-19, whereby, elevated concentrations of CO and acetone combined with the lowered concentration of alcohol are detected in COVID-19 breath samples and are not characteristic of non-COVID-19 breath samples. In order to accomplish incorporating a light emitting unit indicator to the current electronic nose system to accurately activate in response to both the CO and alcohol concentrations detected within a sample, a first gas sensor having a high sensitivity to CO and a second gas sensor having a high sensitivity to alcohol would need to be provided. Figure 3.4 illustrates the electronic nose testbed prototype housing having LEDs illuminating in response to predetermined threshold levels of target gas concentration in ppm. For example, CO emitted from a non-COVID-19 breath sample has a concentration range of approximately 2 ppm – 100 ppm, corresponding to a “healthy” signature [126]. When a first gas sensor, having a high sensitivity to CO, detects a concentration value of CO emitted from the simulated breath sample solution having a value over 100 ppm, the red colored light emitting diode (LED) of the breath chamber housing of the electronic nose will illuminate to indicate a potential inflammatory response symptom of COVID-19.

In another example, referring again to Table 3.1, it is shown that alcohol is emitted from a non-COVID-19 breath sample having a concentration range between 0.4 ppm – 2.0 ppm, corresponding to a “healthy” signature [142]. When a second gas sensor, having a high sensitivity to alcohol, detects a concentration value of alcohol emitted from the simulated breath sample solution having a value less than 0.4 ppm, the green LED of the breath chamber housing of the electronic nose will illuminate to indicate a potential inflammatory response symptom of COVID-



Figure 3.4 The electronic nose testbed prototype housing has LEDs illuminating in response to predetermined threshold levels of target gas concentration in ppm.

19. Since the sensitivity characteristics of the MQ-2 sensor have a broad detection range for alcohol, this sensor was calibrated to increase sensitivity by rotating the potentiometer clockwise.

In yet another example, the MQ-135 sensor of Table 3.1 is configured to detect a concentration of acetone. Acetone emitted from a non-COVID-19 breath sample has a concentration range between 0.24 ppm – 1.69 ppm, corresponding to a “healthy” signature. When the MQ-135 sensor detects a concentration value of acetone emitted from the simulated breath sample solution having a value over 2.0 ppm, the yellow LED will illuminate to indicate a potential inflammatory response symptom of COVID-19. It would be more desirable if the target gas concentrations in the sample of exhaled breath exceeds threshold values of at least 2 gas sensors, as this may be a strong indication of presence of an inflammatory response associated with COVID-19.

3.1.2.1 System Architecture

The Arduino Uno comprises a board and a chip being the microcontroller. The Arduino Uno has many connectors configured to be electrically connected to the sensor array. Further, the board portion has six Analog to Digital Conversion (ADC) channels which are capable for analog voltage inputs. The Arduino Uno ADC has a 10 bits maximum resolution for the collection of input voltages between values of 0 volts and 5 volts in the form of integer values ranging from 1 to 1024. The gas sensors in the sensor array of the electronic nose device include a commercially available MQ2 and MQ-135 gas sensor. This MOS based gas sensor is categorized as a chemiresistor because its functionality is dictated by a resistance shift between the target gas and the Tin (IV) oxide of the sensor.

The MQ gas sensor is depicted in Figure 3.4 and is comprised of a housing having two stainless steel mesh layers referred to as an anti-explosion network, covering the sensor. The anti-explosion network is connected to a clamping ring. An internal heater begins to heat up when 5V is applied. The MQ sensors require preheating for 24-48 hours prior to data acquisition. The anti-explosion network forms a barrier surrounding the heating element to retain any explosion byproducts if the gas sensor is damaged and to prevent contaminants other than gas from entering the chamber of the sensing element. The sensing element comprises an aluminum oxide-based ceramic having a layer of gas sensitive tin dioxide and is supported by 6 legs as best shown in Figure 3.4. Referring to Figures 3.5 and 3.6, the MQ sensor side has two of the 6 legs labeled H and is configured to heat the sensing element connected by a nickel-chromium coil. Platinum wires of the 4 remaining legs, labeled A and B, are connected to the sensing element and are configured to convey output responses of current changes occurring through the sensing element. Referring

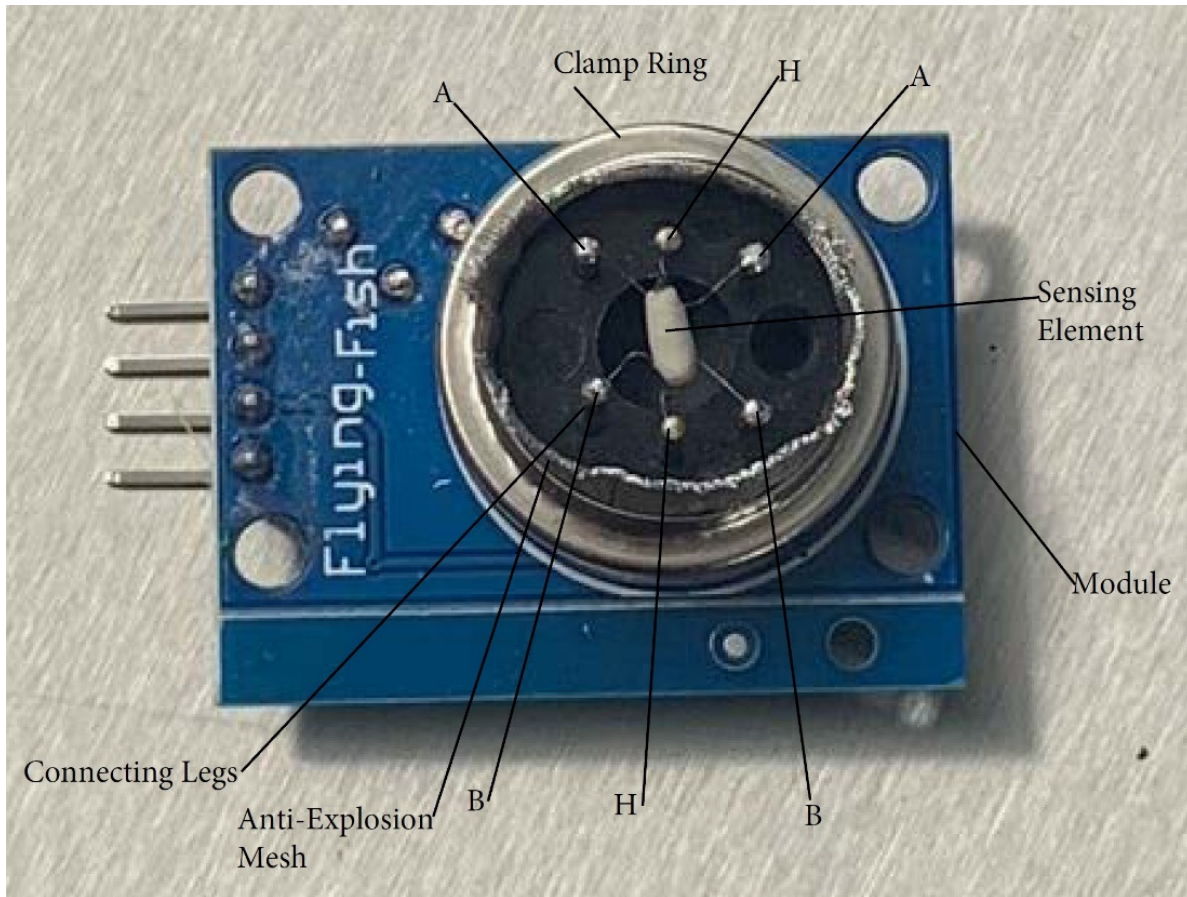


Figure 3.5 The MQ sensor side comprising 6 legs, wherein, two of the legs are labeled H and are configured to heat the sensing element connected by a nickel-chromium coil and platinum wires of the 4 remaining legs, labeled A and B, are connected to the sensing element and are configured to convey output responses of current changes occurring through the sensing element.

to Figure 3.6, the MQ module component side has four pins being common collector voltage (VCC), Ground (GND), Digital (DO), and analog (A0), a power LED that illuminates when connected to a 5V power source, and a digital output (DOOUT) LED that is configured to illuminate when a gas is detected.

3.1.2.2 Gas Sensor Signal Conditioning and Interfacing

The MQ2 and MQ135 sensors are not capable of connecting directly with a breadboard, so the MQ sensors are coupled to a module interfaced with the Arduino Uno microcontroller. Referring again to Figure 3.5, the VCC pin supplies the module with power when it is connected

to the 5V output of the Arduino Uno microcontroller. The GND pin is connected the GND pin of the Arduino Uno microcontroller. The analog output voltage is provided by A0 and is based on the concentration of exposed gas. Figures 3.7 and 3.9 have been designed using Fritzing open-source electronic automation designer software, wherein, the power source is not shown and they illustrate the signal interfacing of the gas sensor unit with the Arduino Uno microcontrollers. In particular, the A0 pin of the MQ2 sensor module is connected to A0 of the Arduino Uno microcontroller and the A0 pin of the MQ-135 sensor module is connected to the A1 of the Arduino

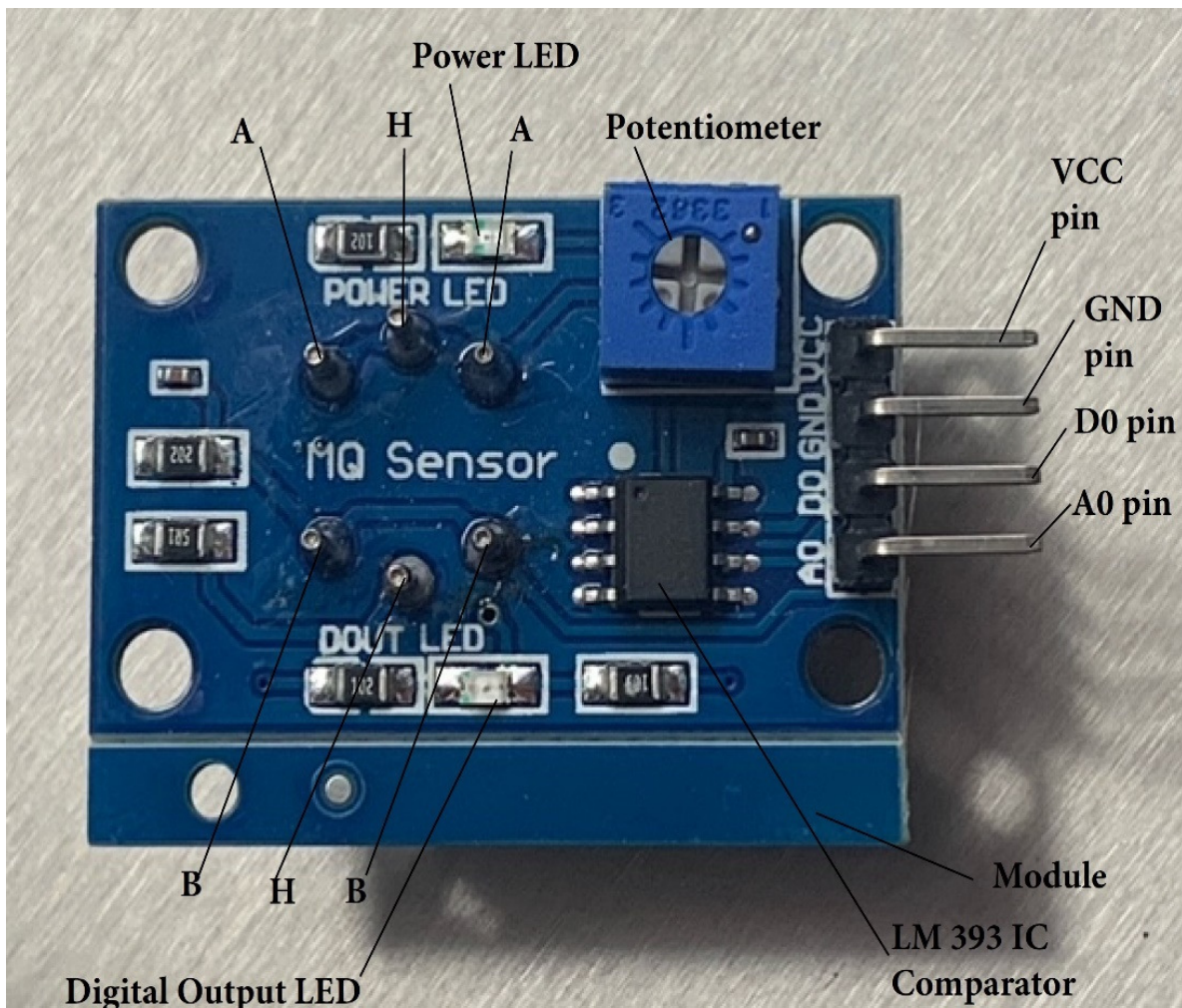


Figure 3.6 The MQ module component side has four pins being Common Collector Voltage (VCC), Ground (GND), Digital (D0), and Analog (A0).

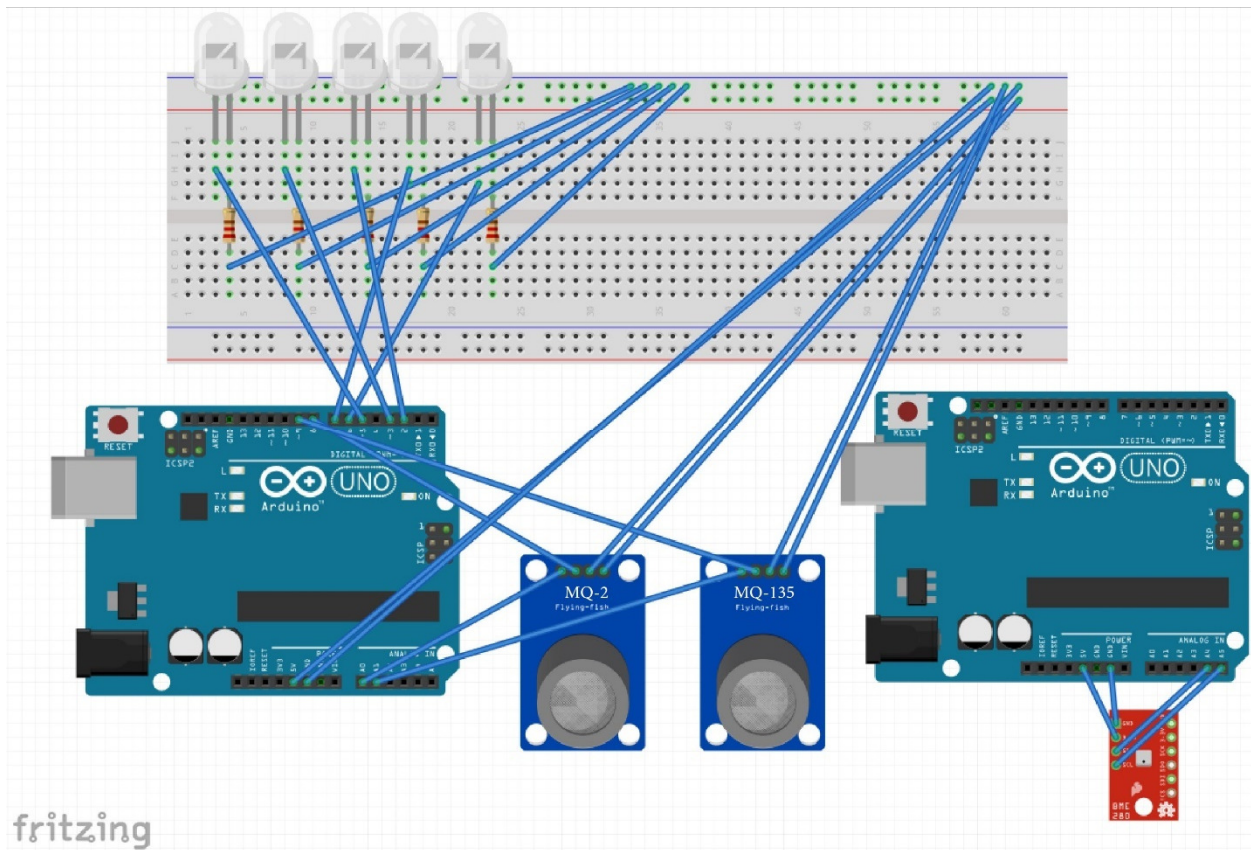


Figure 3.7 A systematic design of the sensor unit having a breadboard in electrical communication with a first and a second Arduino Uno microcontroller, a MQ-2 gas sensor, a MQ-135 gas sensor, a BME280, and 5 LEDs.

Uno microcontroller. The D0 output pin provides a digital representation of detected gas. The D0 output pin of the MQ2 sensor module is connected to Digital pin#8 of the Arduino and the D0 output pin of the MQ-135 sensor module is connected to Digital pin#9 of the Arduino.

Figure 3.7 depicts a systematic design of the sensor unit having a breadboard in electrical communication with a first and second Arduino Uno microcontroller, a MQ-2 gas sensor, a MQ-135 gas sensor, a BME280, and 5 LEDs. In regards to the 5 LEDs shown in Figure 3.4 and Figure 3.8, the cathode is the short leg of each LED and it is connected to ground through a 220-ohm resistor. The anode is the long leg of each LED. The anode of the white led is electrically connected to Digital pin#6 of the Arduino. The anode of the blue led is electrically connected to Digital pin#7

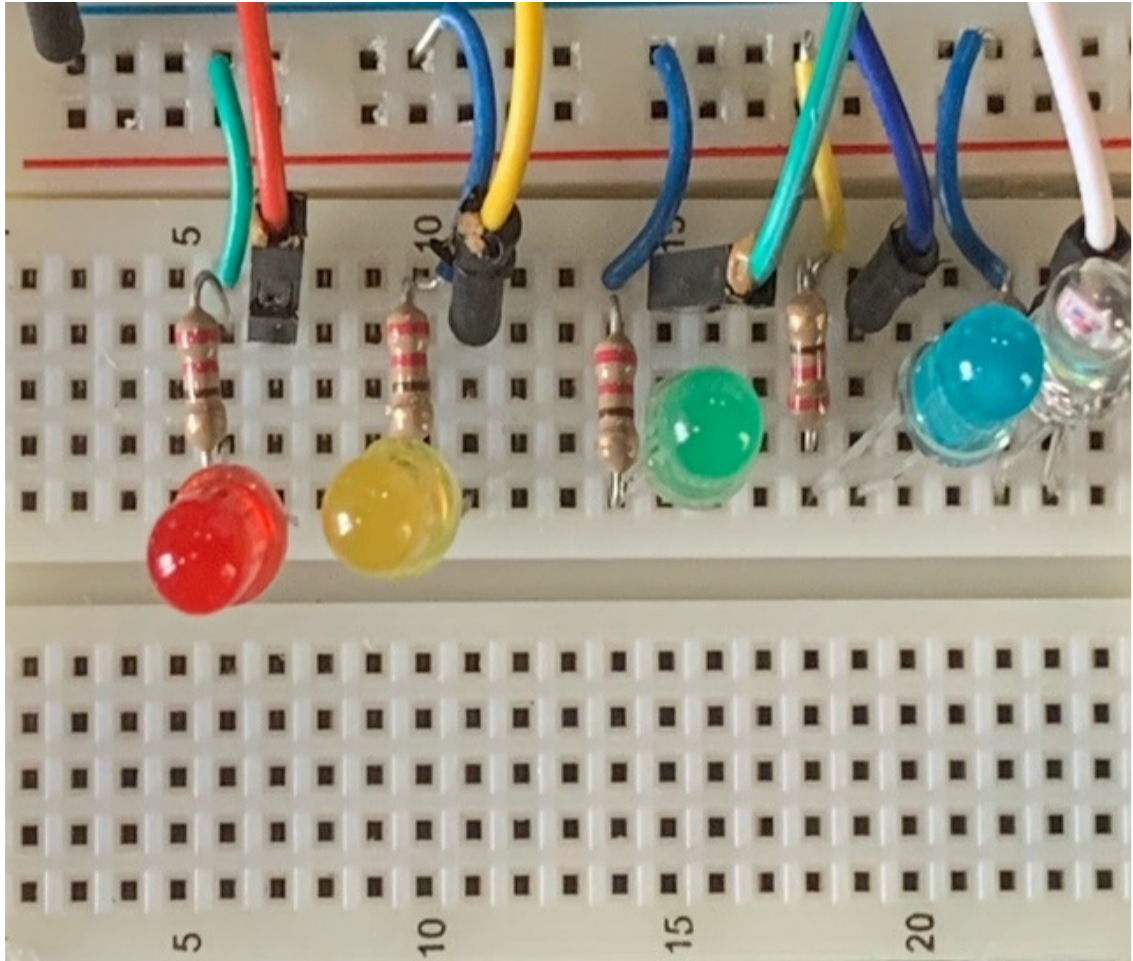


Figure 3.8 Each light emitting diode is individually electrically connected to a 220-ohm resistor on a breadboard.

of the Arduino. The anode of the green led is electrically connected to Digital pin#2 of the Arduino. The anode of the yellow led is electrically connected to Digital pin#3 of the Arduino. The anode of the red led is electrically connected to Digital pin#5 of the Arduino. The source code is attached in Appendix B.

The Bosch BME280 sensor module measures pressure, temperature, and humidity. Referring again to Figures 3.7 and 3.9, the Bosch BME280 module has four pins being a power pin (VIN) connected to 5V of a second Arduino Uno microcontroller, a common ground pin (GND) electrically connected to GND of the second Arduino Uno, a serial clock pin (SCL) for

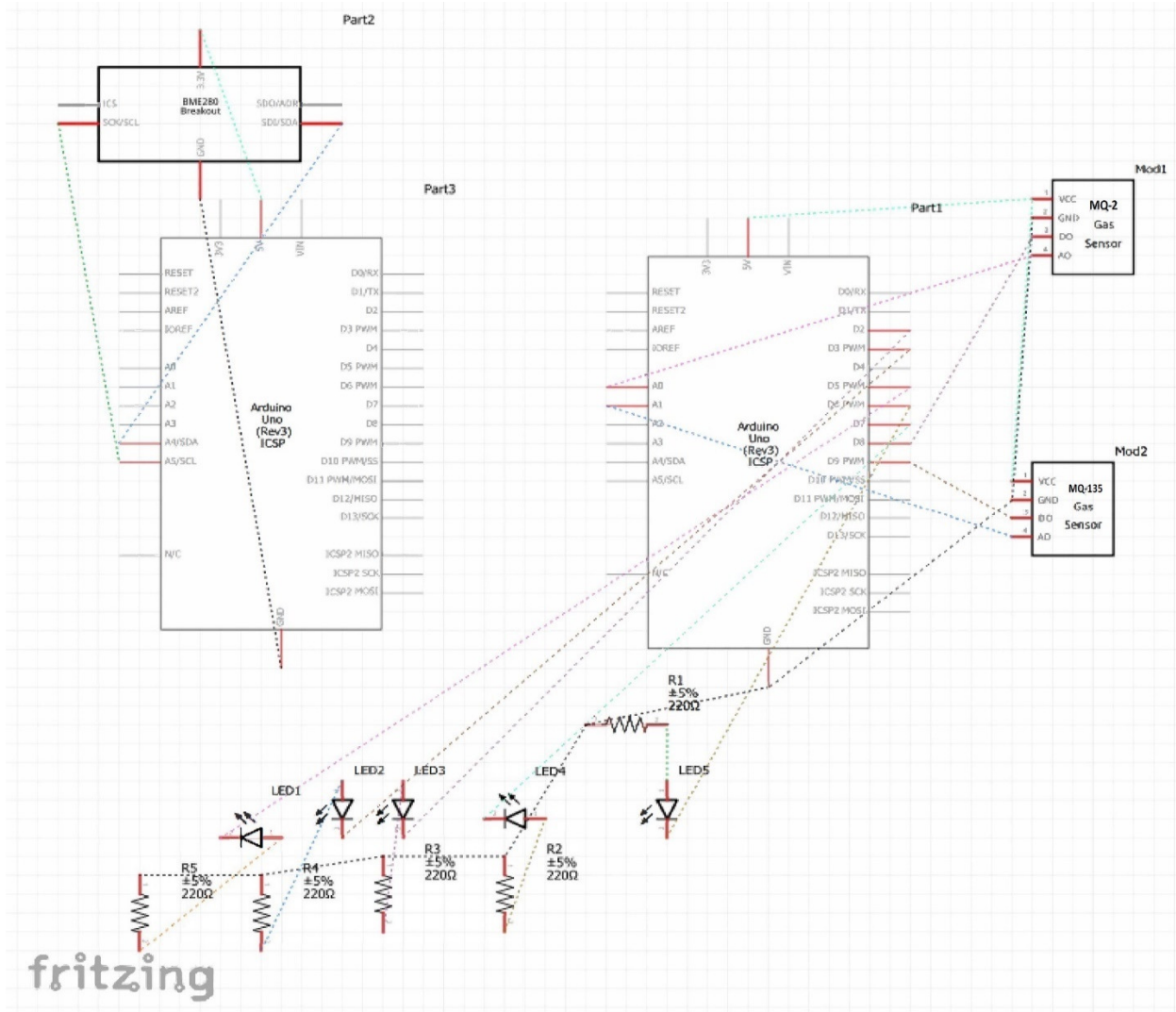


Figure 3.9 A schematic wiring diagram of the sensor unit having a first and a second Arduino Uno microcontroller in electrical communication with a MQ-2 gas sensor, a MQ-135 gas sensor, a BME280, and 5 LEDs.

12C interface is connected to A5 of the second Arduino Uno, and the serial data pin (SDA) is for 12C interface and is connected to A4 of the second Arduino. Measurements from the BME280 sensor were obtained using Arduino Uno with the Adafruit_BME280 library attached in Appendix C. The MQ gas sensor is configured to detect VOCs by volume in air in parts-per-million (ppm) by the resistance ratio of the sensor (R_S/R_0). The ratio of the resistance of the sensor when exposed to the target gas (R_S) to the resistance of the sensor when exposed to clean air (R_0). The resistance

ratio (RS/R0) is used to calculate the concentration of detected gas in parts-per-million, whereby, RS is the resistance of the sensor when the sensing element detects a gas and R0 is the sensor resistance in clean air with an absence of target gas. The following equation is used to obtain the R0 value:

$$R0 = \frac{RS}{f}, \quad (1)$$

where f is the fresh air ratio value from the Hanwei Electronics CO., LTD MQ sensor data sheet.

The MQ sensor calibration line is shown as follows:

$$y = mx + b. \quad (2)$$

A log-log scale is applied due to the calibration line being nonlinear and is expressed as the following equation:

$$\log(y) = m * \log(x) + b. \quad (3)$$

where y is the ratio (RS/R0), x is the ppm value, m is the slope of the line, and b is the intersection point. Two points are selected on the MQ sensor calibration line and they are denoted (x₁, y₁) and (x₂, y₂) and the slope is determined using the equation expressed as:

$$m = [\log(y_2) - \log(y_1)] / [\log(x_2) - \log(x_1)]. \quad (4)$$

The intercept of the MQ sensor calibration line is calculated with the following equation:

$$b = \log(y) - m * \log(x). \quad (5)$$

After calculating the slope and intercept values, the concentration of target gas in ppm can be determined using the following equation:

$$x = \frac{10^{[\log(y)-b]}}{m}. \quad (6)$$

The signal conditioning circuit of the MQ-2 and MQ-135 gas sensors is depicted in Figure 3.9 in which the MQ gas sensor has resistor (RL), 5V supply voltage (VC), and the measured

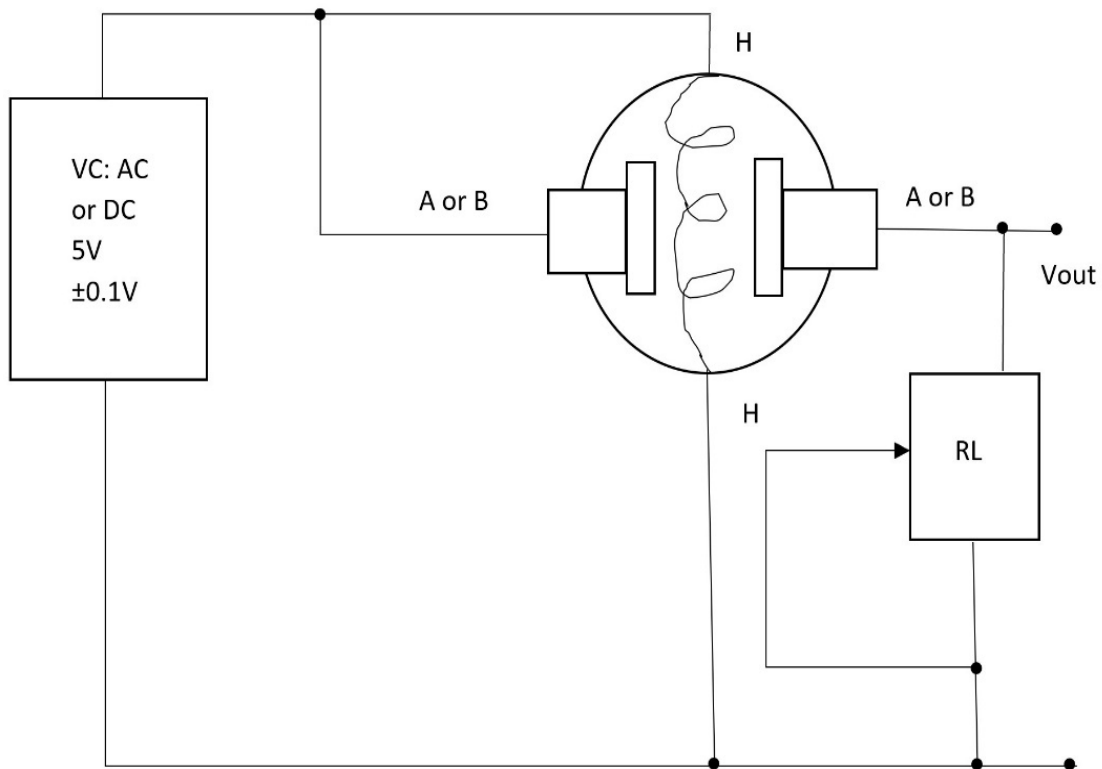


Figure 3.10 Signal conditioning circuit of the MQ gas sensor having resistor (RL), 5V supply voltage (VC), and the measured analog/digital value being the output voltage (Vout).

signal condition resistance to voltage comprising a gas sensor with load resistance , whereby, analog/digital value being the output voltage (Vout). The MQ gas sensors have a resistance change when exposed to a target gas concentration. A voltage divider network is used for the resistance is converted to voltage. The calibration equation of the MQ-2 and MQ-135 gas sensors are based from the schematics of the sensor in Figure 3.10 and Ohm's law and is depicted as follows:

$$R_S = \left(\frac{V_C - R_L}{V_{out}} \right) - R_L, \quad (7)$$

where R_S is the resistance of the sensor when the sensing element detects a gas, R_L is the load resistance at 10K, V_C is the circuit voltage being $5V \pm 0.1$ for the sensors, and V_{out} is the measured

analog/digital value being the output voltage. Attached Appendix B details the Arduino source code for calculating the detected concentrations of target gas in ppm. The calculated values for RL, R0, m, and b are entered into the program.

3.2 Gas Measurement Protocol and Results for Preliminary Gas Data Acquisition

During laboratory tests on the COVID-19 breath simulation mixture formulated during this Dissertation research, two postulated breath analysis strategies were examined to acquire gas data to assess the suitability of using MOS-based gas sensors. This was for the application of exhaled breath analysis to differentiate between potential COVID-19 breath and breath exhaled from a non-COVID-19 individual. First was to acquire gas data as it relates to the concentration values each ranging between 10 ppm-300 ppm of COVID-19 breath simulation mixture and the respective output responses from the gas sensors. In the second strategy, it was to acquire gas data as it relates to the gas sensors being exposed to the COVID-19 breath simulated mixture at differing flow rates ranging between 15 -41.67 mL/min and the respective output responses from the gas sensors. Regression analysis results indicated that both the MQ-2 and the MQ-135 sensors generated an effective response to the COVID-19 breath simulation mixture presented at varying concentrations. However, results from the output response of an MQ-2 and an MQ-135 sensor to a diverse environment of target gasses indicated the MQ-2 gas sensor as taking a greater length of time to normalize baseline drift compared to an MQ-135 gas sensor due to cross interferences with other gasses, which supports the MQ-135 gas sensor as being a potential component of a viable electronic nose for breath analysis applications.

The electronic nose has a housing retaining an array of metal-oxide semiconductor (MOS) gas sensors retained in the chamber of the housing. These sensors are capable of being saturated by a target gas to then produce a voltage drop across the sensors resulting in an output response in

volts (V). The MOS-based sensors are capable of detecting gas concentrations in parts-per-million (ppm) of CO, acetone, and alcohol. Referring again to Figure 3.2, circuitry of the first Arduino Uno microcontroller electrically connects to the MOS-based MQ-2 and MQ-135 gas sensors. The second Arduino Uno microcontroller is electrically connected to a BME280 sensor configured to measure pressure and temperature within the chamber of the housing. The housing chamber retains an internal bladder which connects the input port of the electronic nose to the exhaust port of the electronic nose to separate the microcontrollers and electronic circuitry from the gas obtained from the sample solution, whereby, at least a portion of the BME280, MQ-2 sensor configured to detect both CO and alcohol, and a MQ-135 sensor configured to detect acetone are retained within the internal bladder. The microcontrollers are electrically wired to a 5V power source being an electronic device such as a computer. The electronic device has a graphic user interface configured for a programmer to calibrate the gas sensors, to define threshold values, and to collect data pertaining to the detected gas signature.

The internal bladder of the housing chamber is purged with compressed oxygen, as the carrier gas, to reset the sensors to baseline. A sample solution comprises liquid alcohol and liquid acetone mixed together and retained within an air tight sample vessel to reduce and/or eliminate environmental contaminants. In an attempt to mimic the temperature of exhaled breath, the sample solution of liquid alcohol and liquid acetone were heated to approximately 94°F within the known range of 87.8°F-95°F for exhaled breath temperature [141]. Again, Figure 3.2 illustrates the orientation of the compressed oxygen vessel being in communication with the flow meter, the sample vessel retaining the simulated breath sample liquid solution, and the internal bladder of the electronic nose housing. The gasses emitted from the simulated breath sample liquid solution being retained within the sample vessel are carried by compressed oxygen to mix with 150 ppm of

compressed CO calibration gas. The compressed CO gas is emitted from a controlled high pressure aluminum cylinder in communication with the sample vessel retaining the gasses emitted from the liquid alcohol and the liquid acetone solution. These gasses are then pumped into the internal bladder through a one-way valve of the inlet port. The t-handle of the ball valve of the exhaust port is oriented in a closed position to ensure the sample is retained in the internal bladder long enough to saturate the gas sensors.

The alcohol, CO, and acetone gasses mimic the mixture of gasses present in an exhaled breath and are carried with the compressed oxygen carrier gas past a single MOS-based MQ-2 sensor configured to detect both CO and alcohol, a single MOS-based MQ-135 sensor configured to detect acetone, and a BME280 sensor configured to detect temperature having a BMP280 piezo-resistive pressure sensor. The flow control of the model A-5 In-Line Dual Scale Flowmeter is configured for a user to visually monitor the volume of oxygen flow via a round ball within the tapered tube of the flowmeter. The gas flows to the sensors which are mounted on an inner wall surface of the internal bladder near the inlet port of the electronic nose and the gas is then exhausted through the exhaust port of the electronic nose when the t-handle of the ball valve is oriented in an open position. After the gasses emitted from the simulated breath sample solution saturate the sensors within the internal bladder of the electronic nose, the analog signal from the MQ-2 and MQ-135 sensors are transmitted to a LM393 High Precision Comparator configured to digitize the signal. The comparator determines when the threshold values set by the potentiometer of the sensors have been met. The sensors of the electronic nose interface with a microcontroller Arduino Uno and the sensor values of CO, alcohol, acetone concentrations are displayed on a serial monitor within approximately 27 seconds from the initial sample introduction. The Arduino Uno code converts the digital signal from output response (V) into concentration (ppm) based on the

resistance ratio (R_S/R_0) of the resistance change when the sensor is exposed to a target gas (R_S) in relation to the stable sensor resistance of the sensor in clean air (R_0). Thus, a detected target gas of a sample may be detected and measured to indicate the approximate concentration in ppm.

3.2.1 Flow Rate Impact

Figure 3.11(a) shows the measured temperature detected from the BME280 temperature sensor and the baseline drift of the MQ-2 and MQ-135 sensors retained within the internal bladder of the electronic nose at the ambient working condition of temperature being approximately 66°F and having approximately 61% humidity after preheating for 24 hours. The baseline of the sensors output for both the MQ-2 and MQ-135 sensor maintains a stable state at ambient working conditions for concentrations of CO, alcohol, and acetone. The flow rate of the carrier gas is regulated to dispense oxygen using the flow control of the flowmeter which may be rotated to adjust the flow of the carrier gas. Figure 3.11(b) illustrates the resulting output responses of the MQ-2 sensor as the sensor is exposed to gasses emitted from 300 ppm of the sample solution at different flow rates. Figure 3.11(c) illustrates the resulting output responses of the MQ-135 sensor as the sensor is exposed to gasses emitted from 300 ppm of the sample solution at different flow rates. For both the MQ-2 and MQ-125 sensors, as the flow rates increase, the characteristic peaks of alcohol, CO, and acetone, detected from the sample solution, occur more rapidly compared to when the flow rate is reduced.

As the flow rate increases, the positions of the characteristic peaks of alcohol, CO, and acetone congregate in a closer proximity to each other compared to the peaks having a decreased flow rate. The peaks of the target gas have a closer proximity to each other during an increased flow rate result in an increased difficulty to differentiate between each target gas during an

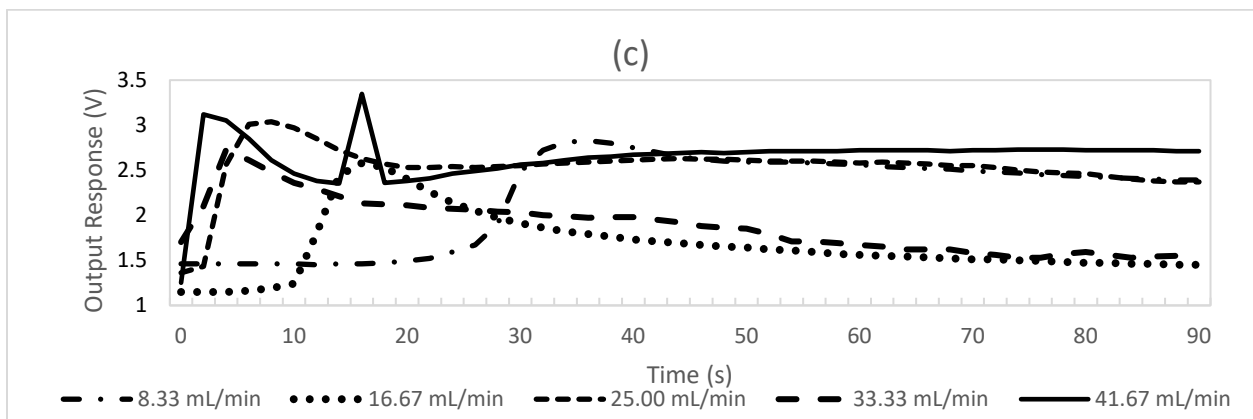
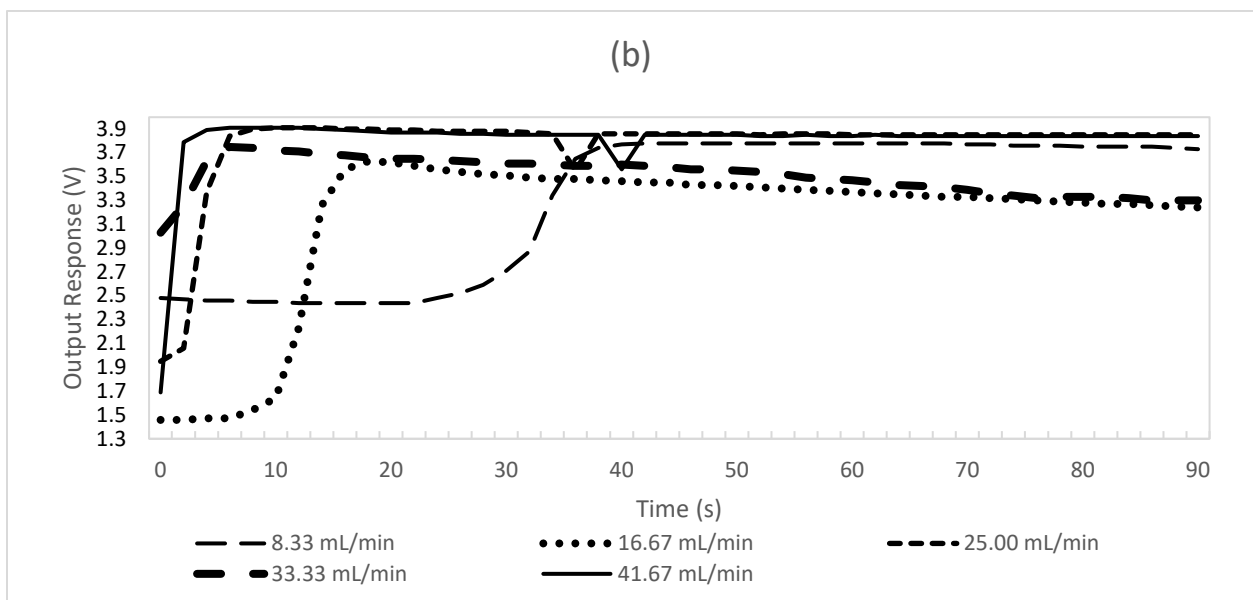
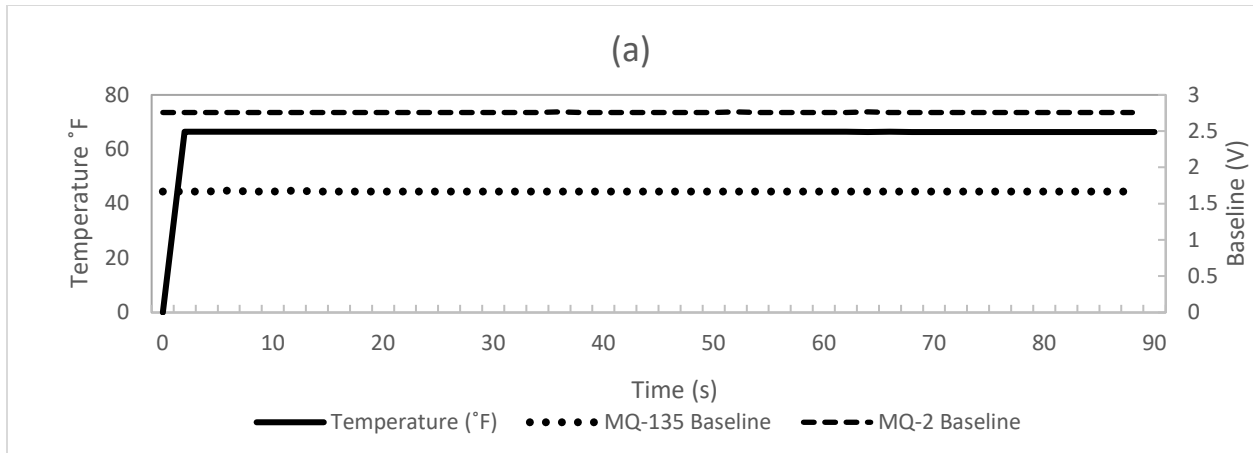


Figure 3.11 (a) Temperature and flow control of baseline drift over the MQ-2 and MQ-135 MOS based sensors, (b) Output responses of the MQ-2 sensor at different flow rates of 300 ppm sample solution, (c) Output responses of the MQ-135 sensor at different flow rates of 300 ppm sample solution [124] © 2021 IEEE.

increased flow rate. However, the detection of these peaks having a decreased flow rate require an increase in detection time for each detection protocol. Thus, it would be more desirable for an electronic nose to have a medium flow rate resulting in a more rapid detection of a target gas with minimal sample time for the sensors to return to baseline. Thus, in light of the measured output response and the detection time, the electronic nose proceeded with the more desirable protocol using the sample solution having a flow rate of the oxygen carrier gas being approximately 25.00 mL/min.

Unlike GC-IMS techniques currently used to separate the plurality of compounds in an exhaled breath sample and then identification of each individual compound based on drift velocity, MOS based MQ gas sensors of this instant study detect a target gas based on a voltage divider network formed by the load resistance and the sensor. The MQ-2 and MQ-135 sensors are coded using Arduino software configured to calculate specific gas concentrations using fresh air calibration data and the resistance ratio provided by the manufacturer's datasheet. In particular, the load resistance slope and intercept of the calibration line follow a linear scale that is converted into a log-log scale, as the MQ sensor data is nonlinear. The Arduino coding program utilized in this study calculates the resistance of the sensor from the analog voltage across the load resistor.

For example, the MQ-2 sensor has sensitivity characteristics for a plurality of gasses including, but not limited to, CO and alcohol, whereby, a single MQ-2 sensor produces an analog output voltage. Thus, a single MQ-2 sensor will not differentiate between a concentration of detected CO and a concentration of detected alcohol with a high accuracy. As a result, it is expected that the accuracy of the sensors will improve if a gas detection system has a first gas sensor having a high sensitivity to CO and a second gas sensor having a high sensitivity to alcohol rather than a single gas sensor having a broad detecting scope encompassing both CO and alcohol. Further, the

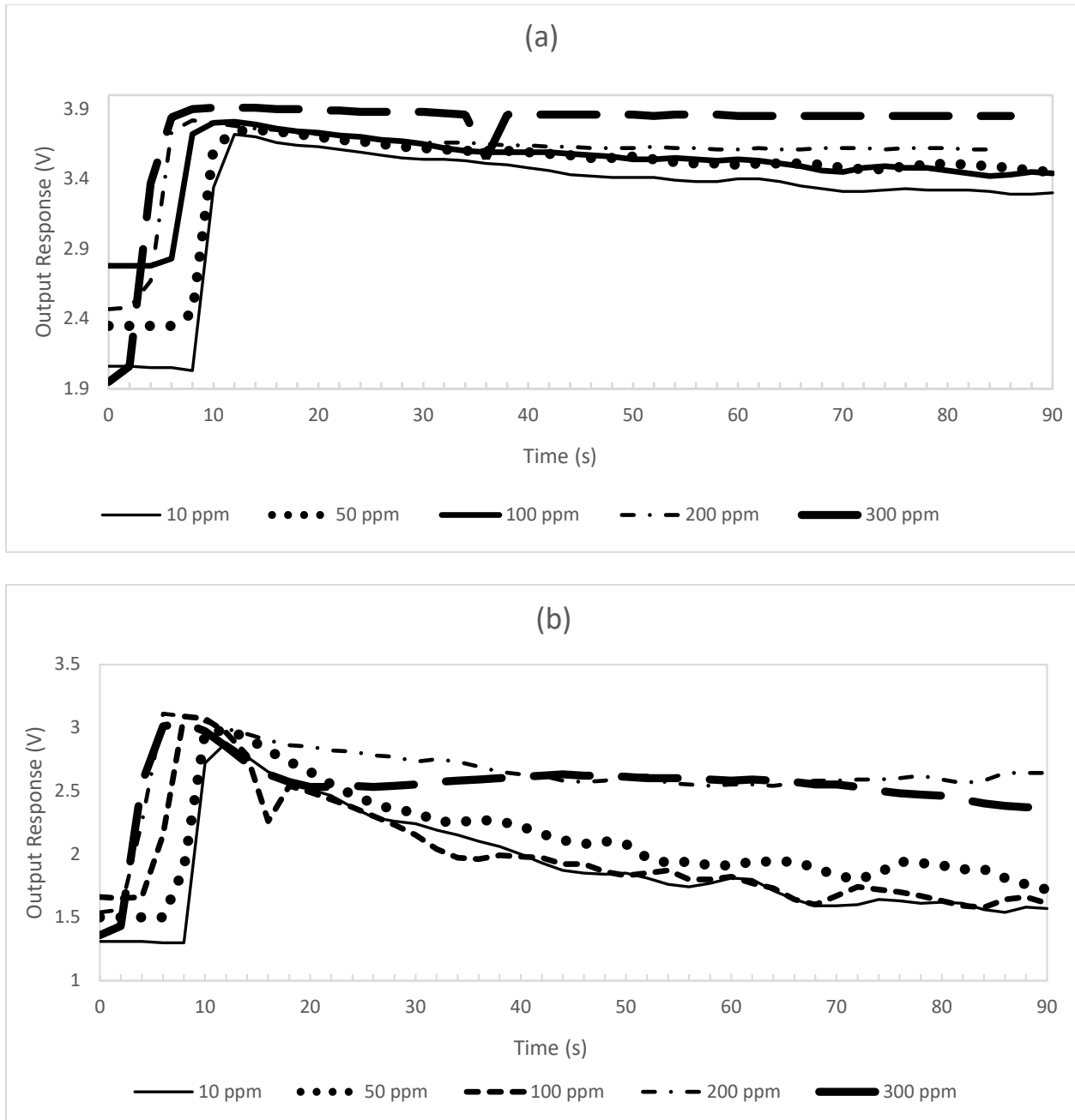


Figure 3.12 Gas concentration gradient of simulated breath sample having a flow rate of 25.00 mL/min (a) for the MQ-2 sensor, (b) for the MQ-135 sensor [124] © 2021 IEEE.

incorporation of an array of sensors that are highly specific to an individual target gas is desirable for our future works in the evolution this current electronic nose system. However, in light of the sensitivity characteristics of the MQ sensors used in Dissertation, the analysis of the unique

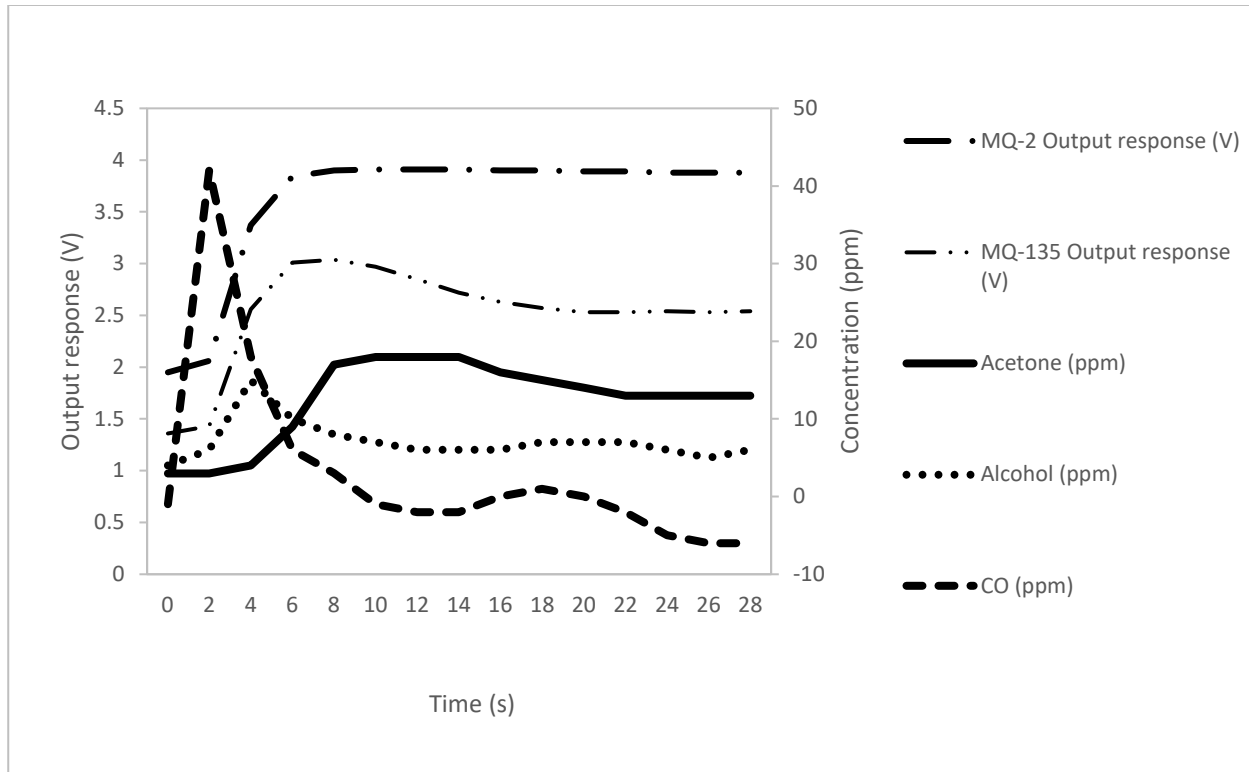


Figure 3.13 Output response voltages from of the MQ-2 sensor and the MQ-135 sensor with associated individual gas concentrations in ppm of acetone, alcohol, and CO from the 300 ppm sample solution at a flow rate of 25.00 mL/min for 30 s [124] © 2021 IEEE.

characteristics of the output response of a single MQ-2 sensor to a diverse environment of target gasses emitted from the COVID-19 simulation solution is explored to determine the suitability of MQ sensors for the application of exhaled breath analysis in COVID-19.

Referring again to Figure 3.11(b) and Figure 3.12(a), the MQ-2 sensor output voltage data starting at 0 s has a baseline drift of approximately 2.8 V, whereby, electrons from the heated tin dioxide semiconductor particles of the sensing element interact with ambient air, ionize the oxygen in the air causing the tin dioxide to adsorb the oxygen and obstruct the electrical current flow through the sensing element of the MQ-2 sensor. At 6 s of exposure to the simulated exhaled breath sample gas, an increase in the measured output voltage occurs at 3.7 V from the MQ-2 sensor. In particular, this voltage increase occurs when the adsorbed oxygen becomes saturated by the CO

and alcohol gas mixture and is cleaved from its communication with the tin dioxide semiconductor particles of the sensor, whereby, facilitating unobstructed current flow through the sensing element and an associated resistance change of an increased output voltage. As shown in Figure 3.13, during this voltage increase, the MQ-135 sensor detected peaks of approximately 18 ppm acetone and the MQ-2 sensor detected peaks of 42 ppm CO and 15 ppm alcohol from the 300 ppm sample solution at a flow rate of 25.00 mL/min for 30 s.

Most apparent after 10 s, the output response voltage of the MQ-2 sensor has a gradual decline as the CO and alcohol gas mixture begin to dissipate to a lower concentration level. This gradual decline in output response voltage is facilitated as newly available electrons from the heated tin dioxide semiconductor particles of the sensor ionize the oxygen in the air. The sensor adsorbs the ionized oxygen and obstructs the electrical current flow through the sensing element of the MQ-2 sensor until the baseline drift of approximately 2.8 V is achieved. In Figure 3.11(b) and Figure 3.12(a), the output response of the MQ-2 sensor has not declined to meet its baseline drift of approximately 2.8 V even at 90 s. The MQ-135 sensor reaches its approximate baseline drift of 1.8 V, at a faster rate for lower concentrations of 10 ppm and 50 ppm at approximately 50 s as illustrated in Figure 3.11(c) and Figure 3.12(b), however, higher concentrations such as, 300 ppm have not reached baseline drift at 90 seconds after exposure to the COVID-19 simulation solution. This time dependent characteristic is indicative that an MQ-2 sensor with a wide scope of detection for a plurality of gasses within a sample of diverse gasses will take a longer length of time to reach baseline drift compared to an MQ-135 sensor with a higher selectivity for a single gas within a sample of diverse gasses. This process may be expedited by purging the system with compressed oxygen to remove the gasses more quickly from the internal bladder of the electronic nose between sampling intervals. The design of the electronic nose platform has been constructed

to minimize the impact of crosstalk interference of gasses upon the gas sensors. In particular, as a result of the interactions of differing gasses within the simulated sample of exhaled breath and the crosstalk interference that occurs with these gasses at the sensing element of the MQ-2 sensor compared to the MQ-135 sensor, the accuracy of an electronic nose system for the application of exhaled breath analysis would be enhanced by having an array of gas sensors each having a high sensitivity and high selectivity to a single target gas rather than having a wide detection scope of gases.

3.2.2 Gas Concentration Gradient

Figure. 3.12(a) illustrates the output response of the MQ-2 sensor having a concentration of the simulated breath sample solution with ranges between 10 ppm – 300 ppm having a flow rate of 25.00 mL/min. Figure. 3.12(b) illustrates the output response of the MQ-135 sensor having a concentration of the simulated breath sample solution with ranges between 10 ppm-300 ppm having a flow rate of 25.00 mL/min. The detection range of concentrations of alcohol, acetone, and CO detected in the sample solution of the electronic nose was configured for a detection range of approximately 10 ppm-300 ppm according to the standard operating conditions of the sensors. As the flow rate increases, the detection time of both the MQ-2 and MQ-135 sensors decrease which is more desirable for rapid detection of target gasses. The output response of the MQ-2 sensor demonstrates an elevated output response as a result of an increased flow for all tested concentrations of sample solution between 10 ppm – 300 ppm. The output response of the MQ-135 sensor demonstrates an elevated output response as a result of an increased flow for tested concentrations of sample solution between 10 ppm – 200 ppm. The signal accuracy of the of the MQ-135 sensor may be compromised from noise as the sample solution exceeds 200 ppm. The

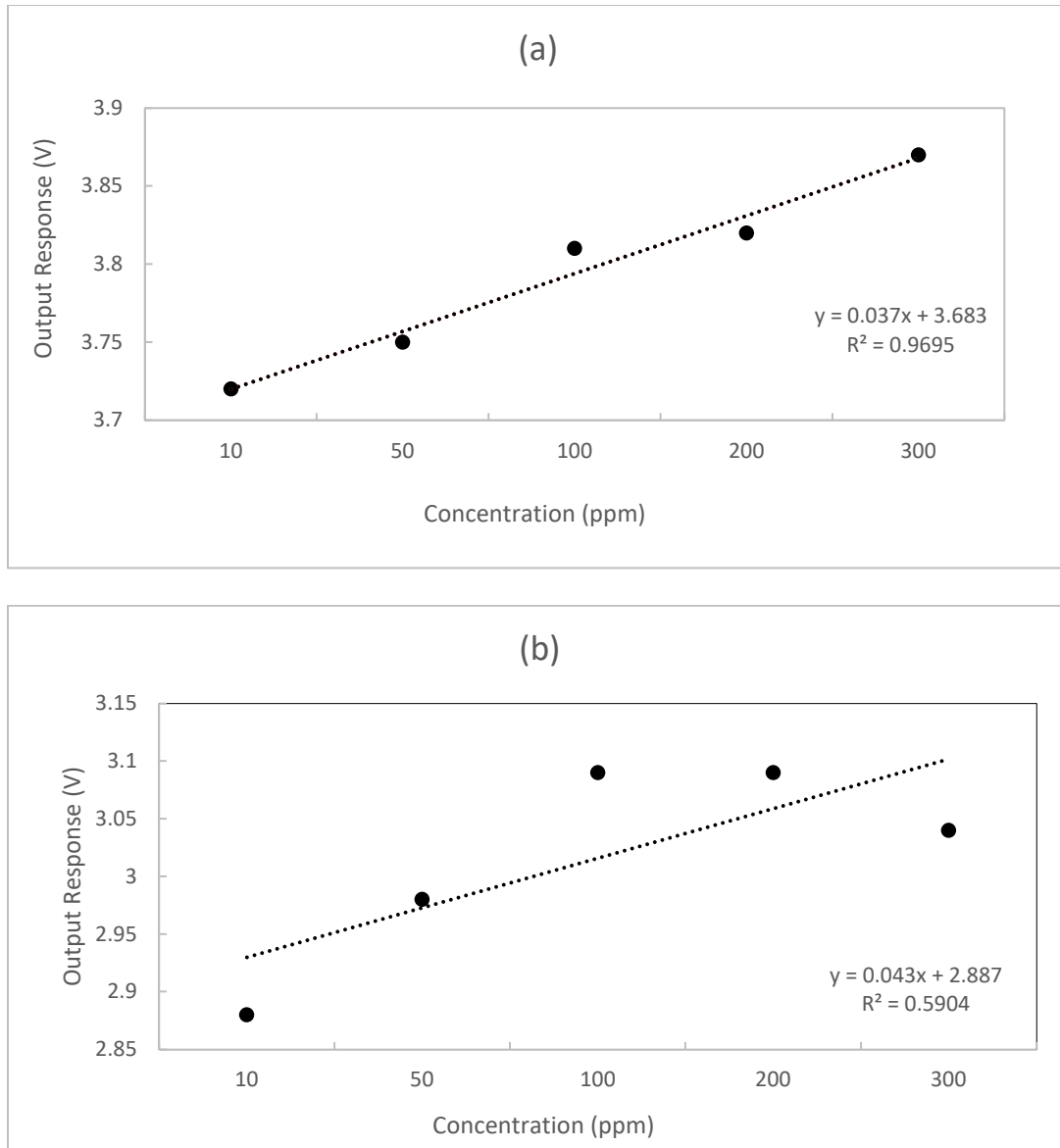


Figure 3.14 Correlation analysis of the concentration gradient between output response (V) versus the concentration (ppm) of COVID-19 simulation solution, (a) for the MQ-2 sensor, (b) for the MQ-135 sensor.

concentrations in ppm of alcohol, CO, and acetone are calculated after the output of the MQ-2 and MQ-135 sensors are converted by the code of the Arduino Uno microcontroller.

Regression analysis was performed to determine the linear model data between output response (V) versus the concentration (ppm) of COVID-19 simulation solution as illustrated in Figure 3.14(a) for the MQ-2 sensor and in Figure 3.14(b) for the MQ-135 sensor. Figures 3.14(a)

and (b) illustrate the horizontal x-axis representing an independent variable being the concentration (ppm) of COVID-19 simulation solution as there was a change in concentration during the experiment, the output response (V) was measured. Figure 3.14(a) best indicates the value of the output response increases as the concentration of COVID-19 breath simulation solution increases, resulting in the gradient of the graph being positive. In particular, the correlation between the values of the output response measurements and the concentration gradient of the sample solution have been determined and the fitting formula of Figure 3.14(a) has a measured relativity (R^2) showing the linear regression model fits the data set of the MQ-2 sensor with a $R^2 > 0.9695$. Thus, 96.95% of the variation in the output responses of the MQ-2 sensor results from the changes in concentration values of sample solution. Figure 3.14(b) depicts the fitting formula having measured relativity (R^2) indicating the linear regression model fits the data set of the MQ-135 sensor with a $R^2 > 0.5904$. 59.04% of the variation in the output responses of the MQ-135 sensor results from the concentration values of sample solution.

As illustrated in the comparison of Figure 3.14(a) with 3.14(b), there is a substantial difference in the R^2 value of the MQ-2 sensor and the MQ-135 sensor indicating that the MQ-135 sensor may need to incorporate a method of signal correction to perform signal conditioning, digital signal processing, and pattern recognition to filter out the noise in an attempt to increase accuracy and efficiency of these sensors. In particular, section 3.3 and Chapter 4 of this Dissertation will discuss a signal processing approach involving the manipulation of the gas sensor output response baseline in light of orthogonal signal correction in an attempt to decrease the negative influence of gradual drifts associated with the output response of the MQ-2 and MQ-135 sensors.

3.3 Gas Measurement Protocol and Results for OSC in a Stability Regression Model

Gas data was acquired by the test bed prototype on a variety of COVID-19 breath simulation solution concentrations. Each measurement included the step of an MQ-2 and an MQ-135 gas sensor being exposed to the COVID-19 breath simulation solution of acetone, CO, and methyl alcohol. The next step included purging the flow lines and internal bladder with compressed oxygen to reset the sensors to baseline. In particular, the MQ-2 and MQ-135 sensors are exposed to the COVID-19 breath simulation solution of acetone, CO, and methyl alcohol within the internal bladder for 90 seconds to adequately quantify the output response of the sensors. Next, the lines of the test bed prototype were purged, to clear away any gasses remaining within the lines and on the sensors, with compressed oxygen for 310 seconds to provide sufficient time for the sensors to return to their baseline drift. For example, the output response generated by the MQ-2 and MQ-135 sensors during a sample cycle prior to the gas sensors being exposed to the COVID-19 breath simulation solution of acetone, CO, and methyl alcohol is illustrated in Figure 3.15(a).

Figures 3.15(a) and 3.15(b) illustrate increased peaks in output response values when the sensors become saturated with the COVID-19 breath simulation solution of acetone, CO, and methyl alcohol during the initial 90 seconds. After 90 seconds of the sample cycle, a decline is shown in measured output response at the time of purging the flow lines and internal bladder of the test bed prototype with compressed oxygen for 310 seconds to reset the sensors to their respective baseline values. The flow rate of the carrier gas is regulated to dispense oxygen using the flow control of the flowmeter which may be rotated to adjust the flow of the carrier gas. Figure 3.15(a) indicates the resulting output responses of the MQ-2 sensor as the sensor is exposed to gasses emitted from 300 ppm of the sample solution at different flow rates ranging between 8.33-41.67 mL/min. Fig. 3.15(b) illustrates the resulting output responses of the MQ-135 sensor as the

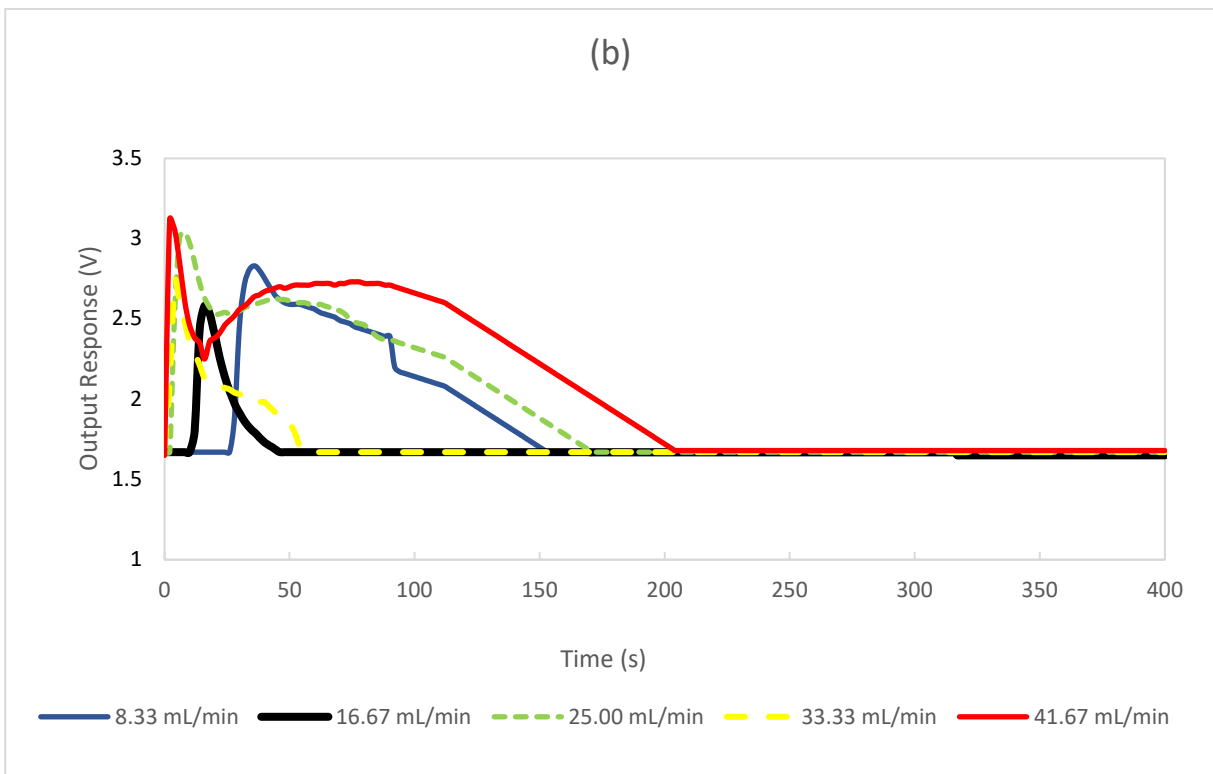
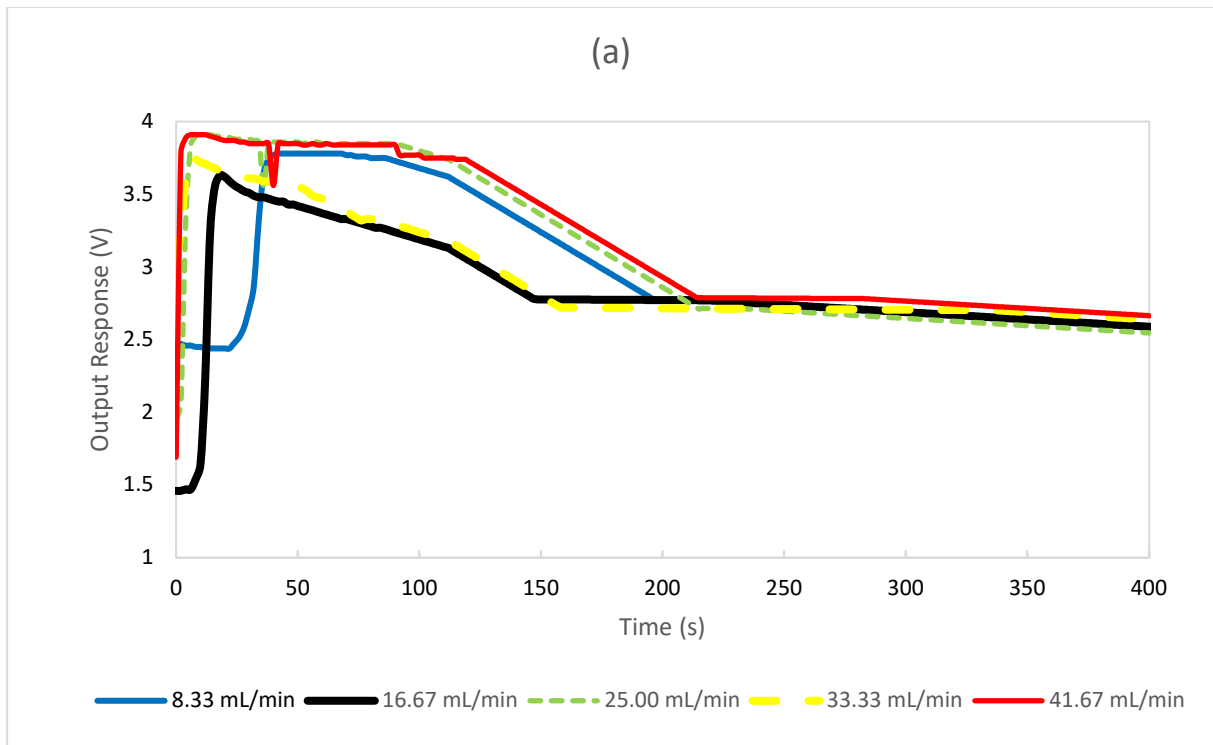


Figure 3.15 (a) Output responses of the MQ-2 sensor at different flow rates of 300 ppm sample solution, (b) Output responses of the MQ-135 sensor at different flow rates of 300 ppm sample solution.

sensor is exposed to gasses emitted from 300 ppm of the sample solution at different flow rates ranging between 8.33-41.67 mL/min. For both the MQ-2 and MQ-135 sensors, as the flow rates increase, the characteristic peaks of alcohol, CO, and acetone, detected from the sample solution occur more rapidly compared to when the flow rate is reduced.

As the flow rate increases, the positions of the characteristic peaks of alcohol, CO, and acetone congregate in a closer proximity to each other compared to the peaks having a decreased flow rate. The peaks of the target gas have a closer proximity to each other during an increased flow rate resulting in an increased difficulty to differentiate between each target gas during an increased flow rate. However, the detection of these peaks having a decreased flow rate require an increase in detection time for each detection protocol. Thus, it would be more desirable for an electronic nose to have a medium flow rate resulting in a more rapid detection of a target gas with minimal sample time for the sensors to return to baseline. Furthermore, in light of the measured output response and the detection time, the electronic nose proceeded with the more desirable protocol using the sample solution having a flow rate of the oxygen carrier gas being approximately 25.00 mL/min.

Five varying concentrations including 10 ppm, 50 ppm, 100 ppm, 200 ppm, and 300 ppm of COVID-19 breath simulation solution of acetone, CO, and methyl alcohol were formulated for the learning measurements. The MQ-2 and MQ-135 sensors were configured with an Arduino Uno microcontroller to digitize the sensor output responses every second. The output responses were recorded to CoolTerm serial port terminal software and transferred to Microsoft Excel Spreadsheet Software. This Dissertation focuses on MQ-2 and MQ-135 gas sensor responses in terms of sensor resistance, as this parameter is provided for in the specification sheet of the MQ-2 and MQ-135 gas sensors in terms of the resistance ratio of the sensor in clean air to the resistance of the sensor

when exposed to a target gas. Ten measurements have been taken for each of the five concentrations of COVID-19 breath simulation solutions that were chosen by random during the experimental testing. Each sensor output is represented by 90 signal responses during gas exposure and by 310 signal responses during the purging process to yield a total of 400 signal response that were detected, filtered, and recorded for each sensor output. The acquired gas data was organized on an Excel dataset having 800 columns {400 data * 2 sensors} and 50 rows {10 measurements * 5 concentrations}.

3.3.1 Measurement Instability

Figures 3.16(a) and 3.16(b) depict the temporal response instability from output response signals of the MQ-2 and MQ-135 sensors. These aggregated individual observations respond to concentrations of 10 ppm, 50 ppm, 100 ppm, 200 ppm, and 300 ppm of COVID-19 breath simulation solution having a flow rate of 25.00 mL/min for the MQ-135 sensor illustrated in Figure 3.16(a) and the MQ-2 sensor illustrated in Figure 3.16(b) and have been organized to display output responses on the y-axis. It can be deduced from Figures 3.16(a) and 3.16(b) that a significant difference of sensor responses between the MQ-2 and MQ-135 gas sensors are acquired for the same COVID-19 breath simulation solution concentration under the same sampling conditions.

As a result of an incomplete recovery process, sensor drift contributes to unstable sensor response outputs. Referring now to Figure 3.17, temporal responses of the MQ-2 sensor were collected during ten consecutive measurements of the 5 concentrations of 10 ppm, 50 ppm, 100 ppm, 200 ppm, and 300 ppm of COVID-19 breath simulation solution. The output responses observed at the start of the measurements indicate the base line value is contingent on the value of the gas concentration of the preceding measurement. In Figure 3.17, beginning with a measurement of 100 ppm of COVID-19 breath simulation solution, the baseline of the MQ-2

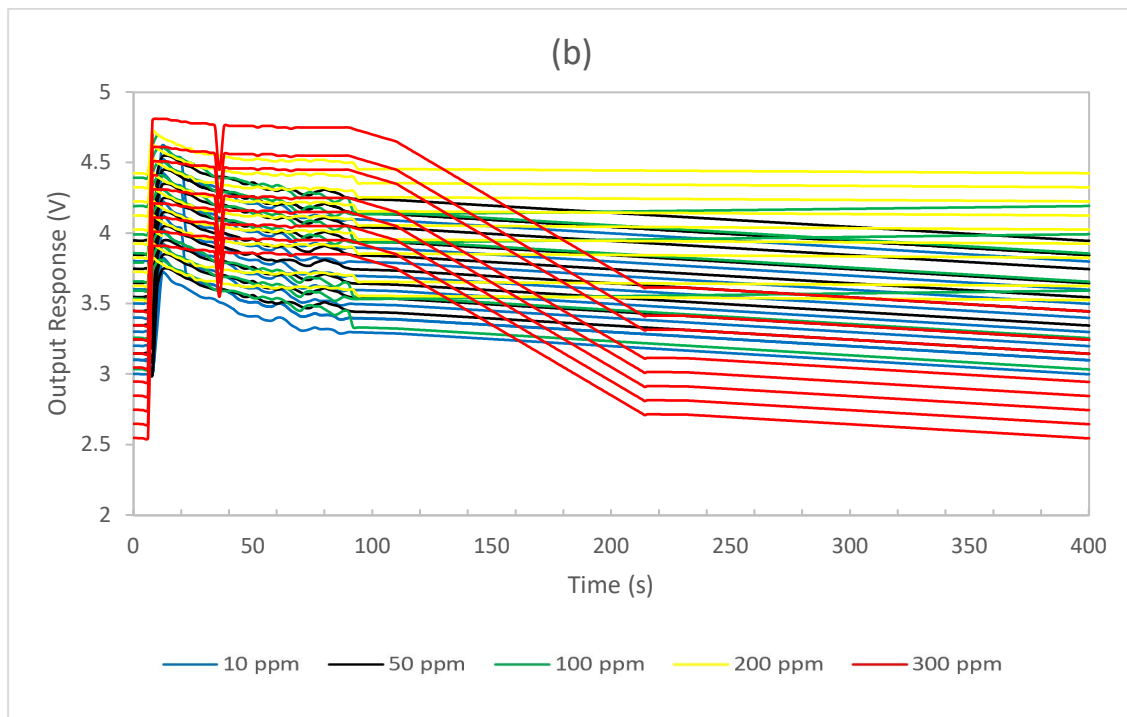
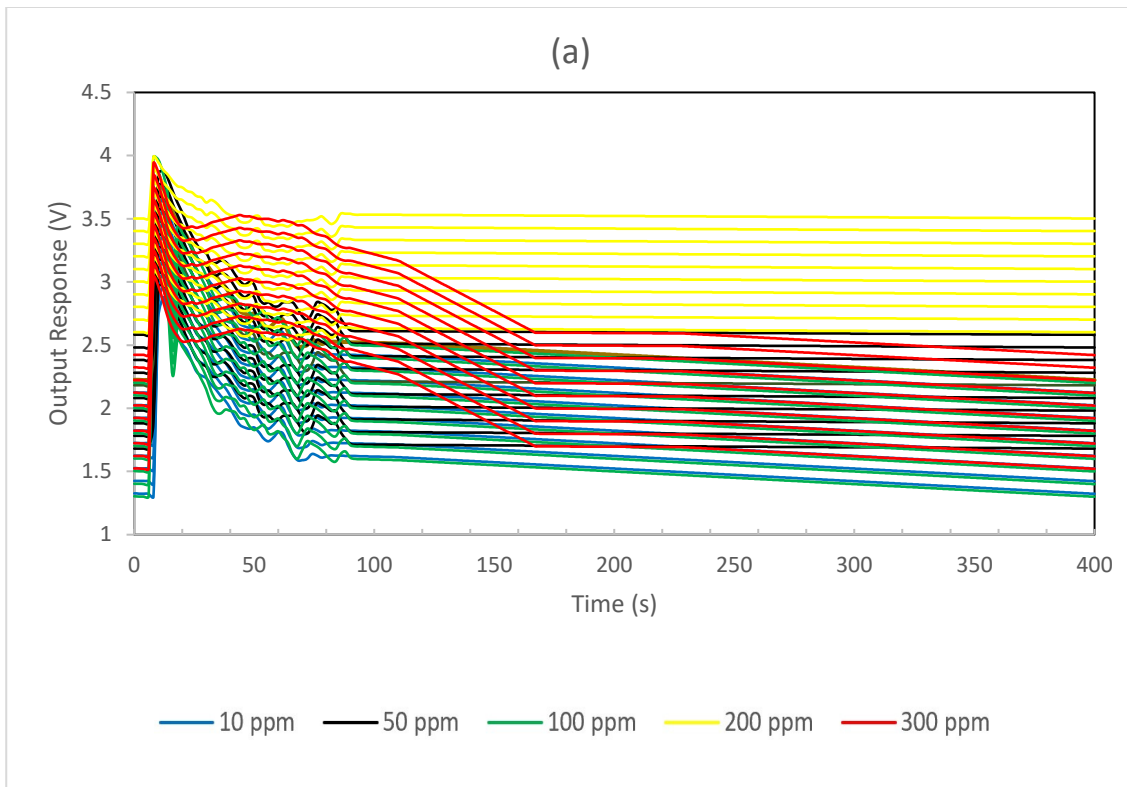


Figure 3.16 Temporal responses at 10 ppm, 50 ppm, 100 ppm, 200 ppm, and 300 ppm of COVID-19 breath simulation solution concentration at 25.00 mL/min (a) for the MQ-135 sensor, (b) for the MQ-2 sensor.

sensor is shown to be 3.148 V when following a measurement of 50 ppm of COVID-19 breath simulation solution and 3.7159 V if the previous measurement had 300 ppm of COVID-19 breath simulation solution. Further, Figure 3.17 emphasizes the drift characteristic of the MQ-2 gas sensor is seen to change both the baseline and the sensitivity of the sensor. This introductory comparison validates the inefficiency of the recovery process of MOS-based gas sensors as a result of pronounced drifts. Thus, it is expected that these drifts will be higher in real-time during the application of using electronic nose technology for breath analysis.

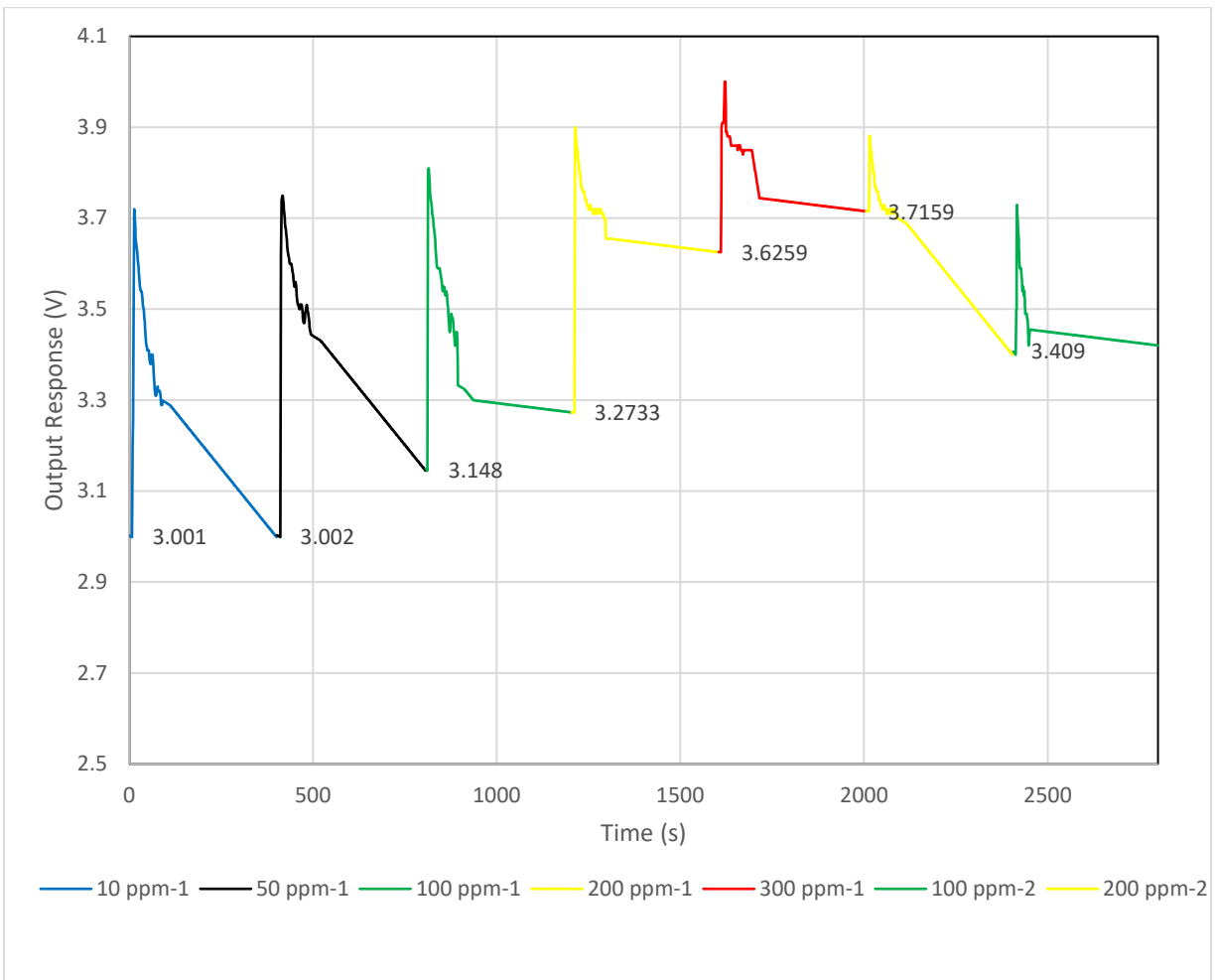


Figure 3.17 Instability of the MQ-2 gas sensor depicted as output responses of initial resistance were collected during a plurality of consecutive measurements of the 5 concentrations of 10 ppm, 50 ppm, 100 ppm, 200 ppm, and 300 ppm of COVID-19 breath simulation solution.

3.4 Reporting Diagnostic Accuracy

The reproducibility, completeness, and transparent reporting of this research was facilitated by the recommendations set forth by the Standards for Reporting Diagnostic Accuracy (STARD) statement [112]. Some of the STARD recommendations are directed to the study design, participants, test methods, analysis, test results. For example, a study design method recommendation includes, but is not limited to, identification as a study of diagnostic accuracy such as sensitivity, specificity, predictive values, or Area Under Curve (AUC) [112]. As it pertains to the diagnostic testing of individuals for SARS-CoV-2, an electronic nose device having gas sensors with a high selectivity to target gasses would be more desirable. Further, the Transparent Reporting of a multivariable prediction model for Individual Prognosis or Diagnosis (TRIPOD) statement sets forth reporting guidelines for the development and validation of prediction models in diagnostic applications [113]. Some of the TRIPOD recommendations are directed to the title, abstract, background and objective, source of data, participants, outcome, predictors, sample size, missing data, statistical analysis methods, risk groups, and development vs. validation. For example, a statistical analysis method recommendation includes, but is not limited to, specify the type of model, all model-building procedures, and methods for internal validation [113]. As it pertains to the diagnostic testing of individuals for SARS-CoV-2, an electronic nose device incorporated with OSC, PLS, and PCA to correct drift variations is most desirable. [154]

Chapter 4: Drift Correction and Calibration

A portion of this chapter was accepted for publication in [154] . Permission to reproduce the works in this Dissertation is included in Appendix A.

The output responses for both the MQ-2 and MQ-135 gas sensors have been compiled in an Excel dataset and are expressed as $G(t)$. A matrix of 50 rows coincide with the observations and 800 columns are associated with the corrected temporal response of the MQ-2 and MQ-135 gas sensors. Concentrations of the differing experiments are arranged in vector Y (50).

4.1 Drift Correction

When gas sensors, such as the MQ-2 and the MQ-135, are exposed to the same gas under the same sampling and environmental conditions, the output responses change and are related to drift. Reducing the variance of this drift can be accomplished with correction methods to improve efficiency and sensor performance [143]. The accuracy of electronic nose devices for applications in breath analysis is influenced by the processing of the sensor output responses to reduce noise and effects of drift as described in Chapter 3. Thus, signal processing of the output responses of the MQ-2 and MQ-135 gas sensors is more desirable to achieve an increased accuracy in electronic nose detection for applications of breath analysis. When gas sensors are exposed to the same gas under the same sampling and environmental conditions, many changes in the sensor response are related to drift. Reducing the variance of this drift can be accomplished with correction methods to improve efficiency and sensor performance [143].

It is assumed that drift can be separated from the analytical signal and modeled. The obtained model can be used for the correction of the sensor array response in new samples [143]. It is also assumed that the sensors of the array have similar correlated behavior in regards to drift, whereby, the drift sensor array has a certain direction associated with all measured samples and with the reference gas [143]. If this assumption is not maintained, the drift correction will be inefficient due to at least a portion of analytical data being eliminated with drift [143]. As a result, drift correction can be utilized by identifying and modeling drift direction of the reference samples and subtracting the obtained value from the new data [143]. Further, the formulation ingredients of equal parts of acetone, alcohol, and CO were assumed to be COVID-19 breath biomarkers as per [98] and were chosen because their corresponding gas sensor was commercially available at the time of the study.

4.1.1 Baseline Manipulation

Studies have described the method of baseline manipulations to overcome the drift effects on output responses of gas sensors in complex atmospheres [116], [117]. Although previous studies have indicated a preference of using the initial output response of a sensor for signal processing techniques, recent studies suggest acquiring measured resistance of the sensor output voltage (G_{final}) at the conclusion of the earlier cleaning step and fractional correction on temporal response $G(t)$ [127], [128] that can be expressed as:

$$G_c(t) = \frac{G(t) - G_{final}}{G_{final}}. \quad (8)$$

The signal processing adjustment is applied to the temporal signals of both the MQ-2 and MQ-135 gas sensors for the quantification of COVID-19 breath simulation solution released in an experimental internal bladder of a testbed prototype of an electronic nose device. A minor improvement is detected in the sensor response differences acquired at the same measurement

conditions and the same gas concentration values; thus, the concentration differentiation is not capable of being realized. After baseline manipulation, the corrected data is organized in dataset (X) and an Orthogonal Signal Correction (OSC) technique is applied to improve the drift correction.

4.1.2 Orthogonal Signal Correction (OSC)

Before regression modeling is used, the baseline manipulation of OSC was performed to decrease the drift effects from the MQ-2 and MQ-135 gas sensor signals and improving the stability and reliability of the calibration process. OSC is configured to eliminate the variance that is not correlated to the variation of concentration (Y) by removing the acquired gas data that is not pertinent to the output response in matrix X , such as the data that is orthogonal or statistically independent to Y , is separated from matrix X . As a result of this separation, the acquired data organized in the matrix will be valuable during calibration of the electronic nose. Studies have described a method of performing an OSC algorithm [127], [128], [143] as described in the following 6 Steps:

1. Decompose X into scores of t using PCA.
2. Make the first score t_1 orthogonal to Y in pursuance of acquiring a regenerated score t_n as depicted below:

$$t_n = (1 - Y(Y^T Y)^{-1} Y^T) t_1 \quad (9)$$

where t_1 is the first vector term associated with the data maximum and where Y^T is the transpose of Y .

3. The weight vectors W are mathematically determined using PLS as shown:

$$W = X^{-1} t_n \quad (10)$$

4. The regenerated score t is calculated as expressed below:

$$t = XW. \quad (11)$$

5. The loading vector P is determined using the following:

$$P^T = \frac{t^T X}{tt_n}. \quad (12)$$

6. Drift correction is represented by regenerated matrix of the new measurements

X_{corr} being established by subtracting the drift component from the new measurement matrix as shown in the below equation [143]:

$$X_{corr} = X - tP^T. \quad (13)$$

In regards to PCA applications, if the sensor responses of the reference sample indicate a substantial drift, the first components in a PCA model may be determined by the use of measurements obtained from the reference sample and indicate the direction of the drift [143]. In particular, the PCA application to drift compensation focuses on the direction of the maximum variance of the output responses of the MOS sensors of the reference samples as a drift [143]. Thus, the loading vector P , of equation 13, obtained from the reference sample contributes to the noise and is utilized to determine regenerated score t of the new measurements X_{corr} . In contrast, PLS modeling for drift compensation utilizes changes in the output response of the gas sensors of the reference samples as a function of time [143]. In particular, PLS modeling may be determined from observing output responses of the gas sensors of the reference samples represented by an X_d matrix and time as the Y matrix. Loading vector P and weights W are utilized to determine the projection of the new measurements in the below equation [143]:

$$t_d = X_n W_d (PW)^{-1}, \quad (14)$$

wherein, t_d represents the projection. The new measurements X_n^{corr} are corrected for drift by removing the drift component using the below equation [143]:

$$X_n^{corr} = X_n - t_d P. \quad (15)$$

Although at least one latent variable could be incorporated into the PCA and PLS model for drift correction, both reference sample and analyzed sample are required to have the same scaling and transformation [143]. It is also known that outliers should be removed from datasets used for the drift model calculations so that the drift direction is not adversely affected. The procedure was implemented to measure the reliability of the OSC method, whereby the regenerated dataset (X_{corr}) consisted of 50 observations and machine learning algorithms are shown to quantify these observations in Microsoft Excel. These 50 observations were separated into an initial set of machine learning training data comprising 75% observations, to serve as a baseline for subsequent analysis, and 25% of the observations being evaluated on a test set. The machine learning algorithm was constructed to contain training and testing data from the 5 concentrations of COVID-19 breath simulation solution.

The previously mentioned Steps 1-6 of the OSC method are performed for the acquired data of the MQ-2 and the MQ-135 gas sensors to result in increasing the resemblance of the output responses of the same respective concentration of COVID-19 breath simulation solution. Figures 4.1 (a) and (b) illustrate the test set of observations following OSC for the 5 concentrations including 10 ppm, 50 ppm, 100 ppm, 200 ppm, and 300 ppm of COVID-19 breath simulation solution. The distribution of temporal responses of corresponding concentrations of COVID-19 breath simulation solution of Figures 4.1 (a) and (b) are shown to be substantially reduced compared to the temporal responses illustrated in Figures 3.16 (a) and (b). As a result of the attenuated temporal responses observed in Figures 4.1 (a) and (b), a distinction can be more clearly recognized between the differing concentrations of COVID-19 breath simulation solution following temporal signal correction using the OSC method. Gas quantification is influenced by OSC as illustrated in Figure 4.2 showing the PCA scores of the acquired data after temporal signal

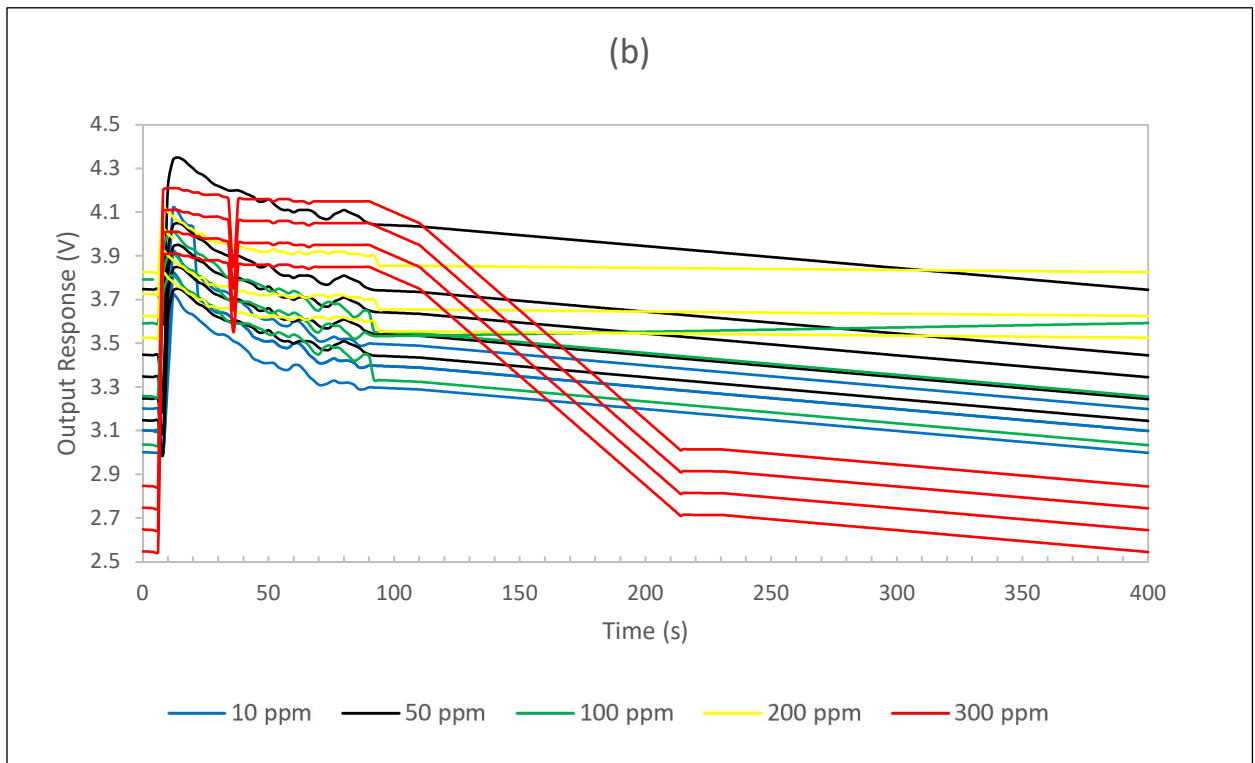
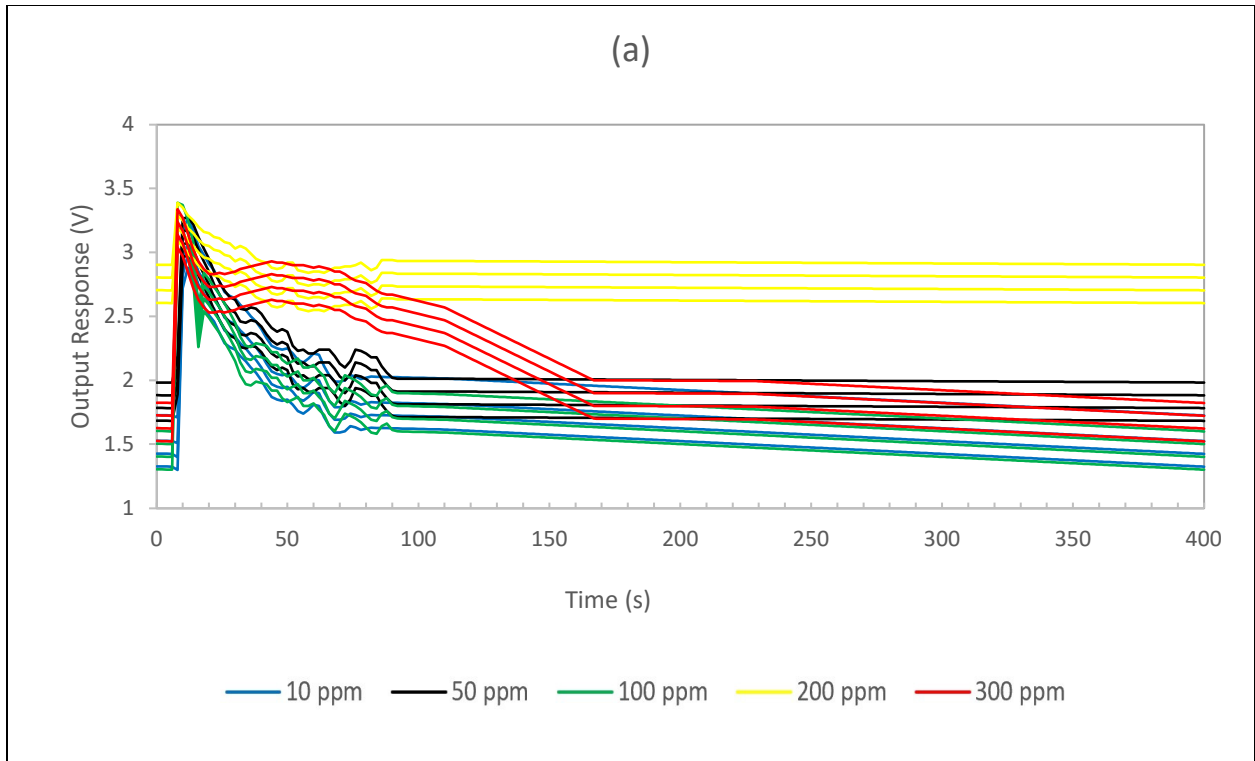


Figure 4.1 Temporal responses of concentrations of 10 ppm, 50 ppm, 100 ppm, 200 ppm, and 300 ppm of COVID-19 breath simulation solution concentration at 25.00 mL/min following OSC for (a) for the MQ-135 sensor, (b) for the MQ-2 sensor.

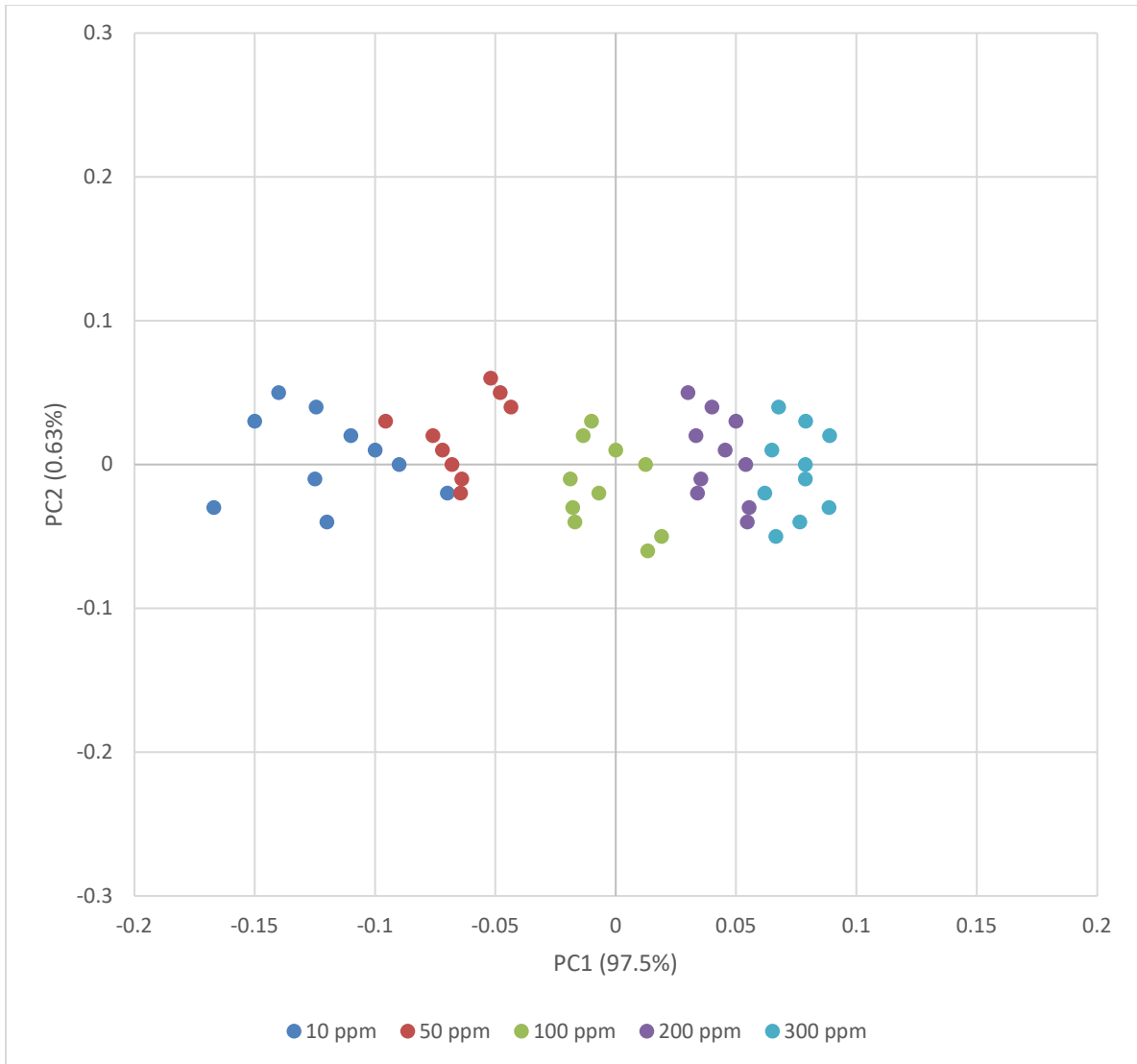


Figure 4.2 PCA plot after OSC correction for concentrations of 10 ppm, 50 ppm, 100 ppm, 200 ppm, and 300 ppm of COVID-19 breath simulation.

correction using the OSC method. In particular, without OSC application, the PCA score plot would demonstrate substantial overlap of concentration points resulting in poor differentiation between concentrations prior to signal processing using the OSC method [127]. As expected, Figure 4.2 illustrates a more desirable dataset plot in which discrimination between concentrations including 10 ppm, 50 ppm, 100 ppm, 200 ppm, and 300 ppm of COVID-19 breath simulation solution points are more observable as a result of OSC.

4.1.3 Calibration

Studies have indicated that due to multicollinearity resulting from highly correlated predictors in the dataset as well as the considerable quantity of the columns of corrected temporal responses of the sensors compared to the rows of observations, it is not appropriate to utilize a multiple linear regression (MLR) [128]. Alternatively, partial least square (PLS) analysis is carried out on independent variables in an attempt to understand the covariance between X and Y . Some studies have indicated that although regression modeling using independent components result in a suitable prediction, overfitting and underfitting is a common problem with regression methods, so it is necessary to optimize the number of components [129]. For example, underfitting a regression model occurs when a small sample is used to estimate a large number of parameters, which results in reduced precision. In another example, overfit data is more complex and less flexible in that it cannot recognize new data because a large number of parameters are used, including noise and outliers.

Calibration of the testbed prototype was achieved with PLS regression, as the dataset was separated into 10 segments with 30 observations each using Analyse-It, a statistical analysis add-in software for Microsoft Excel. Of the 10 segments, two segments served as the data set to assess the functionality of the calibration model while the other 8 segments were utilized as learning data. Cross validation was carried out 10 times in succession to result in each of the 50 observations turning into a predicted observation. Next, the ten root mean square errors (RMSEs) were averaged to determine the RMSE to assess the fit of the regression model with the dataset. Referring now to Figure 4.3, the RMSE data is plotted on the y-axis and the x-axis shows the number of components for raw data with PLS and for OSC corrected data with PLS. Although a high accuracy is achieved with PLS and PLS with OSC, when measuring the error of the model in predicting quantitative

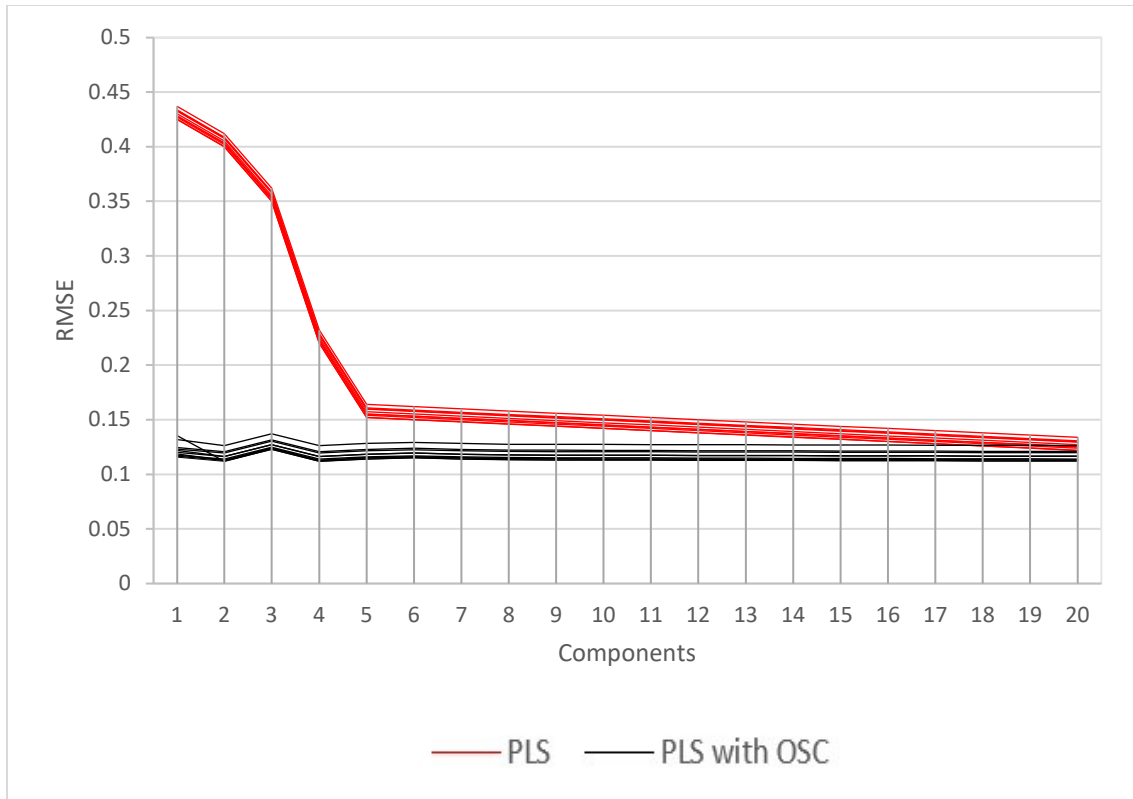


Figure 4.3 Plot illustrating RMSE values on the y-axis and number of PLS and PLS with OSC components on the x-axis.

data, it is more desirable to have a lower RMSE value because the average distance from the predicted values of the model and the dataset values are in closer proximity. The method comprising both PLS with OSC corrected data achieves a RMSE value of approximately 0.12 using 1 component compared to PLS alone achieving a RMSE value of approximately 0.15 using 5 components. It is clearly shown in Figure 4.3 that the RMSE values are similar within the range of about 0.12-0.15, which enables a visual comparison of independent stability regression coefficients. [154]

The RMSE values indicate the vector distance between predicted values and observed values. Random variables may be equated as the errors. Some errors include, but are not limited to, miscalibration of the gas sensors and measurement noise from environmental contamination. Correction for the bias from the gas sensors are assumed to be known and this value is removed

from the acquired raw gas sensor data. The standard deviation of the unknown errors can be estimated for a single observation rather than the total error. The RMSE provides an indication of the model's subsequent prediction. If the model indicates that the model does not become more accurate with more observations, then the model is not configured for the inclusion of noise that is influencing the data. Although Figure 4.3 shows that the model fit improves by adding in 1 component and worsens when 3 components are added, the model is capable of predicting observed data because the noise is small, within the range 0.12-0.15. For breath analysis applications, this error is considered small. The combination of advanced mathematical principles with underlying error assumptions applied to the acquired data, the parameters of the model may be adjusted for a highly probable RMSE range between 0.12-0.15. Thus, any RMSE values below 0.12 would not provide a meaningful predictive interpretation from the model.

4.1.4 Selected Characteristic Features

In order to determine the stability of the model, the variability of regression coefficients derived by PLS or PLS with OSC are compared. As previously mentioned in Chapter 3.2, the output responses of the MQ-2 and MQ-135 gas sensors have 400 points. A stability comparison is difficult because the regression coefficient is determined by using the average of the 400 points from the output response of the gas sensor and is associated with the following equation, $(400 \times 5 + 1)$. Studies have indicated that the average value obtained from the points of acquired gas sensor data result in a decrease in dimensionality, leaving $(5+1)$ coefficients for comparison [130].

4.1.5 Stability Test

For the five cycles of the PLS application and the PLS application with OSC, the regression coefficients have an associated coefficient variation that is determined. Initially, the model was

established using a single component and then another component was subsequently added to the second cycle so that the final cycle has 5 components. 6 times the regression coefficients and the RMSE are obtained from the dataset being divided on 6 subsets. Upon completion of the first and second cycle, the ratio of the standard deviation over the mean of each of the two coefficients and the average of the 6 RMSE values, the coefficient of variation is determined. PCA plots of the datasets using the Microsoft Excel Analyse-It PCA Analysis tool were utilized for illustrating Figure 4.2. The coefficient of variation of the regression coefficient from using PLS with OSC are about ten times less than the use of PLS alone. The most ideal RMSE results are observed with 1 component during the incorporation of the OSC method and with 5 components with PLS alone sharing an RMSE of about 0.15%. As a result of the implementation of these methods, the comparison of each independent stability regression coefficient may be achieved.

Chapter 5: Conclusions

The design and assembly of an electronic nose with an array of selective gas sensors with distinct output responses to alcohol, CO, and acetone was described. The electronic nose device had electrical components including Arduino Uno microcontrollers, MOS based MQ-2 and MQ-135 gas sensors connected to an internal bladder, and a Bosch BME280 sensor. An experimental evaluation of the electronic nose device indicated that the process of exposing gases from a formulated COVID-19 breath sample solution across the sensing element of the gas sensors produced a baseline drift phenomenon. Signal processing of the MQ-2 and MQ-135 gas sensors are a critical signal correction step in addressing the drift effects of these sensors. Ability of the internal bladder-attached MQ-2 and MQ-135 gas sensor in real-time gas identification was investigated. Chosen sections of the output response were applied to generate diverse features for gas classification. A reference measurement associated with the output resistance of the gas sensor is obtained at the conclusion of purging the chamber with pressurized oxygen during the cleaning process (G_{final}). PLS with OSC was performed to enhance the gas quantification performance in regression models and to distinguish between five differing concentrations of COVID-19 breath simulation solution was demonstrated.

In this Dissertation, an experimental set-up was designed and implemented to acquire gas sensor output responses in a dataset from the MQ-2 and MQ-135 gas sensors exposed to concentrations of 10 ppm, 50 ppm, 100 ppm, 200 ppm, and 300 ppm of COVID-19 breath simulation solution. It was shown during PCA of the datasheet that PLS with OSC is ideal for

concentration discrimination of the COVID-19 breath simulation solution. A comparison of the stability and accuracy of the regression model with the application of PLS and PLS with OSC resulted in an increased accuracy with both methods, however, the PLS with OSC method required less components than with PLS alone to achieve the same performance [127]. Regression model stability based on the differing of regression coefficients of the PLS and PLS with OSC models have been observed and results indicate that in light of the PLS and PLS with OSC models having similar accuracy, the PLS with OSC model is more robust due to its reliance on less variables than the PLS model counterpart [143]. The results that were obtained in this Dissertation indicate increased classification rates are contingent on the extracted features from the output response for real-time gas identification. Result measurements of this electronic nose configuration can contribute to the design of a real-time single sensor or a sensor array for rapid gas identification and decrease the drift phenomenon due to prolonged exposition of the sensing element in MOS based gas sensors.

The sampling and analysis of exhaled breath to determine a variety of biomarkers in disease has been explored. These investigations are implemented to gain a noninvasive insight to the diagnosis and the monitoring of progression of diseases such as lung disease, airway inflammatory disease, liver disease, and viral induced diseases such as COVID-19. Structural configuration and sensor array materials of the electronic nose devices have been shown to impact the gas sensor accuracy and selectivity for a target gas as it relates to a desired signature of disease in simulated COVID-19 breath sample analysis. Further, the sensor type, the concentration of sample solution, and flow of the electronic nose system have been shown to influence the amount of CO, alcohol, and acetone gas detected. The measured quantity of a plurality of detected gasses within breath ultimately defines a unique signature over time.

To date, the direct link between SARS-CoV-2 gaining access to the nervous system through the olfactory nerve to invoke reversible anosmia and COVID-19 induced inflammatory multisystem syndrome remains unexplored and represents a major gap in knowledge about SARS-CoV-2 cellular entry and associated detectable biomarkers of COVID-19. Thus, research was conducted to elucidate the olfactory nerve's role in viral entry of SARS-CoV-2 to the nervous system and to determine further quantitative biomarkers associated its immune response in an effort to gain insights in expanding the scope of the breath pattern signature of detecting COVID-19. A highly specified sensor array detection system may be capable of identifying inflammatory biomarkers of COVID-19 from the breath of an individual. Accordingly, the role of electrochemical and semiconductor-based detection sensors as well as canine detection of these viral components and/or inflammatory biomarkers under ambient and pathological conditions have been researched. Although there are ongoing efforts in breath analysis research addressing the standardization sampling, analytic, and reporting to correlate the data of the studies so that the data may be better interpreted, modifications to existing electronic nose devices are required to address the drift problem as for example, the MQ-135 sensor may have demonstrated.

The magnitude of how rapidly the COVID-19 virus could spread and infect others facilitated the need for a rapid COVID-19 test, accessible and affordable for both children and adults worldwide. As a result, an infected patient can quickly quarantine and isolate to slow the spread. Our research group has determined VOCs associated with COVID-19 and has built a prototype gas analysis system similar to a breathalyzer for detecting gasses of COVID-19. Some of the symptoms like headaches, coughing, and diarrhea result in an inflammatory response to create a unique variety of gasses like acetone, hydrogen, and carbon monoxide that can be detected when they are exhaled through a person's breath. A sample of a person's breath is first collected

in a chamber when a patient breaths into the valve, the gas sensors then detect a voltage change when they contact a COVID-19 target gas. The concentration in parts-per-million is calculated based on the non-linear resistance ratio of the target gas and clean air. Log-based scale calculations and post-data processing calibrate the sensors to increase the accuracy and selectivity. Finally, the voltages and PPM of the target gas concentration data is stored in a computer database and sensor coding reveals the resulting breath pattern signature of COVID-19. Although, this system may also be modified to sniff out other pathogens of disease, spoiled meats, and ripened fruit, we are dedicated to build a gas sensor platform for low cost, noninvasive, and rapid detection of the breath pattern signature of COVID-19, in an attempt to slow the spread of the global health threat of infection and in turn to help save lives.

Chapter 6: Recommended Applications

The use of real-time electronic nose technologies and scent trained canines have been used for detection of various molds, viruses, and bacterial agents that may impact, for example, the quality of an indoor space. A biodetection canine can be trained to successfully pinpoint a particular volatile organic compound (VOC) associated with a metabolic byproduct of infection [138]. For example, a trained scent dog experimental study indicated canine capabilities for the detection of SARS-CoV-2 having a measured sensitivity of 82.63% and a specificity of 96.35% when the trained dog sniffed saliva and bodily secretions during the sampling method [138]. Within the coronavirus family, seven viruses are currently known to infect humans, including, NL63 and 229E from the alpha genus and OC43, HKU1, SARS-CoV, MERS-CoV, and SARS-CoV-2 from the beta genus [139]. Of these seven viruses, studies have indicated infected SARS-CoV-2 individuals have significant exhaled breath concentrations of ethanal, octanal, acetone, butanone, and methanol capable of distinguishing between non-SARS-CoV-2 infected individuals and SARS-CoV-2 infected individuals as shown in Table 6.1. Although the VOCs of the remaining six viruses of the coronavirus family have not been made available, breath analysis studies investigating the exhaled breath VOCs of individuals infected with other pathogens of disease such as, viruses and bacteria may provide clues to specific metabolic byproducts of infection within the coronavirus family. Although dogs have been cited as having a history of identifying medical diseases, they can be trained to detect a variety of other compounds such as those found in indoor emissions emitted from contamination sources such as, building materials, cleaning products,

Table 6.1 Volatile organic compounds (VOCs) of indoor pathogens including, bacteria, viruses, and different genera of molds capable of impacting a healthy indoor space.

Pathogen	VOC	Source	Reference
<i>Staphylococcus aureus</i>	Isovaleric acid, 2-methyl-methylbutanol	Bacteria	[136]
<i>Pseudomonas aeruginosa</i>	1-undecane, 2, 4-dimethyl-1-heptane, 2-butanone, 2-propanol, Ammonia, 2-acetophenone, Hydrogen cyanide, Methyl thiocyanide	Bacteria	[136]
<i>Escherichia coli</i>	Methanol, Pentanol, Ethyl acetate, Indole, 1-octanol, hexanol	Bacterial	[136]
<i>Klebsiella pneumoniae</i>	2,2,4,4,tetramethyloxolane, 3-Z-octenyl acetate, 3-methylcyclohexene	Bacteria	[136]
<i>Mycobacterium tuberculosis</i>	Cymol 4-methyldodecane methyl nicotinate 4-methyldodecane	Bacteria	[136]
<i>Haemophilus influenzae</i>	γ -butyrolactone	Bacteria	[136]
<i>Helicobacter pylori</i>	CO	Bacteria	[138]
<i>Clostridium difficile</i>	4-methylpentanoate, 4-methylpentanoic acid 1-methyl-2-(1-methylethyl)-benzene	Bacteria	[136]
<i>Respiratory Syncytial Virus (RSV)</i>	Styrene	Virus	[137]
<i>SARS-CoV-2</i>	Ethanal, Octanal, Acetone, Butanone, Methanol	Virus	[98]
<i>Influenza A</i>	Acetaldehyde, Acetone, Isoprene,	Virus	[12], [137], [140]
Influenza virus H ₁ N ₁	2-methoxy-ethanol	Virus	[140]
<i>Human rhinovirus</i>	Acetone	Virus	[140]
<i>Penicillium pinophilum</i>	Alcohols	Mold	[131], [133]
<i>Aspergillus niger</i>	Alcohols and Isoprene,	Mold	[131], [133], [134]

furniture, human activities, and different genera of molds, contributing to toxicity and adverse respiratory problems such as, asthma and rhinitis [131]. Studies have indicated that microbial activity of common household mold, *Aspergillus niger*, is associated with VOCs emitted based on indoor environmental factors such as temperature, humidity, and lighting [134], [135]. Further, VOC emissions of molds are heavily influenced by the cultivation growth time and the type of substrate such as drywall, wallpaper, or wood that the mold is growing on [134].

The successful biodetection of canines is attributed to their enhanced olfactory system being densely packed with neurons, functional genes, and gene encoding receptors. Further, canines have an enlarged olfactory epithelium and a bulbous olfactory bulb. Electronic nose technologies are developed to mimic the highly accurate perception of bioeffluents that scent dogs possess. Bioeffluents are best detected indoors, as they are emitted from exhaled breath and dermal emissions, to reflect the metabolic state of an individual as it pertains to infectious disease VOC expression [132], [138]. As our understanding of infectious diseases such as COVID-19 improves, we expect these diagnostic devices to include a diversity of other MOS-based gas sensors and electrochemical sensors, including but not limited to, an SGX-4NO-250 Nitric Oxide sensor or a P-NUCLEO-IKA02A1 electrochemical toxic gas sensor board with a CO sensor, that can detect changes associated with the pathogenesis of the disease. In addition, the research results provide for the advancement of electronic nose technology. In particular, this testbed prototype continues its ongoing developmental progress of incorporating mucus-based electrochemical transistors at the Dept. of Electrical Engineering, USF, Tampa, campus led by Dr. Arash Takshi.

There are at least four directions for the application of this Dissertation research of eNose technology. The first direction is for the detection of VOC biomarkers of a chronic disease such as asthma, multiple sclerosis, or cancer. This noninvasive eNose prototype may be implemented

for both the diagnosis and progression of these types of disease. Secondly, the differentiation between disease variants such as those in the coronavirus family may be accomplished with this eNose prototype. Each disease variant may have a unique VOC breath pattern signature differing from subsequent variants. For this application, once the VOCs are established, there would be minimal hardware updates to the eNose. For example, gas sensors would be added or removed to correspond to the desired VOC biomarker of interest. The flexibility of an eNose device to be configured for detection of a plurality of variants of disease is a feature that currently overcomes limitations of PCR COVID-19 testing only the RNA only. In a third direction for extending this research, the eNose prototype could be easily configured to acquire gas data to show differentiation between a first subject and a second subject. For example, healthy individuals may emit varying amounts of VOC concentrations based on their health, environmental exposure to contaminants, and diet. Two individuals will not have the same exact breath pattern signature and eNose data may be analyzed to determine the presence of certain breath patterns and potential influences of the biological and/or environmental source of these biomarkers. Finally, the fourth direction in which this Dissertation research may be extended is for the application of advanced mathematical signal correction techniques to control variation of variables and to eliminate noise.

References

- [1] Germanese, Danila, et al. "An E-Nose for the Monitoring of Severe Liver Impairment: A Preliminary Study." *Sensors* (14248220), vol. 19, no. 17, Sept. 2019, p. 3656. EBSCOhost,search.ebscohost.com/login.aspx?direct=true&db=edb&AN=138734963&site=eds-live.
- [2] Doty, Anna C., et al. "Assessment of the Portable C-320 Electronic Nose for Discrimination of Nine Insectivorous Bat Species: Implications for Monitoring White-Nose Syndrome." *Biosensors* (2079-6374), vol. 10, no. 2, Feb. 2020, p. 12. EBSCOhost,doi:10.3390/bios10020012.
- [3] Gouma, Pelagia-Irene (Port Jefferson, NY), and Sanford R.(Stony Brook, NY) Simon. *Selective Nanoprobe for Olfactory Medicine*. 20140624 2014. EBSCOhost,search.ebscohost.com/login.aspx?direct=true&db=edspgr&AN=edspgr.08758261&site=eds-live.
- [4] Gouma, Pelagia-Irene (Port Jefferson, NY), and Milutin (Forest Hills, NY) Stanacevic. *Gas Sensor with Compensations for Baseline Variations*. 20150217 2015. EBSCOhost,search.ebscohost.com/login.aspx?direct=true&db=edspgr&AN=edspgr.08955367&site=eds-live.
- [5] Miekisch, W., et al. "Diagnostic Potential of Breath Analysis-Focus on Volatile Organic Compounds." *CLINICA CHIMICA ACTA*, no. 1-2, 2004, p. 25. EBSCOhost,search.ebscohost.com/login.aspx?direct=true&db=edsbl&AN=RN153916388&site=eds-live.
- [6] Mats J. Olsson, et al. "The Scent of Disease: Human Body Odor Contains an Early Chemosensory Cue of Sickness." *Psychological Science*, vol. 25, no. 3, 2014, p. 817.
- [7] RodrA-guez-Aguilar, Maribel, et al. "Ultrafast Gas Chromatography Coupled to Electronic Nose to Identify Volatile Biomarkers in Exhaled Breath from Chronic Obstructive Pulmonary Disease Patients: A Pilot Study." *Biomedical Chromatography*, no. 12, 2019. EBSCOhost, doi:10.1002/bmc.4684.
- [8] He, L., et al. (2006), "Expression of elevated levels of pro-inflammatory cytokines in SARS-CoV-infected ACE2+ cells in SARS patients: relation to the acute lung injury and pathogenesis of SARS." *J. Pathol.*, 210: 288-297. doi:10.1002/path.2067M.

- [9] Ryan, M. A., et al. "Monitoring Space Shuttle Air Quality Using the Jet Propulsion Laboratory Electronic Nose." *IEEE Sensors Journal*, vol. 4, no. 3, June 2004, p. 337. EBSCOhost, search.ebscohost.com/login.aspx?direct=true&db=edb&AN=52148782&site=eds-live.
- [10] Wang, Pei. "Combination of Serological Total Antibody and RT-PCR Test for Detection of SARS-COV-2 Infections." *Journal of Virological Methods*, vol. 283, Sept. 2020. EBSCOhost, doi:10.1016/j.jviromet.2020.113919.
- [11] Bruno E, Alessandrini M, Ottaviani F, et al. "Can the electronic nose diagnose chronic rhinosinusitis? A new experimental study." *Eur Arch Otorhinolaryngol*. 2008;265(4):425-428. doi:10.1007/s00405-007-0477-8
- [12] Sethi, S., et al. "Clinical Application of Volatile Organic Compound Analysis for Detecting Infectious Diseases." *CLINICAL MICROBIOLOGY REVIEWS*, no. 3, 2013, p. 462. EBSCOhost, search.ebscohost.com/login.aspx?direct=true&db=edsbl&AN=RN336747002&site=eds-live.
- [13] Mohamed E, Bruno E, Linder R, Alessandrini M, Di Girolamo A, Poppl SJ, De Lorenzo A. 2003. A novel method for diagnosing chronic rhinosinusitis based on an electronic nose. *An. Otorhinolaryngol. Ibero Am*. 30:447–457
- [14] Chen, Haoxuan et al. "Breath-borne VOC Biomarkers for COVID-19." Research Gate, to be published. doi:10.1101/2020.06.21.20136523.
- [15] Cipollaro, Lucio, et al. "Musculoskeletal Symptoms in SARS-CoV-2 (COVID-19) Patients." *Journal of Orthopaedic Surgery & Research*, vol. 15, no. 1, May 2020, pp. 1–7. EBSCOhost, doi:10.1186/s13018-020-01702-w.
- [16] Zhou, Zili, et al. "Effect of Gastrointestinal Symptoms in Patients With COVID-19." *Gastroenterology (00165085)*, vol. 158, no. 8, June 2020, p. 2294. EBSCOhost, search.ebscohost.com/login.aspx?direct=true&db=edo&AN=143598414&site=eds-live.
- [17] Hartman, Matthew E et al. "COVID-19 Respiratory Failure: Targeting Inflammation on VV-ECMO Support." *ASAIO journal (American Society for Artificial Internal Organs : 1992)* vol. 66,6 (2020): 603-606. doi:10.1097/MAT.0000000000001177
- [18] Boesveldt, Sanne et al. "Anosmia-A Clinical Review." *Chemical senses* vol. 42,7 (2017): 513-523. doi:10.1093/chemse/bjx025j
- [19] Marinosci, Annalisa et al. "Possible link between anosmia and COVID-19: sniffing out the truth." *European archives of oto-rhino-laryngology : official journal of the European Federation of Oto-Rhino-Laryngological Societies (EUFOS) : affiliated with the German Society for Oto-Rhino-Laryngology - Head and Neck Surgery*, 1–2. 17 Apr. 2020, doi:10.1007/s00405-020-05966-0

- [20] van Riel D, Verdijk R, Kuiken T. The olfactory nerve: a shortcut for influenza and other viral diseases into the central nervous system. *J Pathol.* 2015;235:277–287. doi: 10.1002/path.4461.
- [21] Sungnak, Waradon et al. “SARS-CoV-2 Entry Factors Are Highly Expressed in Nasal Epithelial Cells Together with Innate Immune Genes.” *Nature Medicine* 26.5 (2020): 681–687. Crossref. Web.
- [22] Henderson, B. et al. “A benchmarking protocol for breath analysis: the peppermint experiment.” *J Breath Res.* 2020 Aug 10;14(4):046008. doi: 10.1088/1752-7163/aba130. PMID: 32604084
- [23] Seo, Giwan et al. “Rapid Detection of COVID-19 Causative Virus (SARS-CoV-2) in Human Nasopharyngeal Swab Specimens Using Field-Effect Transistor-Based Biosensor.” *ACS nano* vol. 14,4 (2020): 5135-5142.
- [24] Stephen D. Roper, Chapter 39 - Gustatory and Olfactory Sensory Transduction, Editor(s): Nicholas Sperelakis, *Cell Physiology Source Book (Fourth Edition)*, Academic Press, 2012, Pages 681-697, ISBN 9780123877383, <https://doi.org/10.1016/B978-0-12-387738-3.00039-1>. (<http://www.sciencedirect.com/science/article/pii/B9780123877383000391>)
- [25] Wang, Qihui, et al. “Structural and Functional Basis of SARS-CoV-2 Entry by Using Human ACE2.” *Cell*, vol. 181, no. 4, May 2020, pp. 894–904.
- [26] Timothy D. Smith, Kunwar P. Bhatnagar, Chapter 2 - Anatomy of the olfactory system, Editor(s): Richard L. Doty, *Handbook of Clinical Neurology*, Elsevier, Volume 164, 2019, Pages 17-28, ISSN 0072-9752, ISBN 9780444638557, <https://doi.org/10.1016/B978-0-444-63855-7.00002-2>. (<http://www.sciencedirect.com/science/article/pii/B9780444638557000022>)
- [27] Joseph, Albert, and Gabriele C. DeLuca. “Back on the Scent: The Olfactory System in CNS Demyelinating Diseases.” *Journal of Neurology, Neurosurgery & Psychiatry*, vol. 87, no. 10, Oct. 2016, pp. 1146–1154. EBSCOhost, doi:10.1136/jnnp-2015-312600.
- [28] Akaike, T., et al. “Free Radicals in Viral Pathogenesis: Molecular Mechanisms Involving Superoxide and NO.” *Proceedings of the Nutrition Society*, vol. 217, no. 1, Jan. 1998, p. 64. EBSCOhost, search.ebscohost.com/login.aspx?direct=true&db=egh&AN=577275&site=eds-live.
- [29] Stefano, George B., et al. “Potential Immunoregulatory and Antiviral/SARS-CoV-2 Activities of Nitric Oxide.” *Medical Science Monitor*, vol. 26, May 2020, p. 1. EBSCOhost, search.ebscohost.com/login.aspx?direct=true&db=edb&AN=143487470&site=eds-live.
- [30] Lundberg JO. Airborne nitric oxide: inflammatory marker and aerocrine messenger in man. *Acta Physiol Scand Suppl.* 1996;633:1-27.

- [31] Molloy, E.J., Bearer, C.F. COVID-19 in children and altered inflammatory responses. *Pediatr Res* (2020). <https://doi.org/10.1038/s41390-020-0881-y>
- [32] Cynthia Liu, Qiongqiong Zhou, Yingzhu Li, Linda V. Garner, Steve P. Watkins, Linda J. Carter, Jeffrey Smoot, Anne C. Gregg, Angela D. Daniels, Susan Jervey, and Dana Albaiu. “Research and Development on Therapeutic Agents and Vaccines for COVID-19 and Related Human Coronavirus Diseases.” *ACS Central Science* 2020 6 (3), 315-331. DOI: 10.1021/acscentsci.0c00272
- [33] Babizhayev MA, and Deyev AI. “Management of the Virulent Influenza Virus Infection by Oral Formulation of Nonhydrolyzed Carnosine and Isopeptide of Carnosine Attenuating Proinflammatory Cytokine-Induced Nitric Oxide Production.” *American Journal of Therapeutics*, vol. 19, no.1, Jan. 2012, pp. e25-47. EBSCOhost, search.ebscohost.com/login.aspx?direct=true&db=cin20&AN=108218670&site=eds-live
- [34] Craig eAngle, et al. “Real-Time Detection of a Virus Using Detection Dogs.” *Frontiers in Veterinary Science*, vol. 2, Jan. 2016. EBSCOhost, doi:10.3389/fvets.2015.00079.
- [35] Iravani, Behzad, et al. “Non-Invasive Recording from the Human Olfactory Bulb.” *Nature Communications*, vol. 11, no. 1, Jan. 2020, p. 1. EBSCOhost, search.ebscohost.com/login.aspx?direct=true&db=edb&AN=141512632&site=eds-live.
- [36] M. Cascella, et al. "Features, evaluation, and treatment coronavirus (COVID-19)," [Updated 2020 Mar 20]. In: StatPearls [Internet]. Treasure Island (FL): StatPearls Publishing; 2020 Jan-. Available from: <https://www.ncbi.nlm.nih.gov/books/NBK554776/J>. Clerk Maxwell, A Treatise on Electricity and Magnetism, 3rd ed., vol. 2. Oxford: Clarendon, 1892, pp.68–73.
- [37] J.T. Ortega, et al. "Role of changes in Sars-Cov-2 spike protein in the interaction with the human ACE2 receptor: An In Silico Analysis," *EXCLI Journal* 19 (2020): 410-417.
- [38] A.C. Walls, et al. “Structure, function, and antigenicity of the SARS-CoV-2 spike glycoprotein,” *Cell*. 2020 Mar 9 doi: 10.1016/j.cell.2020.02.058
- [39] Bruce M. Wenig (2009) Undifferentiated Malignant Neoplasms of the Sinonasal Tract. *Archives of Pathology & Laboratory Medicine*: May 2009, Vol. 133, No. 5, pp. 699-712.
- [40] M. Gui, et al. “Cryo-electron microscopy structures of the SARS-CoV spike glycoprotein reveal a prerequisite conformational state for receptor binding,” *Cell Res*. 2017 Jan; 27(1): 119–129. Published online 2016 Dec 23. doi: 10.1038/cr.2016.152M. Young, *The Technical Writer's Handbook*. Mill Valley, CA: University Science, 1989.
- [41] Princivalle, A., Monasta, L., Butturini, G. et al. Pancreatic ductal adenocarcinoma can be detected by analysis of volatile organic compounds (VOCs) in alveolar air. *BMC Cancer* 18, 529 (2018). <https://doi.org/10.1186/s12885-018-4452-0>

- [42] Sethi, Shneh et al. "Clinical application of volatile organic compound analysis for detecting infectious diseases." *Clinical microbiology reviews* vol. 26,3 (2013): 462-75. doi:10.1128/CMR.00020-13
- [43] M. Vaduganathan, et al., "Renin–Angiotensin–Aldosterone System Inhibitors in Patients with Covid-19," *The New England Journal of Medicine*. April 2020. 10.1056/NEJMs2005760 [doi]. <https://www.nejm.org/doi/full/10.1056/NEJMs2005760J>
- [44] Hoffmann, Markus et al. "Priming Time: How Cellular Proteases Arm Coronavirus Spike Proteins." *Activation of Viruses by Host Proteases* 71–98. 16 Feb. 2018, doi:10.1007/978-3-319-75474-1_4
- [45] RodrA-guez-Aguilar, Maribel, et al. "Ultrafast Gas Chromatography Coupled to Electronic Nose to Identify Volatile Biomarkers in Exhaled Breath from Chronic Obstructive Pulmonary Disease Patients: A Pilot Study." *Biomedical Chromatography*, no. 12, 2019. EBSCOhost, doi:10.1002/bmc.4684.
- [46] Hui-Ling Yen, et al. "SARS-CoV-2 Viral Load in Upper Respiratory Specimens of Infected Patients." *New England Journal of Medicine*, vol. 382, no. 12, Mar. 2020, pp. 1177–1179. EBSCOhost, doi:10.1056/NEJMc2001737.
- [47] Galougahi, Mahboobeh Karimi et al. "Olfactory Bulb Magnetic Resonance Imaging in SARS-CoV-2-Induced Anosmia: The First Report." *Academic radiology*, S1076-6332(20)30194-X. 11 Apr. 2020, doi:10.1016/j.acra.2020.04.002
- [48] D. Dong et al., "The role of imaging in the detection and management of COVID-19: a review," in *IEEE Reviews in Biomedical Engineering*, doi: 10.1109/RBME.2020.2990959.
- [49] Zamuruyev, Konstantin O et al. "Human breath metabolomics using an optimized non-invasive exhaled breath condensate sampler." *Journal of breath research* vol. 11,1 016001. 22 Dec. 2016, doi:10.1088/1752-7163/11/1/016001
- [50] S. Knasmüller and M. French, *The Micronucleus Assay in Toxicology*. The Royal Society of Chemistry, 2019.
- [51] D. Caruso, et al. "Effect of short and long term gonadectomy on neuroactive steroid levels in the central and peripheral nervous system of male and female rats," *Journal of neuroendocrinology*, vol. 22, no. 11, pp. 1137-1147, 2010.
- [52] Doty RL, Kamath V. The influences of age on olfaction: a review. *Front Psychol*. 2014;5:20. doi: 10.3389/fpsyg.2014.00020.
- [53] Angle, Craig et al. "Canine Detection of the Volatilome: A Review of Implications for Pathogen and Disease Detection." *Frontiers in veterinary science* vol. 3 47. 24 Jun. 2016, doi:10.3389/fvets.2016.00047

- [54] Kim, Jeong-Min et al. "Identification of Coronavirus Isolated from a Patient in Korea with COVID-19." *Osong public health and research perspectives* vol. 11,1 (2020): 3-7. doi:10.24171/j.phrp.2020.11.1.02
- [55] Cheung, Chung Y et al. "Cytokine responses in severe acute respiratory syndrome coronavirus-infected macrophages in vitro: possible relevance to pathogenesis." *Journal of virology* vol. 79,12 (2005): 7819-26.
- [56] Mats J. Olsson, et al. "The Scent of Disease: Human Body Odor Contains an Early Chemosensory Cue of Sickness." *Psychological Science*, vol. 25, no. 3, 2014, p. 817.
- [57] P. Millet, M. Opiekun, T. Martin, G. K. Beauchamp, and B. A. Kimball, "Cytokine contributions to alterations of the volatile metabolome induced by inflammation," *Brain Behavior and Immunity*, p. 312, 2018.
- [58] Lei Gao, Yongsheng Ding, Hua Dai, Zhende Huang and Shihuang Shao, "A novel fingerprint map of SARS-CoV with visualization analysis," *Third International Conference on Image and Graphics (ICIG'04)*, Hong Kong, China, 2004, pp. 226-229, doi: 10.1109/ICIG.2004.18.
- [59] Hussain M1, Jabeen N2, Raza F1, Shabbir S1,2, Baig AA1, Amanullah A1, Aziz B1. Structural variations in human ACE2 may influence its binding with SARS-CoV-2 spike protein. *J Med Virol*. 2020 Apr 6. doi: 10.1002/jmv.25832. [Epub ahead of print]
- [60] S.G. Waxman, "Axonal conduction and injury in multiple sclerosis: the role of sodium channels," *Nature Reviews Neuroscience*, no. 12, p. 932. 2006.
- [61] Craven, Brent A., et al. "The Fluid Dynamics of Canine Olfaction: Unique Nasal Airflow Patterns as an Explanation of Macrosmia." *Journal of The Royal Society Interface*, vol. 7, no. 47, June 2010, p. 933.
- [62] DeLuca, Gabriele C., et al. "Olfactory Pathology in Central Nervous System Demyelinating Diseases." *Brain Pathology*, vol. 25, no. 5, Sept. 2015, p. 543.
- [63] Garcia-Gonzalez, D., et al. "Olfactory System and Demyelination." *ANATOMICAL RECORD -NEW SERIES-*, no. 9, 2013, p. 1424.
- [64] Collins, L. N., et al. "Myelination of the Developing Lateral Olfactory Tract and Anterior Commissure." *Journal of Comparative Neurology*, vol. 526, no. 11, Aug. 2018, p. 1843. EBSCOhost, search.ebscohost.com/login.aspx?direct=true&db=edb&AN=130000643&site=eds-live.
- [65] Fukushima, Nanae, et al. "Acetyl-L-Carnitine Enhances Myelination of Regenerated Fibers of the Lateral Olfactory Tract." *Neuroscience Letters*, vol. 653, July 2017, pp. 215-219. EBSCOhost, doi:10.1016/j.neulet.2017.06.001.

- [66] Paterson, Ross, et. al. “The emerging spectrum of COVID-19 neurology: clinical, radiological and laboratory findings.” *Brain*, (2020), awaa240, <https://doi.org/10.1093/brain/awaa240>
- [67] Kremer, Stephane, et al. “Brain MRI Findings in Severe COVID-19: A Retrospective Observational Study.” *Radiological Society of North America*, 2020. SN 0033-8419, 10.1148/radiol.2020202222, <https://doi.org/10.1148/radiol.2020202222>
- [68] F.J. Hernández Ramos, A. Palomino García, & M.D. Jiménez Hernández. (2020). Neurology during the pandemic. Is COVID-19 changing the organisation of neurology departments? *Neurología (English Edition)*, 35(4), 269–271. <https://doi-org.ezproxy.lib.usf.edu/10.1016/j.nrleng.2020.04.008>
- [69] Montalvan, V et al. “Neurological manifestations of COVID-19 and other coronavirus infections: A systematic review.” *Clinical neurology and neurosurgery* vol. 194 (2020): 105921. doi:10.1016/j.clineuro.2020.105921
- [70] Wang, Lei et al. “Clinical manifestations and evidence of neurological involvement in 2019 novel coronavirus SARS-CoV-2: a systematic review and meta-analysis.” *Journal of neurology*, 1–13. 11 Jun. 2020, doi:10.1007/s00415-020-09974-2
- [71] Escalada Pellitero S, Garriga Ferrer-Bergua L. Paciente con clínica neurológica comoúnica manifestación de infección por SARS-CoV-2. *Neurología*. 2020;35:271—272.
- [72] Toscano, Gianpaolo, et al. “Guillain-Barré Syndrome Associated with SARS-CoV-2.” *New England Journal of Medicine*, vol. 382, no. 26, June 2020, pp. 2574–2576. EBSCOhost, doi:10.1056/NEJMc2009191.
- [73] Neil M. Borden, MD, et al. *Imaging Anatomy of the Human Brain : A Comprehensive Atlas Including Adjacent Structures*. Demos Medical, 2016. EBSCOhost, search.ebscohost.com/login.aspx?direct=true&db=nlebk&AN=1081584&site=eds-live.
- [74] “Olfactory Pathways and Limbic System.” Pp. 903-904. [http://www.neuroanatomy.wisc.edu/coursebook/neuro3\(2\).pdf](http://www.neuroanatomy.wisc.edu/coursebook/neuro3(2).pdf)
- [75] Takeshi Moriguchi, et al. “A First Case of Meningitis/Encephalitis Associated with SARS-Coronavirus-2.” *International Journal of Infectious Diseases*, vol. 94, no. 55–58, May 2020, pp. 55–58. EBSCOhost, doi:10.1016/j.ijid.2020.03.062.
- [76] M. Palao , E. Fernandez-D ´ ıaz , J. Gracia-Gil , C.M. Romero-Sanchez , I. D ´ ıaz-Maroto , T. Segura , Multiple Sclerosis following SARS-CoV-2 infection, *Multiple Sclerosis and Related Disorders* (2020), doi: <https://doi.org/10.1016/j.msard.2020.102377>
- [77] Ren, Huihui, et al. “Association of the Insulin Resistance Marker TyG Index with the Severity and Mortality of COVID-19.” *Cardiovascular Diabetology*, vol. 19, no. 1, May 2020, pp. 1–8. EBSCOhost, doi:10.1186/s12933-020-01035-2.

- [78] Vargas-Vargas M and Cortés-Rojo C. Ferritin levels and COVID-19. *Rev Panam Salud Publica*. 2020;44:e72. <https://doi.org/10.26633/RPSP.2020.72>
- [79] Vlasić Z, Dodig S, Cepelak I, et al. Iron and ferritin concentrations in exhaled breath condensate of children with asthma. *J Asthma*. 2009;46(1):81-85. doi:10.1080/02770900802513007
- [80] Ashmawi, Samiha & Diab, Haytham & Fahmy, Elsayed. (2015). "Evaluation of Lung Cancer by Estimating Ferritin in Exhaled Breath Condensate." *Egyptian Journal of Chest Diseases and Tuberculosis*. 19. 10.1016/j.ejcdt.2014.08.002.
- [81] Balbi, Bruno et al. "Exhaled Breath Condensate: Technical and Diagnostic Aspects." *The Scientific World Journal*, (2015). 435160. <https://doi.org/10.1155/2015/435160>, doi: 10.1155/2015/435160
- [82] Casaletto KB, Ward ME, Baker NS, et al. "Retinal thinning is uniquely associated with medial temporal lobe atrophy in neurologically normal older adults. *Neurobiol Aging*." 2017;51:141-147. doi:10.1016/j.neurobiolaging.2016.12.011
- [83] Hideshima, Sho & Hayashi, Hiroki & Hinou, Hiroshi & Nambu, Shunsuke & Kuroiwa, Shigeki & Nakanishi, Takuya & Momma, Toshiyuki & Nishimura, Shin-Ichiro & Sakoda, Yoshihiro & Osaka, Tetsuya. (2019). Glycan-immobilized dual-channel field effect transistor biosensor for the rapid identification of pandemic influenza viral particles. *Scientific Reports*. 9. 10.1038/s41598-019-48076-6.
- [84] Ruskiewicz, Dorota M., et al. "Diagnosis of COVID-19 by Analysis of Breath with Gas Chromatography-Ion Mobility Spectrometry - a Feasibility Study." *EClinicalMedicine*, vol. 29–30, Dec. 2020. EBSCOhost, doi:10.1016/j.eclinm.2020.100609.
- [99] Shin, Woosuck. "Medical Applications of Breath Hydrogen Measurements." *Analytical & Bioanalytical Chemistry*, vol. 406, no. 16, June 2014, pp. 3931–3939. EBSCOhost, doi:10.1007/s00216-013-7606-6.
- [100] Gourab Dutta Banik, et al. "Hydrogen Sulphide in Exhaled Breath: A Potential Biomarker for Small Intestinal Bacterial Overgrowth in IBS." *Journal of Breath Research*, vol. 10, no. 2, June 2016, p. 1. EBSCOhost, search.ebscohost.com/login.aspx?direct=true&db=edb&AN=116190249&site=eds-live.
- [101] Lourenço, Célia, and Claire Turner. "Breath analysis in disease diagnosis: methodological considerations and applications." *Metabolites* vol. 4,2 465-98. 20 Jun. 2014, doi:10.3390/metabo4020465
- [102] Tatar, Moosa, et al. "Analysis of Excess Deaths During the COVID-19 Pandemic in the State of Florida." *American Journal of Public Health*, vol. 111, no. 4, Apr. 2021, pp. 704–707. EBSCOhost, doi:10.2105/AJPH.2020.306130.

- [103] Justus Kavita Mutuku, et al. “An Overview of Experiments and Numerical Simulations on Airflow and Aerosols Deposition in Human Airways and the Role of Bioaerosol Motion in COVID-19 Transmission.” *Aerosol and Air Quality Research*, no. 6, 2020, p. 1172. EBSCOhost, doi:10.4209/aaqr.2020.04.0185.
- [104] Chayu Yang, and Jin Wang. “Modeling the Transmission of COVID-19 in the US – A Case Study.” *Infectious Disease Modelling*, vol. 6, no. 195–211, Jan. 2021, pp. 195–211. EBSCOhost, doi:10.1016/j.idm.2020.12.006.
- [105] Ding, Siyuan, and T.Jake Liang. “Is SARS-CoV-2 Also an Enteric Pathogen With Potential Fecal–Oral Transmission? A COVID-19 Virological and Clinical Review.” *Gastroenterology*, vol. 159, no. 1, July 2020, pp. 53–61. EBSCOhost, doi:10.1053/j.gastro.2020.04.052.
- [106] Rannan-Eliya, Ravindra Prasan, et al. “Increased Intensity Of PCR Testing Reduced COVID-19 Transmission Within Countries During The First Pandemic Wave.” *Health Affairs*, vol. 40, no. 1, Jan. 2021, pp. 70–81. EBSCOhost, doi:10.1377/hlthaff.2020.01409.
- [107] Garg, Atul, et al. “Evaluation of Seven Commercial RT-PCR Kits for COVID-19 Testing in Pooled Clinical Specimens.” *Journal of Medical Virology*, vol. 93, no. 4, Apr. 2021, pp. 2281–2286. EBSCOhost, search.ebscohost.com/login.aspx?direct=true&db=edb&AN=148788299&site=eds-live.
- [108] Jose Luis Blanco, et al. “Overcoming the Slow Recovery of MOX Gas Sensors through a System Modeling Approach.” *Sensors*, vol. 12, no. 10, Oct. 2012, pp. 13664–13680. EBSCOhost, doi:10.3390/s121013664.
- [109] Righettoni, Marco, et al. “Breath Analysis by Nanostructured Metal Oxides as Chemo-Resistive Gas Sensors.” *Materials Today*, vol. 18, no. 3, Apr. 2015, pp. 163–171. EBSCOhost, doi:10.1016/j.mattod.2014.08.017.
- [110] Manuela Baietto, and Alphas D. Wilson. “Applications and Advances in Electronic-Nose Technologies.” *Sensors*, vol. 9, no. 7, June 2009, pp. 5099–5148. EBSCOhost, doi:10.3390/s90705099.
- [111] Sharma, R. K., et al. “Investigation of Stability and Reliability of Tin Oxide Thin-Film for Integrated Micro-Machined Gas Sensor Devices.” *SENSORS AND ACTUATORS B*, no. 1, 2001, p. 9. EBSCOhost, search.ebscohost.com/login.aspx?direct=true&db=edsbl&AN=RN105449033&site=eds-live.
- [112] Korotcenkov, G., and B. K. Cho. “Instability of Metal Oxide-Based Conductometric Gas Sensors and Approaches to Stability Improvement (Short Survey).” *Sensors & Actuators: B. Chemical*, vol. 156, no. 2, Jan. 2011, pp. 527–538. EBSCOhost, doi:10.1016/j.snb.2011.02.024.

- [113] Di Natale, C., et al. "Counteraction of Environmental Disturbances of Electronic Nose Data by Independent Component Analysis." *SENSORS AND ACTUATORS B*, no. 2–3, 2002, p. 158. EBSCOhost, search.ebscohost.com/login.aspx?direct=true&db=edsbl&AN=RN110247989&site=eds-live.
- [114] Marco, S., and A. Gutierrez-Galvez. "Signal and Data Processing for Machine Olfaction and Chemical Sensing: A Review." *IEEE Sensors Journal*, vol. 12, no. 11, Nov. 2012, pp. 3189–3214. EBSCOhost, doi:10.1109/JSEN.2012.2192920.
- [115] Hines, E. L., et al. "Electronic Noses: A Review of Signal Processing Techniques." *IEE PROCEEDINGS CIRCUITS DEVICES AND SYSTEMS*, no. 6, 1999, p. 297. EBSCOhost, search.ebscohost.com/login.aspx?direct=true&db=edsbl&AN=RN073462265&site=eds-live.
- [116] Gardner, J.W. & Bartlett, P.N.. (2000). *Electronic Noses. Principles and Applications. Measurement Science and Technology*. 11. 1087. 10.1088/0957-0233/11/7/702.
- [117] Llobet, E., et al. "Wavelet Transform and Fuzzy ARTMAP-Based Pattern Recognition for Fast Gas Identification Using a Micro-Hotplate Gas Sensor." *Sensors & Actuators: B. Chemical*, vol. 83, no. 1–3, Mar. 2002, pp. 238–244. EBSCOhost, doi:10.1016/S0925-4005(01)01047-4.
- [118] Zuppa, Marzia, et al. "Recovery of Drifting Sensor Responses by Means of DWT Analysis." *Sensors & Actuators: B. Chemical*, vol. 120, no. 2, Jan. 2007, pp. 411–416. EBSCOhost, doi:10.1016/j.snb.2006.02.049.
- [119] Ziyatdinov, A., et al. "Drift Compensation of Gas Sensor Array Data by Common Principal Component Analysis." *Sensors & Actuators: B. Chemical*, vol. 146, no. 2, Jan. 2010, pp. 460–465. EBSCOhost, doi:10.1016/j.snb.2009.11.034.
- [120] Marco, S., et al. "Gas Identification with Tin Oxide Sensor Array and Self Organizing Maps: Adaptive Correction of Sensor Drifts." *IEEE Instrumentation and Measurement Technology Conference Sensing, Processing, Networking. IMTC Proceedings, Instrumentation and Measurement Technology Conference, 1997. IMTC/97. Proceedings. Sensing, Processing, Networking., IEEE*, vol. 2, Jan. 1997, p. 904. EBSCOhost, doi:10.1109/IMTC.1997.610256.
- [121] Artursson, Tom, et al. "Drift Correction for Gas Sensors Using Multivariate Methods." *Journal of Chemometrics*, vol. 14, no. 5–6, Jan. 2000, pp. 711–723. EBSCOhost, doi:10.1002/1099-128X(200009/12)14:5/6<711::AID-CEM607>3.0.CO;2-4.
- [122] Grover, Abhishek, and Brejesh Lall. "A Novel Method for Removing Baseline Drifts in Multivariate Chemical Sensor." *IEEE Transactions on Instrumentation & Measurement*, vol. 69, no. 9, Sept. 2020, pp. 7306–7316. EBSCOhost, search.ebscohost.com/login.aspx?direct=true&db=edb&AN=145160007&site=eds-live.

- [123] hui, Ding & Jun-hua, Liu & Zhong-ru, Shen. (2003). Drift reduction of gas sensor by wavelet and principal component analysis. *Sensors and Actuators B-chemical - SENSOR ACTUATOR B-CHEM.* 96. 354-363. 10.1016/S0925-4005(03)00569-0.
- [124] T. C. Miller, S. D. Morgera, S. E. Sadow, A. Takshi and M. Palm, "Electronic Nose with Detection Method for Alcohol, Acetone, and Carbon Monoxide in Coronavirus Disease 2019 Breath Simulation Model," in *IEEE Sensors Journal*, pages 1-9, doi: 10.1109/JSEN.2021.3076102.
- [125] Miller, Tiffany C. "Brain-Computer Interface Based on Magnetic Particle Imaging For Diagnostic and Neurological Rehabilitation in Multiple Sclerosis." 2020 8th International Winter Conference on Brain-Computer Interface (BCI), Brain-Computer Interface (BCI), 2020 8th International Winter Conference On, Feb. 2020, pp. 1–6. EBSCOhost, doi:10.1109/BCI48061.2020.9061645.
- [126] B. D. Cox, Margaret J. Whichelow. Carbon Monoxide Levels in the Breath of Smokers and Nonsmokers: Effect of Domestic Heating Systems. *Journal of Epidemiology and Community Health* (1979-) [Internet]. 1985 [cited 2020 Nov 9];39(1):75. Available from: <http://search.ebscohost.com.ezproxy.lib.usf.edu/login.aspx?direct=true&db=edsjsr&AN=edsjsr.25566538&site=eds-live>
- [127] Laref, Rachid, et al. "Orthogonal Signal Correction to Improve Stability Regression Model in Gas Sensor Systems." *Journal of Sensors*, vol. 2017, Jan. 2017. EBSCOhost, doi:10.1155/2017/9851406.
- [128] D. Ahmadou, R. Laref, E. Losson and M. Siadat, "Reduction of drift impact in gas sensor response to improve quantitative odor analysis," 2017 IEEE International Conference on Industrial Technology (ICIT), 2017, pp. 928-933, doi: 10.1109/ICIT.2017.7915484.
- [128] S. Wold, Henrik Antti, Fredrik Lindgren, Jerker Öhman, "Orthogonal signal correction of near-infrared spectra", *Chemometrics and Intelligent Laboratory Systems*, Volume 44, Issues 1–2, 1998, Pages 175-185, ISSN 0169-7439, [https://doi.org/10.1016/S0169-7439\(98\)00109-9](https://doi.org/10.1016/S0169-7439(98)00109-9).
- [129] Jurs, P. C., et al. "Computational Methods for the Analysis of Chemical Sensor Array Data from Volatile Analytes." *CHEMICAL REVIEWS*, no. 7, 2000, p. 2649. EBSCOhost, search.ebscohost.com.ezproxy.lib.usf.edu/login.aspx?direct=true&db=edsbl&AN=RN082672023&site=eds-live.
- [130] Miguel Macías Macías, et al. "Improving Short Term Instability for Quantitative Analyses with Portable Electronic Noses." *Sensors*, vol. 14, no. 6, June 2014, pp. 10514–10526. EBSCOhost, doi:10.3390/s140610514.
- [131] Gallon, Victoria, et al. "Emissions of VOCs, SVOCs, and Mold during the Construction Process: Contribution to Indoor Air Quality and Future Occupants' Exposure." *Indoor Air*, vol. 30, no. 4, July 2020, p. 691. EBSCOhost, doi:10.1111/ina.12647.

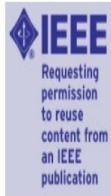
- [132] Ye, Wei, et al. "Indoor Air Pollutants, Ventilation Rate Determinants and Potential Control Strategies in Chinese Dwellings: A Literature Review." *Science of the Total Environment*, vol. 586, May 2017, pp. 696–729. EBSCOhost, doi:10.1016/j.scitotenv.2017.02.047.
- [133] Zhao, G., et al. "Volatile Organic Compounds Emitted by Filamentous Fungi Isolated from Flooded Homes after Hurricane Sandy Show Toxicity in a *Drosophila* Bioassay." *Indoor Air*, vol. 27, no. 3, May 2017, pp. 518–528. EBSCOhost, doi:10.1111/ina.12350.
- [134] Kalalian, Carmen, et al. "Influence of Indoor Chemistry on the Emission of MVOCs from *Aspergillus Niger* Molds." *Science of the Total Environment*, vol. 741, Nov. 2020. EBSCOhost, doi:10.1016/j.scitotenv.2020.140148.
- [135] Betancourt, Doris A., et al. "Microbial Volatile Organic Compound Emissions from *Stachybotrys Chartarum*growing on Gypsum Wallboard and Ceiling Tile." *BMC Microbiology*, vol. 13, no. 1, Dec. 2013. EBSCOhost, doi:10.1186/1471-2180-13-283.
- [136] Belizario, Jose E., et al. "Breath Biopsy and Discovery of Exclusive Volatile Organic Compounds for Diagnosis of Infectious Diseases." *Frontiers in Cellular and Infection Microbiology*, Jan. 2021. EBSCOhost, doi:10.3389/fcimb.2020.564194.
- [137] Traxler, Selina, et al. "VOC Breath Profile in Spontaneously Breathing Awake Swine during Influenza A Infection." *Scientific Reports*, vol. 8, no. 1, Oct. 2018, pp. 1–12. EBSCOhost, search.ebscohost.com.ezproxy.lib.usf.edu/login.aspx?direct=true&db=edb&AN=138760468&site=eds-live.
- [138] SALGIRLI DEMIRBAŞ, Yasemin, et al. "The Role of Bio-Detection Dogs in the Prevention and Diagnosis of Infectious Diseases: A Systematic Review." *Ankara Universitesi Veteriner Fakultesi Dergisi*, vol. 68, no. 2, Apr. 2021, pp. 185–192. EBSCOhost, search.ebscohost.com.ezproxy.lib.usf.edu/login.aspx?direct=true&db=edb&AN=149643189&site=eds-live.
- [139] Zeinab Abdelrahman, et al. "Comparative Review of SARS-CoV-2, SARS-CoV, MERS-CoV, and Influenza A Respiratory Viruses." *Frontiers in Immunology*, vol. 11, Sept. 2020. EBSCOhost, doi:10.3389/fimmu.2020.552909.
- [140] Lamote, Kevin, et al. "The Scent of COVID-19: Viral (Semi-)Volatiles as Fast Diagnostic Biomarkers?" *Journal of Breath Research*, vol. 14, no. 4, Oct. 2020, pp. 1–7. EBSCOhost, search.ebscohost.com.ezproxy.lib.usf.edu/login.aspx?direct=true&db=edb&AN=144763703&site=eds-live.
- [141] Elias Mansour, Rotem Vishinkin, Stephane Rihet, Walaa Saliba, Falk Fish, Patrice Sarfati, Hossam Haick. "Measurement of temperature and relative humidity in exhaled breath." *Science Direct, Sensors and Actuators B: Chemical*, vol. 304, 2020.

- [142] Fenske JD, Paulson SE. Human Breath Emissions of VOCs. JOURNAL- AIR AND WASTE MANAGEMENT ASSOCIATION [Internet]. 1999 [cited 2020 Nov 9];(5):594. Available from: <http://search.ebscohost.com.ezproxy.lib.usf.edu/login.aspx?direct=true&db=edsbl&AN=RN061130263&site=eds-live>
- [143] Alisa Rudnitskaya. "Calibration Update and Drift Correction for Electronic Noses and Tongues." *Frontiers in Chemistry*, vol. 6, Sept. 2018. *EBSCOhost*, doi:10.3389/fchem.2018.00433.
- [144] Kanji, Jamil N., et al. "False Negative Rate of COVID-19 PCR Testing: A Discordant Testing Analysis." *Virology Journal*, vol. 18, no. 1, Jan. 2021, pp. 1–6. *EBSCOhost*, doi:10.1186/s12985-021-01489-0.
- [145] Wintjens AGWE, Hintzen KFH, Engelen SME, Lubbers T, Savelkoul PHM, Wesseling G, van der Palen JAM, Bouvy ND. Applying the electronic nose for pre-operative SARS-CoV-2 screening. *Surg Endosc*. 2020 Dec 2:1–8. doi: 10.1007/s00464-020-08169-0. Epub ahead of print. PMID: 33269428; PMCID: PMC7709806.
- [145] Grassin-Delyle, Stanislas, et al. "Metabolomics of Exhaled Breath in Critically Ill COVID-19 Patients: A Pilot Study." *EBioMedicine*, vol. 63, Jan. 2021. *EBSCOhost*, doi:10.1016/j.ebiom.2020.103154.
- [146] Giovannini G, Haick H, Garoli D. Detecting COVID-19 from Breath: A Game Changer for a Big Challenge. *ACS Sens*. 2021 Apr 23;6(4):1408-1417. doi: 10.1021/acssensors.1c00312. Epub 2021 Apr 7. PMID: 33825440; PMCID: PMC8043202.
- [147] Licht JC, Grasemann H. Potential of the Electronic Nose for the Detection of Respiratory Diseases with and without Infection. *Int J Mol Sci*. 2020 Dec 10;21(24):9416. doi: 10.3390/ijms21249416. PMID: 33321951; PMCID: PMC7763696.
- [148] Dragonieri S, Pennazza G, Carratu P, Resta O. Electronic Nose Technology in Respiratory Diseases. *Lung*. 2017 Apr;195(2):157-165. doi: 10.1007/s00408-017-9987-3. Epub 2017 Feb 25. PMID: 28238110.
- [149] Farraia MV, Cavaleiro Rufo J, Paciência I, Mendes F, Delgado L, Moreira A. The electronic nose technology in clinical diagnosis: A systematic review. *Porto Biomed J*. 2019 Jul 22;4(4):e42. doi: 10.1097/j.pbj.0000000000000042. PMID: 31930178; PMCID: PMC6924976.
- [150] Dragonieri S, Schot R, Mertens BJ, Le Cessie S, Gauw SA, Spanevello A, Resta O, Willard NP, Vink TJ, Rabe KF, Bel EH, Sterk PJ. An electronic nose in the discrimination of patients with asthma and controls. *J Allergy Clin Immunol*. 2007 Oct;120(4):856-62. doi: 10.1016/j.jaci.2007.05.043. Epub 2007 Jul 20. PMID: 17658592.
- [151] Tenero L, Sandri M, Piazza M, Paiola G, Zaffanello M, Piacentini G. Electronic nose in discrimination of children with uncontrolled asthma. *J Breath Res*. 2020 Jul 21;14(4):046003. doi: 10.1088/1752-7163/ab9ab0. PMID: 32512553.

- [152] Bossuyt PM, Reitsma JB, Bruns DE, Gatsonis CA, Glasziou PP, Irwig L, Lijmer JG, Moher D, Rennie D, de Vet HC, Kressel HY, Rifai N, Golub RM, Altman DG, Hooft L, Korevaar DA, Cohen JF; STARD Group. STARD 2015: an updated list of essential items for reporting diagnostic accuracy studies. *BMJ*. 2015 Oct 28;351:h5527. doi: 10.1136/bmj.h5527. PMID: 26511519; PMCID: PMC4623764.
- [153] Moons KG, Altman DG, Reitsma JB, Ioannidis JP, Macaskill P, Steyerberg EW, Vickers AJ, Ransohoff DF, Collins GS. Transparent Reporting of a multivariable prediction model for Individual Prognosis or Diagnosis (TRIPOD): explanation and elaboration. *Ann Intern Med*. 2015 Jan 6;162(1):W1-73. doi: 10.7326/M14-0698. PMID: 25560730.
- [154] Miller TC, Morgera SD, Sadow SE, Takshi A, Mullarkey M, Palm M. Neurological connections and endogenous biochemistry - potentially useful in electronic-nose diagnostics for coronavirus diseases. *Neuroimmunol Neuroinflammation* 2021;8:[Accept]. <http://dx.doi.org/10.20517/2347-8659.2021.05>

Appendix A: Copyright Permissions

The following notice is for the use of Figures 3.2, 3.11 (a), (b), and (c), 3.12 (a) and (b), 3.13 and Table 3.1, and material in Chapter 3 referring to reference [124].



Requesting permission to reuse content from an IEEE publication

Electronic Nose with Detection Method for Alcohol, Acetone, and Carbon Monoxide in Coronavirus Disease 2019 Breath Simulation Model

Author: [::Tiffany::] C. [::Miller::]; Salvatore D. Morgera; Stephen E. Saddow; Arash Takshi; Matthew Palm

Publication: IEEE Sensors Journal

Publisher: IEEE

Date: Apr 27, 2021

Copyright © 2021, IEEE

Thesis / Dissertation Reuse

The IEEE does not require individuals working on a thesis to obtain a formal reuse license, however, you may print out this statement to be used as a permission grant:

Requirements to be followed when using any portion (e.g., figure, graph, table, or textual material) of an IEEE copyrighted paper in a thesis:

- 1) In the case of textual material (e.g., using short quotes or referring to the work within these papers) users must give full credit to the original source (author, paper, publication) followed by the IEEE copyright line © 2011 IEEE.
- 2) In the case of illustrations or tabular material, we require that the copyright line © [Year of original publication] IEEE appear prominently with each reprinted figure and/or table.
- 3) If a substantial portion of the original paper is to be used, and if you are not the senior author, also obtain the senior author's approval.

Requirements to be followed when using an entire IEEE copyrighted paper in a thesis:

- 1) The following IEEE copyright/ credit notice should be placed prominently in the references: © [year of original publication] IEEE. Reprinted, with permission, from [author names, paper title, IEEE publication title, and month/year of publication]
- 2) Only the accepted version of an IEEE copyrighted paper can be used when posting the paper or your thesis on-line.
- 3) In placing the thesis on the author's university website, please display the following message in a prominent place on the website: In reference to IEEE copyrighted material which is used with permission in this thesis, the IEEE does not endorse any of [university/educational entity's name goes here]'s products or services. Internal or personal use of this material is permitted. If interested in reprinting/republishing IEEE copyrighted material for advertising or promotional purposes or for creating new collective works for resale or redistribution, please go to http://www.ieee.org/publications_standards/publications/rights/rights_link.html to learn how to obtain a License from RightsLink.

If applicable, University Microfilms and/or ProQuest Library, or the Archives of Canada may supply single copies of the dissertation.

BACK

CLOSE WINDOW

The following notice is for material in Chapter 2 referring to reference [125].



Brain-Computer Interface Based on Magnetic Particle Imaging For Diagnostic and Neurological Rehabilitation in Multiple Sclerosis

Conference Proceedings: 2020 8th International Winter Conference on Brain-Computer Interface (BCI)

Author: [::Tiffany::] C. [::Miller::]

Publisher: IEEE

Date: 26-28 Feb. 2020

Copyright © 2020, IEEE

Thesis / Dissertation Reuse

The IEEE does not require individuals working on a thesis to obtain a formal reuse license, however, you may print out this statement to be used as a permission grant:

Requirements to be followed when using any portion (e.g., figure, graph, table, or textual material) of an IEEE copyrighted paper in a thesis:

- 1) In the case of textual material (e.g., using short quotes or referring to the work within these papers) users must give full credit to the original source (author, paper, publication) followed by the IEEE copyright line © 2011 IEEE.
- 2) In the case of illustrations or tabular material, we require that the copyright line © [Year of original publication] IEEE appear prominently with each reprinted figure and/or table.
- 3) If a substantial portion of the original paper is to be used, and if you are not the senior author, also obtain the senior author's approval.

Requirements to be followed when using an entire IEEE copyrighted paper in a thesis:

- 1) The following IEEE copyright/ credit notice should be placed prominently in the references: © [year of original publication] IEEE. Reprinted, with permission, from [author names, paper title, IEEE publication title, and month/year of publication]
- 2) Only the accepted version of an IEEE copyrighted paper can be used when posting the paper or your thesis on-line.
- 3) In placing the thesis on the author's university website, please display the following message in a prominent place on the website: In reference to IEEE copyrighted material which is used with permission in this thesis, the IEEE does not endorse any of [university/educational entity's name goes here]'s products or services. Internal or personal use of this material is permitted. If interested in reprinting/republishing IEEE copyrighted material for advertising or promotional purposes or for creating new collective works for resale or redistribution, please go to http://www.ieee.org/publications_standards/publications/rights/rights_link.html to learn how to obtain a License from RightsLink.

If applicable, University Microfilms and/or ProQuest Library, or the Archives of Canada may supply single copies of the dissertation.

BACK

CLOSE WINDOW

The following notice is for material in Chapters 4 and 5 referring to reference [127].

Copyright

Copyright © 2017 Rachid Laref et al. This is an open access article distributed under the [Creative Commons Attribution License](#), which permits unrestricted use, distribution, and reproduction in any medium, provided the original work is properly cited.

The following notice is for the use of Table 6.1 and material referring to reference [136].

Keywords: breath biopsy, infectious disease, microbiomes, metabolomics, biomarkers

Citation: Belizário JE, Faintuch J and Malpartida MG (2021) Breath Biopsy and Discovery of Exclusive Volatile Organic Compounds for Diagnosis of Infectious Diseases. *Front. Cell. Infect. Microbiol.* 10:564194. doi: 10.3389/fcimb.2020.564194

Received: 20 May 2020; **Accepted:** 16 November 2020;

Published: 07 January 2021.

Edited by:

Tao Lin, Baylor College of Medicine, United States

Reviewed by:

Eduard Monso, Parc Taulí Foundation, Spain

Brett Anthony McGregor, University of North Dakota, United States

Copyright © 2021 Belizário, Faintuch and Malpartida. This is an open-access article distributed under the terms of the [Creative Commons Attribution License \(CC BY\)](#). The use, distribution or reproduction in other forums is permitted, provided the original author(s) and the copyright owner(s) are credited and that the original publication in this journal is cited, in accordance with accepted academic practice. No use, distribution or reproduction is permitted which does not comply with these terms.

***Correspondence:** José E. Belizário, jebeliza@usp.br

The following notice is for material presented in Chapters 4 and 5 referring to reference [143].

Keywords: calibration update, calibration transfer, drift correction, electronic nose, electronic tongue

Citation: Rudnitskaya A (2018) Calibration Update and Drift Correction for Electronic Noses and Tongues. *Front. Chem.* 6:433. doi: 10.3389/fchem.2018.00433

Received: 16 March 2018; **Accepted:** 31 August 2018;

Published: 25 September 2018.

Edited by:

Dmitry Kirsanov, Saint Petersburg State University, Russia

Reviewed by:

Santiago Marco, University of Barcelona, Spain

Carmen Horrillo, Consejo Superior de Investigaciones Científicas (CSIC), Spain

Copyright © 2018 Rudnitskaya. This is an open-access article distributed under the terms of the [Creative Commons Attribution License \(CC BY\)](#). The use, distribution or reproduction in other forums is permitted, provided the original author(s) and the copyright owner(s) are credited and that the original publication in this journal is cited, in accordance with accepted academic practice. No use, distribution or reproduction is permitted which does not comply with these terms.

***Correspondence:** Alisa Rudnitskaya, alisa@ua.pt

The following notice is for material in Chapters 4 and 5 referring to reference [154].



www.oaepublish.com

LICENSE TO PUBLISH

Article title:

Article number:

Corresponding author:

Journal title: *Neuroimmunology and Neuroinflammation*

This is a license agreement under which you, the author, assign copyright in your article to OAE Publishing Inc. to allow us to publish your article, including abstract, tables, figures, data, and supplemental materials hosted by us, for the full period of copyright throughout the world, in all languages, in all forms and all media (whether known at this time or developed at any time in the future), subject to the terms and conditions below.

Please read this agreement carefully, complete it, and then return a copy to us by e-mail: nn_editor001@nnjournal.net.

License

OAE Publishing Inc. will apply the CC-BY License [Creative Commons Attribution 4.0 International License (<https://creativecommons.org/licenses/by/4.0/>)], which permits the author(s) to copy and redistribute the material in any medium or format, or to remix, transform, and build upon the material for any purpose, even commercially, provided that the user(s) appropriately acknowledge the original author(s) and the source.

Assignment of Publishing Rights

I hereby assign to OAE Publishing Inc. the following rights to the article, including any supplemental material, and any parts, extracts, or derivative works thereof:

1. the right to carry out a peer-review of the submitted article;
2. the right to make necessary and suitable editorial changes to the accepted article;
3. the right to reproduce and distribute the published article in all forms and all media, including print-on-demand;
4. the right to produce reprints, offprints, and special editions of the published article;
5. the right to translate the published article into all other languages;
6. the right to reproduce and distribute the published article by using such photomechanical or similar means as photocopy;
7. the right to deposit the published article into any designated institutional repository;

Rights of Authors

Authors retain the following rights:

1. copyright, and other proprietary rights relating to the article, such as patent rights;
2. the right to use all or part of the article in their own works, including lectures and books;
3. the right to reproduce the article for internal use, provided that the copies are not for sale;

4. the right to present the article at a meeting/conference;
5. the right to self-archive the article;
6. Author(s) grant any third party the right to use the article freely as long as its integrity is maintained and its original authors, citation details and publisher are identified.

Author Warranties

1. All persons who have a reasonable claim to authorship are named in the article as co-authors, including yourself, and you have not fabricated or misappropriated anyone's identity, including your own;
2. You have been authorized by all such co-authors to sign this agreement as an agent on their behalf, and to agree on their behalf the priority of the assertion of copyright and the order of names in the publication of your article;
3. The article is your original work, apart from any permitted third-party copyright material you include, and does not infringe any intellectual property rights of any other person or entity and cannot be construed as plagiarizing any other published work, including your own published work;
4. Your submitted article is not currently under submission to, nor is it under consideration by, nor has it been accepted by any other journal or publication, nor has it been previously published by any other journal or publication, nor has it been assigned or licensed by you to any third party;
5. You have obtained the necessary written permission to include material in your article that is owned and held in copyright by a third party, which shall include but is not limited to any proprietary text, illustration, table, or other material, including data, audio, video, film stills, screenshots, musical notation, and any supplemental material;
6. You have read and agree to comply with all our policies on publishing ethics and those in the Author Instructions.

Appendix B: MQ and LED Arduino Uno Source Code

The following source code is for material presented in Chapter 3.1.2.2.

```
// Modified on May 09, 2020 by Tiffany C. Miller//
//this code is based on source code from sandboxelectronics.com, sunfounder.com, and
lastminuteengineers.com//

/*****Hardware Related
Macros*****/
#define MQ2_PIN (0) //define which analog input channel you are going to
use, A0 for Alcohol and CO
#define MQ135_PIN (1) //A1 for acetone
#define SGX4N0250_PIN (3) //define A3 input channel for NO
#define RL_VALUE (10) //define the load resistance on the board, in kilo
ohms
#define RO_CLEAN_AIR_FACTOR (9.83) //RO_CLEAR_AIR_FACTOR=(Sensor
resistance in clean air)/RO,
//which is derived from the chart in datasheet

#define GAS_H2 (1)
#define GAS_CO (2)
#define GAS_Alcohol (3)
#define GAS_Acetone (4)
#define GAS_NO (5)

/*****Globals*****/
*****/
float H2Curve[3] = {2.300,0.040,-0.300}; //two points are taken from the curve.
//with these two points, a line is formed which is "approximately
equivalent"
//to the original curve. Take log of each point 1: (lg200, lg
1.1)=(2.3,0.04) and point 2: (lg10000,lg .34)=(4,-0.47)
//find the slope using these points. take point1 as reference
//data format: { x, y, slope}; point1: (lg200, 0.04), point2:
(lg10000, -0.47)
float COCurve[3] = {2.300,0.720,-0.340}; //two reference points of smaller reference
point are taken from the curve.
```

```

//with these two points, a line is formed which is "approximately
equivalent"
//to the original curve.
//data format:{ x, y, slope}; point1: (lg200, lg5.1)=( 2.3, .708),
point2: (lg10000, lg 1.6)=( 4, 0.204)
float AlcoholCurve[3] = {2.300,0.710,-0.373}; //two points are taken from the curve.
//with these two points, a line is formed which is "approximately
equivalent"
//to the original curve.
//data format:{ x, y, slope}; point1: (lg200, lg 2.8)= (2.3, 0.447),
point2: (lg10000,lg 0.65)=( 4, -.187)
float AcetoneCurve[3] = {1.6989, -0.481,-1.345}; //two points are taken from the curve.
//with these two points, a line is formed which is "approximately
equivalent"
//to the original curve.
//data format:{ x, y, slope}; point1: (lg50, lg 0.33)= (1.6989, -
0.481), point2: (lg100,lg 0.13) = (2, -0.886)
float Ro = 10; //Ro is initialized to 10 kilo ohms

void setup()
{
  Serial.begin(9600); //UART setup, baudrate = 9600bps
  while (!Serial); // time to get serial running
  Serial.println(F("BME280 test"));

  unsigned status;

  status = bme.begin(0X76);
  Serial.println("-- Default Test --");
  delayTime = 2000;

  Serial.println();

  Serial.print("Calibrating...\n");
  Ro = MQCalibration(MQ2_PIN); //Calibrating the sensor. Please make sure the
sensor is in clean air
  //
  Serial.print("Calibration is done...\n");
  Serial.print("Ro=");
  Serial.print(Ro);
  Serial.print("kohm");
  Serial.print("\n");
  pinMode(2,OUTPUT); //GREEN LED FOR ALCOHOL
  pinMode(3,OUTPUT); //YELLOW LED FOR ACETONE
  pinMode(4,OUTPUT); //RED LED FOR CO

```

```

pinMode(5,OUTPUT); //BLUE LED FOR H2
pinMode(6,OUTPUT); //WHITE LED FOR NO

}
void loop()
{

Serial.print("CO:");
Serial.print(MQGetGasPercentage(MQRead(MQ2_PIN)/Ro,GAS_CO));
Serial.print( "ppm" );
Serial.print("  ");
if (MQGetGasPercentage(MQRead(MQ2_PIN)/Ro,GAS_CO) > 100)
  Serial.print(" | COVID-19!");
if (MQGetGasPercentage(MQRead(MQ2_PIN)/Ro,GAS_CO) > 100)
  digitalWrite(4, HIGH);
  Serial.print("  ");
if (MQGetGasPercentage(MQRead(MQ2_PIN)/Ro,GAS_CO) < 100)
  Serial.print(" | HEALTHY");
if (MQGetGasPercentage(MQRead(MQ2_PIN)/Ro,GAS_CO) < 100)
  digitalWrite(4, LOW);
  Serial.print("  ");

Serial.print("Alcohol:");
Serial.print(MQGetGasPercentage(MQRead(MQ2_PIN)/Ro,GAS_Alcohol) );
Serial.print( "ppm" );
Serial.print("  ");
if (MQGetGasPercentage(MQRead(MQ2_PIN)/Ro,GAS_Alcohol) < 0.4)
  Serial.print(" | COVID-19!");
  if (MQGetGasPercentage(MQRead(MQ2_PIN)/Ro,GAS_Alcohol) < 0.4)
    digitalWrite(2, LOW);
    Serial.print("  ");
if (MQGetGasPercentage(MQRead(MQ2_PIN)/Ro,GAS_Alcohol) > 0.4)
  Serial.print(" | HEALTHY");
  if (MQGetGasPercentage(MQRead(MQ2_PIN)/Ro,GAS_Alcohol) > 0.4)
    digitalWrite(2, HIGH);
    Serial.print("  ");

Serial.print("Acetone:");
Serial.print(MQGetGasPercentage(MQRead(MQ135_PIN)/Ro,GAS_Acetone) );
Serial.print("ppm" );
Serial.print("  ");
if (MQGetGasPercentage(MQRead(MQ135_PIN)/Ro,GAS_Acetone) > 1.69)
  Serial.print(" | COVID-19!");
if (MQGetGasPercentage(MQRead(MQ135_PIN)/Ro,GAS_Acetone) >1.69)
  digitalWrite(3, HIGH);

```

```

    Serial.print(" ");
    if (MQGetGasPercentage(MQRead(MQ135_PIN)/Ro,GAS_Acetone) < 1.69)
        Serial.print(" | HEALTHY");
    if (MQGetGasPercentage(MQRead(MQ135_PIN)/Ro,GAS_Acetone) < 1.69)
        digitalWrite(3, LOW);
        Serial.print(" ");

    Serial.print("\n");
    delay(200);

    Serial.print("Temperature = ");
    Serial.print(((bme.readTemperature() * 1.8) + 32));
    if (((bme.readTemperature() * 1.8) + 32) > 101)
        digitalWrite(5, HIGH);
        Serial.print(" ");
    if (((bme.readTemperature() * 1.8) + 32) < 101)
        digitalWrite(5, LOW);
        Serial.print(" ");
    Serial.println("°F");

    Serial.print("Pressure = ");

    Serial.print(bme.readPressure() / 100.0F);
    Serial.println(" hPa");

    Serial.print("Humidity = ");
    Serial.print(bme.readHumidity());
    Serial.println(" %");
    Serial.println();

float sensorMQ2_volt;
float sensorMQ2Value;

    sensorMQ2Value = analogRead(A0);
    sensorMQ2_volt = sensorMQ2Value/1024*5.0;

    Serial.print("sensorMQ2_volt = ");
    Serial.print(sensorMQ2_volt);
    Serial.println("V");
    delay(1000);

float sensorSGX4NO250_volt;
float sensorSGX4NO250Value;

    sensorSGX4NO250Value = analogRead(A3);

```

```

sensorSGX4NO250_volt = sensorSGX4NO250Value/1024*5.0;

Serial.print("sensorSGX4NO250_volt = ");
Serial.print(sensorSGX4NO250_volt);
Serial.println("V");
if (sensorSGX4NO250_volt > 0.37)
  Serial.println("! COVID-19!");
if (sensorSGX4NO250_volt > 0.37)
digitalWrite(6, HIGH);
if (sensorSGX4NO250_volt < 0.37)
Serial.print(" | HEALTHY");
if (sensorSGX4NO250_volt < 0.37)
digitalWrite(6, LOW);
delay(1000);

float sensorMQ135_volt;
float sensorMQ135Value;

sensorMQ135Value = analogRead(A1);
sensorMQ135_volt = sensorMQ2Value/1024*5.0;

Serial.print("sensorMQ135_volt = ");
Serial.print(sensorMQ135_volt);
Serial.println("V");
delay(1000);

}

float MQResistanceCalculation(int raw_adc)
{
  return ( ((float)RL_VALUE*(1023-raw_adc)/raw_adc));
}
float MQCalibration(int mq_pin)
{
  int i;
  float val=0;

  for (i=0;i<CALIBARAION_SAMPLE_TIMES;i++) {          //take multiple samples
    val += MQResistanceCalculation(analogRead(mq_pin));
    delay(CALIBRATION_SAMPLE_INTERVAL);
  }
  val = val/CALIBARAION_SAMPLE_TIMES;                //calculate the average value

  val = val/RO_CLEAN_AIR_FACTOR;                      //divided by
  RO_CLEAN_AIR_FACTOR yields the Ro

```

//according to the chart in the datasheet

```
return val;
}
Input: mq_pin - analog channel
float MQRead(int mq_pin)
{
    int i;
    float rs=0;

    for (i=0;i<READ_SAMPLE_TIMES;i++) {
        rs += MQResistanceCalculation(analogRead(mq_pin));
        delay(READ_SAMPLE_INTERVAL);
    }

    rs = rs/READ_SAMPLE_TIMES;

    return rs;
}
int MQGetGasPercentage(float rs_ro_ratio, int gas_id)
{
    if ( gas_id == GAS_H2 ) {
        return MQGetPercentage(rs_ro_ratio,H2Curve);
    } else if ( gas_id == GAS_CO ) {
        return MQGetPercentage(rs_ro_ratio,COCurve);
    } else if ( gas_id == GAS_Alcohol ) {
        return MQGetPercentage(rs_ro_ratio,AlcoholCurve);
    } else if ( gas_id == GAS_Acetone ) {
        return MQGetPercentage(rs_ro_ratio,AcetoneCurve);
    }

    return 0;
}
float MQGetPercentage(float rs_ro_ratio, float *pcurve)
{
    return (pow(10,(((log10(rs_ro_ratio)-pcurve[1])/pcurve[2]) + pcurve[0])));
}
```


Appendix C: BMW280 Arduino Uno Source Code

The following source code is for material presented in Chapter 3.1.2.2.

```
/******  
// Modified on Nov. 21, 2020 by Tiffany C. Miller//  
//this code is based on source code for the BME280 humidity, temperature & pressure sensor  
designed specifically to work with the Adafruit BME280 Breakout at  
http://www.adafruit.com/products/2650
```

These sensors use I2C or SPI to communicate, 2 or 4 pins are required to interface. The device's I2C address is either 0x76 or 0x77.

Adafruit invests time and resources providing this open source code, please support Adafruit and open-source hardware by purchasing products from Adafruit!

Written by Limor Fried & Kevin Townsend for Adafruit Industries.
BSD license, all text above must be included in any redistribution
See the LICENSE file for details.

```
*****/
```

```
#include <Wire.h>  
#include <SPI.h>  
#include <Adafruit_Sensor.h>  
#include <Adafruit_BME280.h>
```

```
#define BME_SCL 13  
#define BME_MISO 12  
#define BME_MOSI 11  
#define BME_CS 10
```

```
#define SEALEVELPRESSURE_HPA (1013.25)
```

```
Adafruit_BME280 bme; // I2C  
//Adafruit_BME280 bme(BME_CS); // hardware SPI  
//Adafruit_BME280 bme(BME_CS, BME_MOSI, BME_MISO, BME_SCK); // software SPI
```

```
unsigned long delayTime;
```

```

void setup() {
  Serial.begin(9600);
  while (!Serial); // time to get serial running
  Serial.println(F("BME280 test"));

  unsigned status;

  // default settings
  status = bme.begin(0X76);
  // You can also pass in a Wire library object like &Wire2
  // status = bme.begin(0x77, &Wire2)
  if (!status) {
    Serial.println("Could not find a valid BME280 sensor, check wiring, address, sensor ID!");
    Serial.print("SensorID was: 0x"); Serial.println(bme.sensorID(), 16);
    Serial.print("    ID of 0xFF probably means a bad address, a BMP 180 or BMP 085\n");
    Serial.print("    ID of 0x56-0x58 represents a BMP 280,\n");
    Serial.print("    ID of 0x60 represents a BME 280.\n");
    Serial.print("    ID of 0x61 represents a BME 680.\n");
    while (1) delay(10);
  }

  Serial.println("-- Default Test --");
  delayTime = 2000;
  Serial.println();
}

void loop() {
  printValues();
  delay(delayTime);
}

void printValues() {
  Serial.print("Temperature = ");
  Serial.print(((bme.readTemperature() * 1.8) + 32));
  if (((bme.readTemperature() * 1.8) + 32) > 90)
    digitalWrite(5, HIGH);
  Serial.print("  ");
  if (((bme.readTemperature() * 1.8) + 32) < 90)
    digitalWrite(5, LOW);
  Serial.print("  ");
  Serial.println("°F");

  Serial.print("Pressure = ");
  Serial.print(bme.readPressure() / 100.0F);
}


```

```
Serial.println(" hPa");

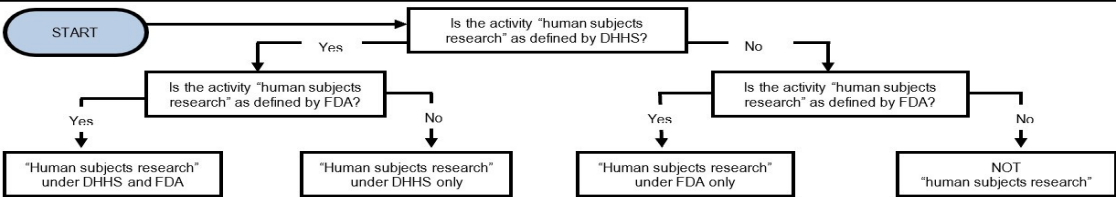
Serial.print("Humidity = ");
Serial.print((bme.readHumidity()+10));
Serial.println(" %");
Serial.println();}
```

Appendix D: HRP-310 – Worksheet for Human Subjects Research Determination

The following HRP-310 – WORKSHEET for Human Subjects Research Determination shows that Institutional Review Board (IRB) approval was not required for this Dissertation research.

	WORKSHEET: Human Subjects Research	
	NUMBER	DATE
	HRP-310	5/1/2020
PAGE 1 of 3		

The purpose of this worksheet is to provide support for individuals in determining whether an activity is human subjects research or how it is regulated. This worksheet is to be used. It does not need to be completed or retained.



1 Research as Defined by DHHS Regulations¹ (Check if "Yes".)

<input checked="" type="checkbox"/>	Is the activity an investigation? (Investigation: A searching inquiry for facts; detailed or careful examination.)
<input checked="" type="checkbox"/>	Is the investigation systematic? (Systematic: Having or involving a system, method, or plan.)
<input checked="" type="checkbox"/>	Is the systematic investigation designed to develop or contribute to knowledge? (Designed: observable behaviors used to develop or contribute to knowledge. Develop: to form the basis for a future contribution. Contribute: to result in. Knowledge: truths, facts, information.)
<input checked="" type="checkbox"/>	Is the knowledge the systematic investigation is designed to develop or contribute generalizable? (Generalizable: Universally or widely applicable.)

2 Human Subject Under DHHS Regulations (Check if "Yes".)

<input type="checkbox"/>	Is the Investigator conducting the research gathering information or biospecimens <i>about living</i> individuals?
--------------------------	--

3 Human Subject Under DHHS Regulations (Check if "Yes".)

<input type="checkbox"/>	Will the Investigator use, study, or analyze information or biospecimens obtained through either of the following mechanisms? Specify which mechanism(s) apply, if yes: <input type="checkbox"/> Physical procedures or manipulations of those individuals or their environment for research purposes ("intervention"). <input type="checkbox"/> Communication or interpersonal contact with the individuals ("interaction").
--------------------------	---

4 Human Subject Under DHHS Regulations (Check if "Yes")

<input type="checkbox"/>	Will the Investigator gather data that is either (Specify which category(s) apply(<i>ies</i>) if <i>yes</i>): <input type="checkbox"/> The data are about behavior that occurs in a context in which an individual can reasonably expect that no observation or recording is taking place (i.e. "private information"). <input type="checkbox"/> Individuals have provided the data for specific purposes in which the individuals can reasonably expect that it will NOT be made public, such as a medical record (i.e. "private information").
<input type="checkbox"/>	Can the individuals' identities be readily ascertained or associated with the information by the Investigator (i.e. "identifiable information")?
<input type="checkbox"/>	Can the individuals' identities be readily ascertained or associated with the biospecimens (i.e. "identifiable biospecimen")?

If all items are checked under 1, 2, and 3 or 1, 2, and 4, the activity is human subjects research under DHHS regulations.

5 Human Subjects Research Under DHHS Regulations (Check if "Yes")

<input type="checkbox"/>	Has a department or agency head, covered by the Common Rule, retained final judgment (consistent with the ethical principles of the Belmont Report) that the activity is human subjects research under DHHS regulations?
--------------------------	--

If checked, the activity is human subjects research under DHHS regulations.

WORKSHEET: Human Subjects Research		
NUMBER	DATE	PAGE
HRP-310	5/1/2020	2 of 3

6 Human Research Under FDA Regulations (Check if “Yes”)	
<input type="checkbox"/>	Does the activity involve any of the following? (Check all that apply)
<input type="checkbox"/>	In the United States: The use of a drug ⁱⁱ in one or more persons other than use of an approved drug in the course of medical practice ⁱⁱⁱ .
<input type="checkbox"/>	In the United States: The use of a device ^{iv} in one or more persons that evaluates the safety or effectiveness of that device.
<input type="checkbox"/>	Data regarding subjects or control subjects submitted to or held for inspection by FDA ^v .
<input type="checkbox"/>	Data regarding the use of a device on human specimens (identified or unidentified) submitted to or held for inspection by FDA ^{vi} .
If “Yes”, the activity is human subjects research under FDA regulations.	
If the activity is human subjects research under DHHS regulations or under FDA regulations, it is human subjects research under organizational policy.	
7 Engagement (Complete if the activity is human subjects research. (Check if “Yes”)	
<input type="checkbox"/>	The organization is engaged in human <u>subjects</u> research. Use HRP-311 - WORKSHEET - Engagement.
Comments: <div style="background-color: #cccccc; height: 20px; width: 100%;"></div>	

ⁱ The following activities conducted or supported by the Department of Defense (DOD) are NOT research involving human subjects: Activities carried out solely for purposes of diagnosis, treatment, or prevention of injury and disease in Service members and other mission essential personnel under force health protection programs of the Department of Defense, including health surveillance pursuant to section 1074f of Reference (g) and the use of medical products consistent with DoD Instruction 6200.02. Authorized health and medical activities as part of the reasonable practice of medicine or other health professions undertaken for the sole purpose of patient treatment. Activities performed for the sole purpose of medical quality assurance consistent with 10 USC 1102 and DoDD 6025.13. Activities performed solely for an OT&E project where the activities and project meet the definition of OT&E as defined in 10 USC 139(a)(2)(A). Activities performed solely for assessing compliance of individuals and organizations with requirements applicable to military, civilian, or contractor personnel or to organizational units, including such activities as occupational drug testing, occupational health and safety reviews, network monitoring, and monitoring for compliance with requirements for protection of classified information. Activities, including program evaluation, customer satisfaction surveys, user surveys, outcome reviews, and other methods, designed solely to assess the performance of DoD programs where the results of the evaluation are only for the use of Government officials responsible for the operation or oversight of the program being evaluated and are not intended for generalized use beyond such program. Survey, interview, or surveillance activities and related analyses performed solely for authorized foreign intelligence collection purposes, as authorized by DoDD 5240.01.

ⁱⁱ The term “drug” means:

- (A) articles recognized in the official United States Pharmacopoeia, official Homoeopathic Pharmacopoeia of the United States, or official National Formulary, or any supplement to any of them; and
- (B) articles intended for use in the diagnosis, cure, mitigation, treatment, or prevention of disease in man or other animals; and
- (C) articles (other than food and dietary supplements) intended to affect the structure or any function of the body of man or other animals; and
- (D) articles intended for use as a component of any article specified in clause (A), (B), or (C).

ⁱⁱⁱ “Other than the use of an approved drug in the course of medical practice” refers to a practitioner providing an approved drug to a patient because the practitioner believes the drug to be in the best interests of the patient. If the protocol specifies the use of the drug, it is not in the course of medical practice unless use of the drug is completely up to the discretion of the practitioner.

^{iv} The term “device” means an instrument, apparatus, implement, machine, contrivance, implant, in vitro reagent, or other similar or related article, including any component, part, or accessory, which is:

WORKSHEET: Human Subjects Research		
NUMBER	DATE	PAGE
HRP-310	5/1/2020	3 of 3

-
- (1) recognized in the official National Formulary, or the United States Pharmacopeia, or any supplement to them,
 - (2) intended for use in the diagnosis of disease or other conditions, or in the cure, mitigation, treatment, or prevention of disease, in man or other animals, or
 - (3) intended to affect the structure or any function of the body of man or other animals, and which does not achieve its primary intended purposes through chemical action within or on the body of man or other animals and which is not dependent upon being metabolized for the achievement of its primary intended purposes.
- ^v This is specific to submissions that are part of an application for a research or marketing permit. However, unless otherwise indicated, assume all submissions to FDA meet this requirement.
- ^{vi} This is specific to submissions that are part of an application for a research or marketing permit. However, unless otherwise indicated, assume all submissions to FDA meet this requirement.

Appendix E: Glossary of Terms

Acute Demyelinating Encephalomyelitis (ADEM)

Acute Respiratory Distress Syndrome (ARDS)

Acute Lung Injury (ALI)

Amperometric Electrochemical (AEC)

Analog to Digital Conversion (ADC)

Angiotensin-Converting Enzyme 2 (ACE2)

Area Under Curve (AUC)

Artificial Neural Network (ANN)

Blood-Brain Barrier (BBB)

Biosafety Level (BSL)

Central Nervous System (CNS)

Chronic Obstructive Pulmonary Disease (COPD)

Computerized Tomography (CT)

Corona Virus Disease 2019 (COVID-19)

Cross-Validation Value (CVV)

Chronic Rhinosinusitis (CRS)

Cyclic Adenosine Monophosphate (cAMP)

Cyclic Nucleotide-Gated (CNG)

Dexamethasone (dex)

Discrete Wavelet Transform (DWT)

Electrobulbogram (EBG)

Electronic Nose (eNose)

Emergency Use Authorization (EUA)

Envelope (E)

Exhaled Breath Condensate (EBD)

False-Negative (FN)

False Negative Rates (FNRs)

Femtogram Per Milliliter (fg/mL)

Field Effect Transistor (FET)

First C-Terminal Domain (CTD1)

Fluid-Attenuated Inversion Recovery (FLAIR)

Fourier Bandpass Filter (FBF)

Gas Chromatography (GC)

Guillain-Barre Syndrome (GBS)

Interleukin (IL)

Internal Control Reagent (ICR)

Ion Mobility Spectrometry (IMS)

Jet Propulsion Laboratory (JPL)

Lateral Olfactory Tract (LOT)

Light Emitting Diode (LED)

Membrane (M),

Metal Oxide Semiconductor (MOS)

Monocyte Chemoattractant Protein-1 (MCP-1)

Moving Median Filter (MMF)

Multiple Linear Regression (MLR)

Multiple Sclerosis (MS)

Nitric Oxide (NO)

Non-Small Cell Lung Cancer (NSCLC)

N-terminal domain (NTD)

Nucleocapsid (N)

Odorant Binding Protein (OBP)

Optical Coherence Tomography (OCT)

Orthogonal Signal Correction (OSC)

Part Per Million (ppm)

Parts-Per Trillion (ppt)

Partial Least Square (PLS)

Polymerase Chain Reaction (PCR)

Principal Component Analysis (PCA)

Pro-Inflammatory Cytokines (PICs)

Quartz Crystal Microbalance (QCM)

Real-Time Reverse Transcription Polymerase Chain Reaction (rRT-PCR)

reduced Graphene Oxide (rGO)

Relativity (R^2)

Root Mean Square Errors (RMSEs)

Royal Infirmary of Edinburgh (RIE)

Second C-Terminal Domain (CTD2)

Self-Organizing Maps (SOMs)

Serial Clock Pin (SCL)

Serial Data Pin (SDA)

Severe Acute Respiratory Syndrome Coronavirus 2 (SARS-CoV-2)

Spike (S)

Surface Plasmon Resonance (SPR)

Standards for Reporting Diagnostic Accuracy (STARD)

Surface Acoustic Wave (SAW)

Third C-Terminal Domain (CTD3)

Transparent Reporting of a Multivariable Prediction Model for Individual Prognosis or Diagnosis (TRIPOD)

Tumor Necrosis Factor-Alpha (TNF- α)

Ultraviolet-C (UVC)

University of South Florida (USF)

Volatile Organic Compounds (VOCs)

Volts (V)

Appendix F: Publications

The manuscript format has been used in the preparation of this Dissertation. This Dissertation is a compilation of one published conference paper and two published journal papers.

The first published conference paper entitled “Brain-Computer Interface Based on Magnetic Particle Imaging for Diagnostic and Neurological Rehabilitation in Multiple Sclerosis” comprises a portion of Chapter 3.1.1 of this Dissertation and provides information on energy failure of a neuron as it pertains to inflammatory injury within the brain. It was published as a Conference Paper for 2020 8th IEEE International Winter Conference on Brain-Computer Interface (BCI), published. Apr. 09, 2020. by publisher *IEEE*. [125]

The second published journal paper entitled “Electronic Nose with Detection Method for Alcohol, Acetone, and Carbon Monoxide in Coronavirus Disease 2019 Breath Simulation Model” was submitted to *IEEE Sensors Journal* on Jan. 24, 2021 and was accepted Mar. 25, 2021. © [2021] IEEE. Reprinted, Electronic Nose with Detection Method for Alcohol, Acetone, and Carbon Monoxide in Coronavirus Disease 2019 Breath Simulation Model, *IEEE Sensors Journal* On page(s): 1-9, 2021, Print ISSN: 1530-437X Online ISSN: 1558-1748 Digital Object Identifier: 10.1109/JSEN.2021.3076102] This manuscript comprises at least a portion of Chapters 3, 4, 7, and 8 in this Dissertation and discusses the design, assembly, and implementation of the electronic nose test bed prototype having an array of gas sensors being exposed to a formulated COVID-19 breath simulation mixture. [124].

The third, published manuscript entitled “Neurological Connections and Endogenous Biochemistry – Potentially Useful in Electronic-Nose Diagnostics for Coronavirus Diseases” was submitted to the *Journal of Neuroimmunology and Neuroinflammation* on Feb. 23, 2021 and was accepted June 29, 2021. Miller TC, Morgera SD, Sadow SE, Takshi A, Mullarkey M, Palm M. Neurological connections and endogenous biochemistry - potentially useful in electronic-nose diagnostics for coronavirus diseases. *Neuroimmunol Neuroinflammation* 2021;8:[Accept]. <http://dx.doi.org/10.20517/2347-8659.2021.05>. [154] This manuscript comprises at least a portion of Chapters 1-4 of this Dissertation, which introduces COVID-19 symptoms, neurological manifestations of SARS-CoV-2, electronic nose signal processing correction methods, and reporting diagnostic accuracy recommendations

About the Author

Tiffany C. Miller is a proud member of the Patent Bar since 2008 and is permitted to prepare an application for a patent and conduct the prosecution before the United States Patent and Trademark Office. Her qualifications have been mastered by achieving a Bachelor of Science in Bio-Medical Sciences, a Master of Science in Engineering Science, the passing of the Examination for Registration to Practice in Patent Cases Before the United States Patent and Trademark Office and known informally as the Patent Bar, and is a Ph.D. Candidate in Electrical Engineering at USF. She enjoys flying as a solo pilot and has demonstrated a showing of knowledge in legal, scientific, and technical abilities by developing her pre-medical background and applying it to achieving the technical understanding of many fields, including: Mechanical, Processes, Electrical, Bio-Medical, Bio-Engineering, Formulations, Automotive, Aviation, and Marine.

At the beginning of this Dissertation research there was a need to rapidly diagnose COVID-19 infection. The VOC biomarkers of COVID-19 were determined and corresponding gas sensors were configured for their detection. An eNose prototype was built to collect acquired gas data from a COVID-19 breath simulation solution of acetone, CO, and alcohol. The acquired gas data was filtered and advanced mathematics of OSC, PLS, and PCA was used for calibration and signal correction. The eNose prototype continues its ongoing developmental progress of incorporating mucus-based electrochemical transistors at the Dept. of Electrical Engineering, USF, Tampa, campus led by Dr. Arash Takshi.